UNIVERSITY OF BERGEN
DEPARTMENT OF PHYSICS AND TECHNOLOGY

Anisotropic reflectance of Arctic snow and sea ice

By:*Hanne Henningsen*
Supervisor: *Børge Hamre*

MASTER THESIS IN
OPTICS AND ATOMIC PHYSICS

November 20, 2017

Contents

List of Figures

List of Tables

Abstract

We present an investigation of the angular distribution of reflected light on snow and sea ice, for three selected wavelengths; 500, 800 and 1100 nm. Our analysis covers how the angular reflectance distribution is affected by varying the solar zenith angle and cloud configuration, and also if snow grain size and snow thickness will has an influence. We have mainly addressed snow reflective properties, as snow is a key player in the earth's radiation budget.

With an accurate radiative transfer simulation tool (AccuRT), we have simulated various cloud, snow and sea ice scenarios. Our main conclusion is that neither snow or sea ice seems to reflect light isotropically over the upper hemisphere, and that the presence of even thin clouds contribute to extensively to the diffusing of light. The effect is most prominent for 500 nm light, while for longer wavelengths the diffusing effect happens at a slower rate, leaving detectable signals on small cloud variations.

For a typical cloud configuration, a cloud thickness of more than 100 m will diffuse the incident light to an extent where we can not distinguish the incident solar angle based on angular distribution plots.

In April 2016 we collected spectral radiation data on three different locations on the arctic archipelago of Svalbard. This data has been assessed in light of the modelled results, proving to support our hypothesis of the wavelength dependency of the clouds diffusing effects. We found that a thicker cloud cover will shift the detected average angle of the incident light towards the average polar angle (45°).

Acknowledgements

First and foremost, I wish to express gratitude to my supervisor *Børge Hamre*. He was always supportive, kind, and optimistic throughout this period, and his door was always open for both professional advice and encouragement.

My appreciations goes to *Arne Kristoffersen* for his feedback and comments.

I am grateful to all the members of the optics and atomic physics group for their company and wisdom, and to my fellow master students, for making the long hours in the study hall more worthwhile.

I also wish to express my sincerest gratitude to all of the crew members in the Norwegian Polar Institutes Glaciology Team 2016: Jack Kohler, Elisabeth Isaksson, Jean-Charles Gallet, Stephen Hudson, Thomas Schuler, Lana Cohen, Chris Nuth, Torbjørn Østby, Ankit Pramanik, Cesar Deschamps-Berger, and Andreas Köhler, as well as the international director Kim Holmén. They all exhibited great hospitality and taught me invaluable insight during my stay in Ny-Ålesund. A special thanks to Tõnu Martma, who kindly took me under his wing and made both my work and stay more enjoyable and accomplishable. Thanks to Chris Borstad, associate professor at UNIS, for generously equipping me with one of his snow kits for a day of field work on Tellbreen.

During the two years of working with this thesis, from taking relevant courses and collecting data to finally submitting, my personal life has changed substantially. On October 3rd, 2016, my heart broke: My little brother died this day, way too soon and all too sudden. He will always inspire me to strive for honesty, truth, and love.

Last but not least, I am extremely grateful for the encouraging and inspiring words from my friends and family.

Thank you also, dear *Dino* for your endless love and support,

Chapter 1

Introduction

Snow and sea ice are some of the most reflective large scale surfaces occurring naturally on the planet. They play a big part in the earth's radiation budget, reflecting incoming solar radiation back into space, and hence contribute to less heating of the earth/atmosphere system [e.g. Hansen and Nazarenko, 2004]. A reduction in snow- and ice covered surfaces will therefore contribute to lower reflectivity and consequently higher absorption, which again is amplified through further reduction and melting. Knowledge about these changes is of great interest, and for that, ability to interpret radiation data with minimized errors is important.

The Coupled Atmosphere-Snow-Ice-Ocean (CASIO) system is a comprehensive and complicated structure, consisting numerous parameters that affect radiation transport [e.g. Thomas and Stamnes, 2002, Lamb and Verlinde, 2011]. These parameters include atmospheric micro- and macro structure, snow-, ice- and water composition, cloud configuration, etc. Unlimited variation possibilities within these parameters makes modelling and data interpreting on the matter a difficult task, with many unknowns. We can however make fair approximations and simplifications to investigate overall trends.

1.1 Context

Satellites that regularly perform measurements of the radiation from earth and cloud surfaces generally operate with narrow field-of-view instruments. These are confined by orbital and instrumental restraints, allowing measurements of only certain local times and directions of view [Taylor and Stowe, 1984]. Knowledge about the angular distribution of reflected light is therefore valuable for fields relying on measurements of reflected sunlight, like climatology and earth climate surveys. Generally these applications are based on measurements of radiance coming from a particular direction [Hudson et al., 2006].

Based on the previous work on the matter, we want to investigate how various physical parameters governs the optical properties of snow and ice, and how their changes affects the variability in observed reflectance. We will focus on how the solar zenith angle and the geometrical composition of our media (size distributions and volume fractions of brine and bubbles in sea ice, and snow grain size and density in snow), and especially see how the angular distribution of the reflected light varies under various conditions.

It is also interesting to note that fields using synthetic imaging or computer generated imaging, implement different surfaces' reflectance distributions to create a realistic graphical user interface.

1.2 Previous work

Several studies of the optical properties of snow, ice and sea ice have been conducted over the years. The albedo of sea ice reaches maximum at $\lambda = 460 - 470$ nm, and snow- and sea ice albedo drops drastically towards the near infrared [Warren, 1982, Perovich, 1996]. Snow grain size normally increases as the snow ages, causing a decrease in its albedo, while snow albedo increases with increasing solar zenith angle [e.g. Warren, 1982]. The decrease in albedo for increased snow grain size can be explained by the increased path length a photon will travel through the snow between scattering opportunities.

Warren [1982] also addressed the bidirectional reflectance distribution function of snow, by measuring it at the snow surface, and at the top of the atmosphere. They found that

Warren [1982] emphasize that solar wavelengths in the range of 0.3 to 5 μm are important for determining the climate role of snow, as shorter wavelengths are absorbed by the atmosphere. Longer wavelengths are considered thermal infrared, and will not be discussed in this thesis.

The angular distribution of reflected radiance becomes more isotropic at shorter wavelengths because of atmospheric Rayleigh scattering [Hudson et al., 2006]. Warren et al. [1998] finds that the bidirectional reflectance of fine grained, pure snow is independent of wavelength from 300 to 700 nm, proposing weak ice absorption in this spectral range as an explanation.

In Schaepman-Strub et al. [2006] they have examined how the angular reflectance distribution on a slab of spheroids vary when the diffuse component is increased. The distribution gets more isotropic when the diffuse component is increased. For completely diffuse light, the distribution shows a "shallow bowl" shape (meaning a minimum in a solid angle (here ∼0.85 sr) centered around nadir direction, and a slightly higher value around), a result arising from strong forward scattering on the slab spheroids.

Taylor and Stowe [1984] have studied the reflectance characteristics of land, ocean, snow, and ice. They conclude that all of the surfaces in their study become more specular as the solar zenith angle (SZA) increase, and that albedo generally increases with increasing SZA, except for snow, which shows little (and even a slight decrease within a small range). This last result is rather opposite of Warren [1982] who finds that snow albedo is increased at all wavelengths as solar zenith angle increases.

Taylor and Stowe [1984] finds further that cloud and land surfaces change from limb darkening to brightening as SZA increases. They also note that snow exhibit the most isotropic reflectance distribution of the surfaces.

Perovich [1996] conclude that that optical changes like albedo, transmittance and reflectance are directly related to changes in the state and structure of the ice. He finds that the formation of air bubbles due to brine drainage enhances scattering which results in larger albedos, and that the sea-ice optical properties depend on the distribution and volume of brine and air inclusions. Light et al. [2003] also supports this conclusion, as they found that the link between both structural and optical properties of sea ice is closely related to the distributions of brine and air inclusions.

Regarding melt ponds on sea ice, Maykut [1982] found that in early July, shallow melt ponds can cover as much as 50% of the ice, while this fraction decrease rapidly towards 1/10 by early August.

In Hudson et al. [2006] they have measured the bidirectional reflectance function of Antarctic snow, and found it was nearly constant throughout the part of the spectrum where the snow albedo is high ($350 \leq \lambda \leq 900$ nm).

Dumont et al. [2010] studies the angular distribution of reflected light on snow, and observe a reflectance pattern with darkening at grazing angles for near vertical incidence (0°, 30°), for wavelengths shorter than 1 μm, in both modelled- and observational studies. They emphasize that absorption is small at these wavelengths, and that the photon undergoes a high number of scattering events before it either escapes or is absorbed. They find a stronger forward scattering for longer wavelengths and/or large solar zenith angles because of higher absorption and prevailing single scattering.

1.3 Motivation and aim

The main objective of this thesis is to investigate the angular distribution of reflected light from snow- and sea ice surfaces. This knowledge can be useful for estimating the magnitude of possible errors in remote sensing radiation data from snow- and ice surfaces.

Our approach is to isolate different parameters, and see how the angular distribution responds. We will also look at previous work, and see if our results will support previous conclusions, or unveil possible disagreements. Both incident solar zenith angles and observational polar angles are key elements in this analysis. We will look into the scenarios where we have only a thin layer of snow on top of sea ice, and also how the variations in sea ice composition affects its optical properties. An other aspect we will investigate, is the clouds ability to attenuate and diffuse the incident light, and hos their presence will affect the reflectance distributions.

We will also analyze radiation data collected at three different glaciers in the Svalbard archipelago, where cloud analysis also is a central part.

Computational models are extremely useful tools for trying to understand natural processes, as they allow for experimenting and trialing with a lot more flexibility than what can be obtained with field work. When we compare model output results with collected data, we can assess the validity of the model, and more importantly, increase our understanding of the world around us.

When choosing model inputs, we will strive to apply parameters that are within a realistic range, based on existing analysis of the physical properties of the different media.

1.4 Glossary

In Table 1.1 some central identities are presented. A comprehensive list with extensive definitions can be found in Appendix A.2, together with a list of abbreviations.

Table 1.1: Symbols

Symbol	Meaning	Unit	Comment
A	Albedo	-	Surface reflectivity
c	Speed of light in vacuum	ms^{-1}	Value: $\approx 3 \cdot 10^8$
E	Energy	J	-
F	Irradiance	Wm^{-2}	Radiative flux
g	Asymmetry parameter	-	Range: $[-1, 1]$
h	Plancks constant	Js	Value: $6.6261 \cdot 10^{-43}$
k_b	Boltzmann constant	JK^{-1}	Value: $1.3806 \cdot 10^{-23}$
L	Radiance	$\mathrm{Wm}^{-2}\mathrm{sr}^{-1}$	Radiative flux per unit angle
n	Refractive index	-	-
R	Anisotropic reflectance function/factor	-	Abbreviation: ARF
r	Reflectance	-	-
t	Temperature	K	°C is also used
α	Absorption coefficient	m^{-1}	
κ	Extinction coefficient	m^{-1}	Aka attenuation coefficient
λ	Wavelength	m	often $upmu$m = 10^{-6} m, nm = 10^{-9} m
ν	Frequency	s^{-1}	-
ρ	Bidirectional reflectance distribution function	sr^{-1}	Abbreviation: BRDF
σ_a	Attenuation cross section	-	-
τ	Optical depth	-	-

Chapter 2

Theory

2.1 Light

Light has fascinated and intrigued humans for millennia. Plato's emission theory describes how he visioned light as being rays originating from our eyes, illuminating what we were looking at. Today we know that the process is exactly opposite. Our eyes receive rays originating from a luminous source.
It surrounds us at all times, and still keeps fascinating curious minds, as light exhibits remarkable features. One of which is its particle-wave duality, which lead to many disputes in the early 1900's, the beginning of modern physics, before scientists came to terms with the somewhat odd principle of something being both a particle and a wave at the same time. In this thesis we will address both the wave- and particle properties of light, as both are needed to describe light behaviour. We can relate the wavelength, λ and frequency, ν of light by the following equation:

$$\lambda = \frac{c}{\nu}, \tag{2.1}$$

where c is the speed of light in vacuum. In a particle perspective, the frequency of light is associated with a certain photon energy E:

$$E = h\nu, \tag{2.2}$$

where h is the Planck constant (the smallest unit for energy quanta), equal to $6.6261 \cdot 10^{-43}$Js.

2.1.1 Radiometry

One key property of electromagnetic radiation is that it carries energy. In this thesis we will address this energy flux of the radiation in two terms: *Irradiance*, denoted as F, often with subscript $\uparrow$ for upwards and $\downarrow$ for downwards, and *radiance*, L, also often with subscripts $\uparrow$ and $\downarrow$.

- **Irradiance** is defined as radiative flux per unit surface: $\mathrm{Js^{-1}m^{-2}}$, or $\mathrm{Wm^{-2}}$. Irradiance at a distance r from a point source, is proportional to $\frac{1}{r^2}$, in accordance with the inverse square law, which states that the intensity of a signal in a certain distance from a source, is proportional to one over the the square of that distance.

- **Radiance** is also a measure of radiative flux, but is limited to a unit solid angle: $\mathrm{Wm^{-2}sr^{-1}}$. Radiance is therefore the radiant flux in a specific observing or viewing angle, and is useful for establishing variations in intensity distribution from a source or a surface. As radiance is dependent on solid angle, its value is constant and does not fall of with the square of the distance of the source, as for irradiance. (This can be explained by the solid angles' proportionality to the distance, which follows the inverse square law)

Throughout this thesis we will also look at the spectral irradiance and radiance, meaning the intensity per unit length (often $\mathrm{nm^{-1}}$). We will however in many cases not emphasize these incidents, and rather leave it to this clarification.

It is also useful to note the cosine dependence of irradiance, where the received energy flux at a surface is directly proportional to the cosine of the angle of the incident light, relative to the surface normal. The concept is depicted in Figure 2.1.

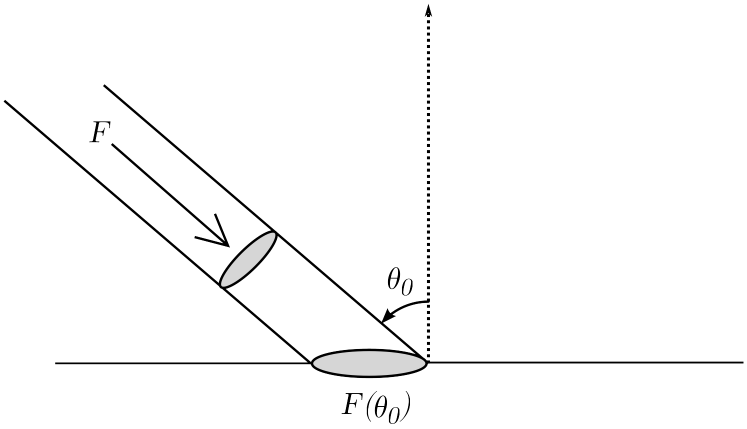

Figure 2.1: Cosine irradiance. $F(\theta_0) = F\cos\theta_0$

2.1.2 Solar Radiation

All particles of matter with temperatures above 0 K contains exited quantum states, and with their spontaneous decay radiative energy is released [Thomas and Stamnes, 2002]. Black bodies are physical idealizations of objects in perfect electromagnetic equilibrium; they radiate at the same rate as they absorb radiation, with zero reflectance. Their emittance can be described by Planck's radiation law:

$$P_e(\lambda) = \frac{2\pi hc^2}{\lambda^5}\frac{1}{\exp(\frac{hc}{\lambda k_b T}) - 1}. \tag{2.3}$$

Here λ, h and c is the same as in Equations 2.1 and 2.2, T the surface temperature of the black body, and k_b the Boltzmann constant (relates a gas' temperature to its kinetic energy), equal to $1.3806 \cdot 10^{-23}$ JK^{-1}.

By letting T = 5780 K in Equation 2.3, a good approximation of the solar radiation spectrum emerges. According to the inverse square law (Section 2.1.1), multiplying Equation 2.3 with the square of the ratio between the solar radius and the sun-earth distance, gives the fraction of idealized black-body irradiance reaching the top of the atmosphere (TOA), weighed with the cosine of the solar zenith angle, θ_0 (see Section 2.1.2):

$$F_{TOA} = P_e(\lambda)\left(\frac{R_\odot}{1\mathrm{AU}}\right)^2 \cos\theta_0, \tag{2.4}$$

where $R_\odot$ is the solar radius, and AU the mean distance between the sun and the earth. Listed values for these are: $R_\odot = 6.9598 \cdot 10^8$ m, and $1\text{AU} = 1.4959789 \cdot 10^{11}$ m [Kutner, 2003]. The input solar zenith angle is set to 45°. In Figure 2.2 this spectrum is shown, together with the modelled spectrum for irradiance at TOA and at ground level.

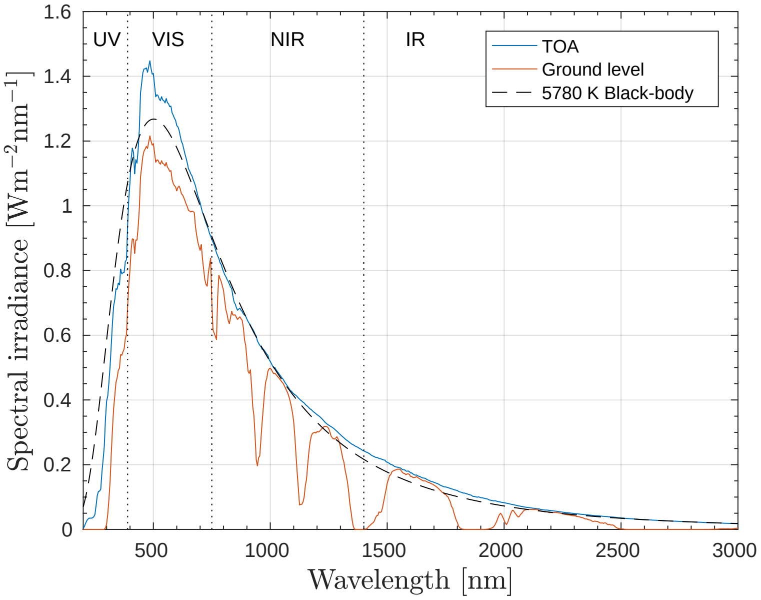

Figure 2.2: The solar spectrum: The dashed black line indicates the black-body radiation at T=5780 K, the blue line the solar radiation at the top of the atmosphere (TOA), while the red line shows the incoming radiation at ground level, on a cloud free day. Ultraviolet, visible, near infrared and infrared parts of the spectrum are indicated.

For visible light ($400 \leq \lambda \leq 750$ nm) there is some atmospheric attenuation throughout the interval, as well as a few more distinct indentations around 600-700 nm. Significant blocking occurs in the ultraviolet (UV) part of the spectrum ($\lambda < 400$ nm), as well as for some wavelengths in the near infrared (NIR, $750 \leq \lambda \leq 1400$ nm) and infrared (IR, 1400 nm $\leq \lambda \leq 1$ mm). The wavelengths in these ranges correspond to the vibrational energies of some strongly absorbing atmospheric gases: For shorter wavelengths ozone (O_3) dominates the absorption, while the indentations in the NIR and IR can be ascribed to the presence of water vapour (H_2O) [e.g. Lamb and Verlinde, 2011, Bohren and Clothiaux, 2006]. The presence of aerosols are also responsible for some atmospheric attenuation (see Section 2.3).

Solar zenith angle

The earth rotates with an axial tilt of 23.45° relative to its orbital plane, giving a yearly radiative flux variation, as the tilt affects the angle of incidence (i.e., the solar zenith/elevation angle), as the earth moves around the sun. This deviation gets more pronounced for higher latitudes, giving large seasonal variations in polar regions. By spherical geometry the relationship can be expressed like:

$$\cos\theta_0 = \sin\alpha_s = \sin\Phi\sin\delta + \cos\Phi\cos\delta\cos h, \tag{2.5}$$

where θ_0 is the solar zenith angle, α_s the solar elevation angle, Φ latitude, and h the hour angle of the sun. The maximum zenith angle occurs at solar noon, when $h = 0$. δ is the declination of the sun, and is defined as the angle between the equatorial plane and the incident solar rays. It can be approximated by

$$\delta = -23.45^\circ \cdot \cos\left(\frac{360^\circ}{365} \cdot (d + 10)\right), \tag{2.6}$$

where d is the day in the year, with day 1 being January 1st. At summer solstice, June 21st ($d = 173$), the sun will be at its maximum elevation on the northern hemisphere. At 78.8° N 11.9° E, the sun reaches its closest to zenith – 55.4°, at solar noon (12:14:22, UTC -1) on this day.

To aid us establish our relevant angles, we have however used a solar positioning calculation tool from the National Oceanic and Atmospheric Administration [2016].

As our data was collected at these latitudes during spring time (see Section 3.1.3), the solar zenith angle in our measurements reached a minimum at around 70°, equivalent to a maximum solar elevation angle of about 20°. For the imaginary line that defines the Arctic circle, located at roughly 66.7° N across the globe, the minimum solar zenith angle is approximately 43.3° [National Oceanic and Atmospheric Administration, 2016].

2.2 Light and matter

When light interacts with matter, there is three possible outcomes: transmission, absorption, or scattering. The sum of absorbed and scattered irradiance can be noted as extinction, or attenuation, and is in essence the radiant flux that is not transmitted.

2.2.1 Attenuation and transmission

When trying to understand an optical medium we can start by addressing its optical depth, which is a measure of how the radiant flux is attenuated. It can be defined as

$$\tau = N\sigma_a l, \tag{2.7}$$

where N is the number of particles per unit length, σ_a the attenuation cross section of a particle in the medium (this unit can be interpreted as the effective area of the particle where radiation can be absorbed or scattered, and depending on the shape and volume of the particle, it might vary greatly from its geometrical cross section), and l the physical length of our medium. The optical depth is a measure of how opaque an optical medium is, and may be very dependent on wavelength. An optically thin medium will have a small optical depth ($\tau \ll 1$), with low absorption and scattering, while an optically thick medium would exhibit more absorption and scattering, attenuating more radiation.

Optical depth per unit length is defined as

$$\kappa = N\sigma_a, \tag{2.8}$$

an identity better known as the extinction (or attenuation) coefficient. It can be thought of as the reciprocal of mean free paths [Thomas and Stamnes, 2002], and is the key element in Beer-Lambert's law of attenuation, an expression for the remaining, or unattenuated irradiantion at a depth x in a medium:

$$F = F_0 \exp(-\kappa x), \tag{2.9}$$

where F_0 is the incident irradiation at depth $x = 0$. We see that a highly absorptive or back-scattering medium will have large extinction coefficient, as little radiation is transmitted.

Refractive index

The refractive index, n of a material where a light wave can propagate, can be defined as

$$n = \frac{c}{v}, \tag{2.10}$$

where c is the speed of light in vacuum, and v the speed of light in an optically homogenous medium. If light travels from one media to an other, an we know the refractive index of one of the two, we can use Snel's[1] law to establish the other:

$$n_2 \sin\theta_2 = n_1 \sin\theta_1, \tag{2.11}$$

where n_1 and n_2 are the refractive indices, θ_1 and θ_2 the angles of the incident and refracted ray, depicted in Figure 2.3. The higher the refractive index, the slower light will propagate through the medium, and the larger the refraction. The refractive index of vacuum is 1, while it will be higher for optical media. The refractive index of optical media are wavelength dependent, an attribute responsible for the dispersion of light through prisms, raindrops, etc., splitting the beam into its separate wavelengths.

These two definitions may however be insufficient for describing light behaviour in optical media, as the refractive index of a material is in fact a complex identity, consisting of a real and an imaginary part: $n = n_r + in_i$, where n_r is in reality the refractive index defined in Equation 2.10. When looking at the wavelength-dependency of the refractive index of a medium, we separate the two, as the real part is connected to the speed of light in the medium, while the imaginary part is connected to how light is absorbed in the medium, through the absorption coefficient α [Warren and Brandt, 2008]:

$$\alpha = \frac{4\pi n_i}{\lambda}. \tag{2.12}$$

It has units [m^{-1}], and is directly related to the wavelength of the light. In Figure 2.4 we see the imaginary part of the refractive index of ice, together with its absorption coefficient. The absorption coefficient reaches its minimum

---

[1] This spelling is, as pointed out by Bohren and Clothiaux [2006], surprisingly the correct one!

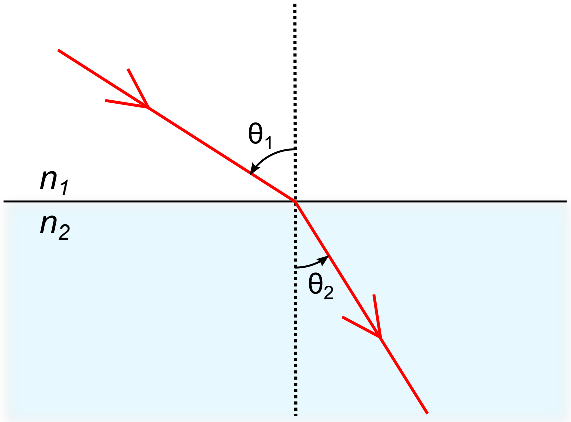

Figure 2.3: Snel's law of refraction. Here light is entering a medium of higher refractive index ($n_2 > n_1$), meaning $\theta_1 > \theta_2$, by Equation 2.11.

value between 200 and 400 nm, corresponding to UV and barely into visible wavelengths where we have high atmospheric attenuation (Figure 2.2), before it increases exponentially towards 1000 nm. Ice is therefore less absorbent in the violet/blue than in longer wavelengths in the spectrum, a feature we can experience when admiring large bodies of pure ice, and is also what we see in large bodies of water – they absorb more of the longer wavelengths in the visible spectrum, while light of shorter wavelengths penetrate longer into the media, leading to a blue appearance.

The refractive index of ice and water is very wavelength dependent throughout the EM spectrum, as seen in Figure 2.5. Here the real and imaginary part of the refractive index of ice is shown, and we see that both are very wavelength dependent. The refractive indices in our model (Section 2.4) are based on these values, obtained by Warren and Brandt [2008].

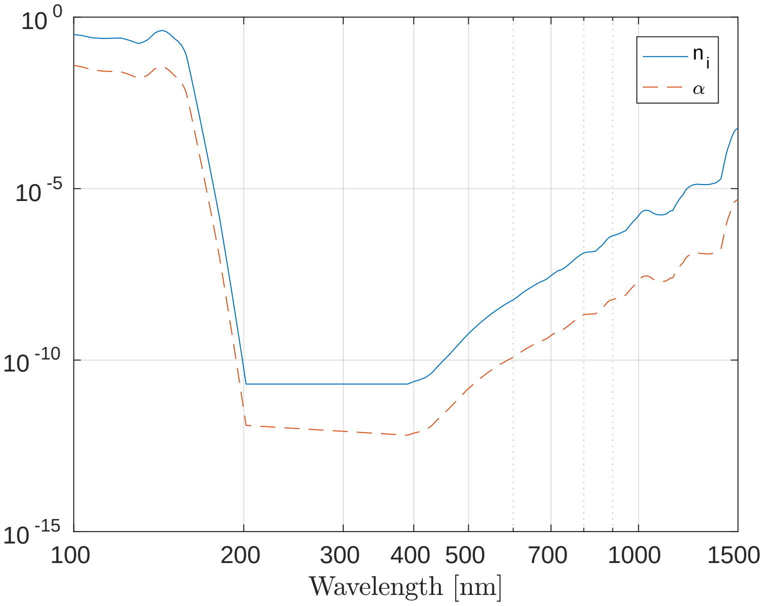

Figure 2.4: Imaginary part of refractive index n_i [unitless], and the absorption coefficient α of pure ice, at UV-, visible-, and NIR wavelenghts. Listed values from Warren and Brandt [2008].

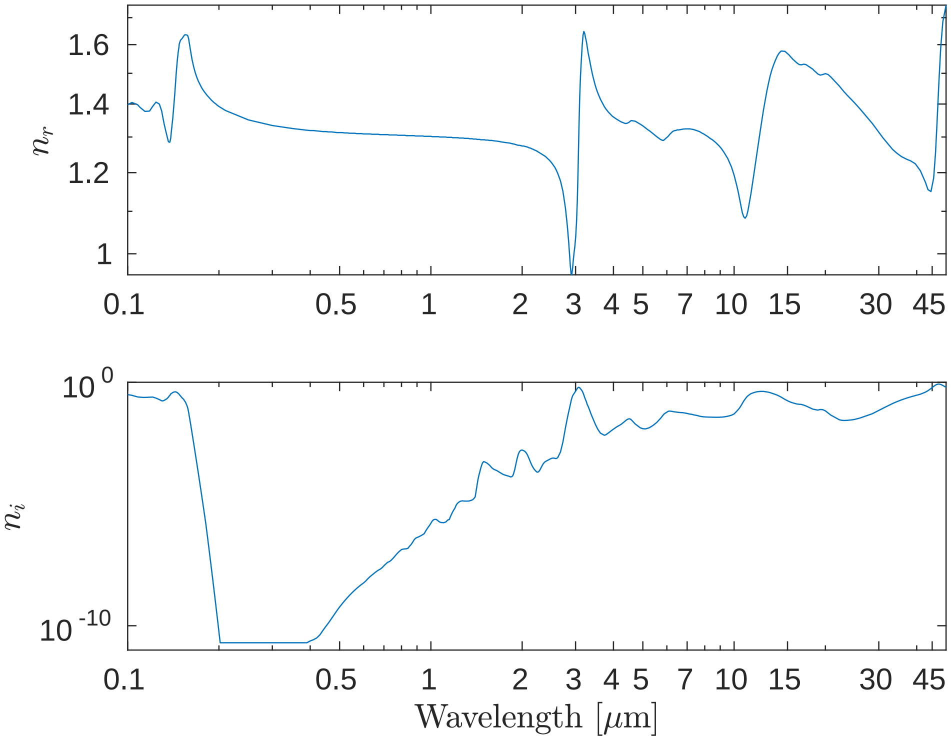

Figure 2.5: Index of refraction of ice, real part (top) and imaginary part (bottom). Listed values from Warren and Brandt [2008].

2.2.2 Scattering: reflection and refraction

Anisotropy

Anisotropy is defined as directional dependence/sensitivity: Observed values are different when measuring along different directional axes in a medium [Encyclopædia Britannica, 2006].

The asymmetry parameter g represents the degree of asymmetry in the angular scattering on a particle. For isotropic scattering $g = 0$, for complete backscattering it is -1, and for complete forward scattering it is 1 [Thomas and Stamnes, 2002].

Scattering on particles

When light interacts with matter we can observe scattering events. Both particle size and the wavelength of the light dictates the nature of the scattering. Depending on particle size, two different functions may describe a scattering event:

- **Rayleigh scattering** from small particles, typically $\frac{1}{10} <$ of the wavelength of the light, spreading the light in a somewhat uniform way ($g \approx 0$). One famous attribute of Rayleigh scattering is its proportionality to λ^{-4}, and hence is much more prevalent for shorter wavelengths.
- **Mie scattering** from larger particles, with sizes from around the same order of magnitude as the incident light, and larger. It has a positive asymmetry parameter, with a peak in the forward direction.

The atmosphere comprises of molecules and particles of varying size and composition, which exhibit different inherent optical properties. In general, atmospheric gas constituents and molecular aerosols contribute to Rayleigh scattering, while larger particles like droplets, crystals, dust and larger aerosols contribute to Mie scattering. A general result is that the larger the particle, the more scattering in forward direction [Bohren and Clothiaux, 2006]. The blueness we observe in the sky is a result of Rayleigh scattering (our eyes are not to be trusted though: the sky is only blue to us due to their response curve being more sensitive in the green part of the spectrum, the skylight spectrum actually peaks in the violet [Bohren and Clothiaux, 2006]).

Scattering in terms of geometric optics

In geometric optics we generally have two types of surface reflection, specular and diffuse, shown in Figure 2.6. Specular reflection follows the law of reflection, stating that the angle of incidence is equal to the angle of reflectance, relative to surface normal. For diffuse scattering, light is reflected equally bright in all directions. These are however to be consider extremes, as most surfaces will exhibit reflectance properties as a combination of the two.

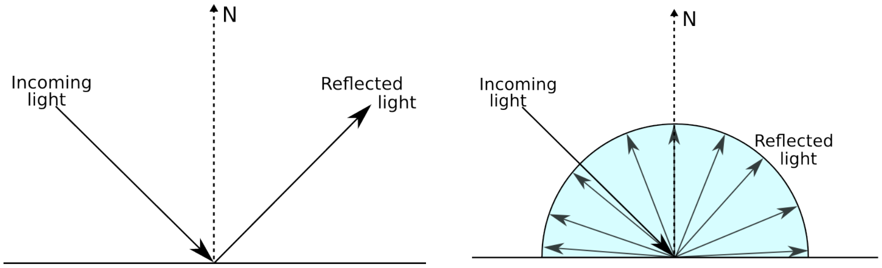

Figure 2.6: Schematic view of two types of ray reflection, specular (left panel), and diffuse (right panel).

2.2.3 Albedo

The albedo A of a surface is defined as the ratio between the reflected and the total incident irradiance:

$$A = \frac{F_\uparrow}{F_\downarrow}, \tag{2.13}$$

where $F_\uparrow$ is the total upwelling irradiance, and $F_\downarrow$ the downwelling. It is a central parameter when assessing the reflectivity of surfaces of the earth. It is a wavelength dependent property, and might vary greatly for different surfaces throughout the electromagnetic spectrum.

Typical values

In the Arctic (and Antarctic) ocean regions, we can roughly separate between three surfaces: snow, ice and open water. These exhibit different reflective properties, as we can see in Figure 2.7, which shows some reference albedos for the respective surfaces, obtained with our radiative transfer model. The solar zenith angle is set to 40°. We keep in mind that the albedo depend on inherent optical properties within the media, while noting that pure snow exhibits a high albedo in the visible part of the spectrum, while dropping of quite rapidly in the NIR, reaching values below 0.1 for wavelengths > 1450 nm. In a sense we can actually say snow is almost "black" in this interval. Sea ice albedo reaches its maximum at 0.8 for $\lambda = 400$ nm, and drops towards zero almost linearly from $\lambda = 600$ to 1000 nm. Pure ice and water exhibit a low albedo for all wavelengths, with a small peak at 0.1 for $\lambda = 400$ nm. The huge difference between sea ice- and pure ice albedo tells us that the physical properties of sea ice, like brine and air inclusions, are of great importance for the reflective properties of sea ice.

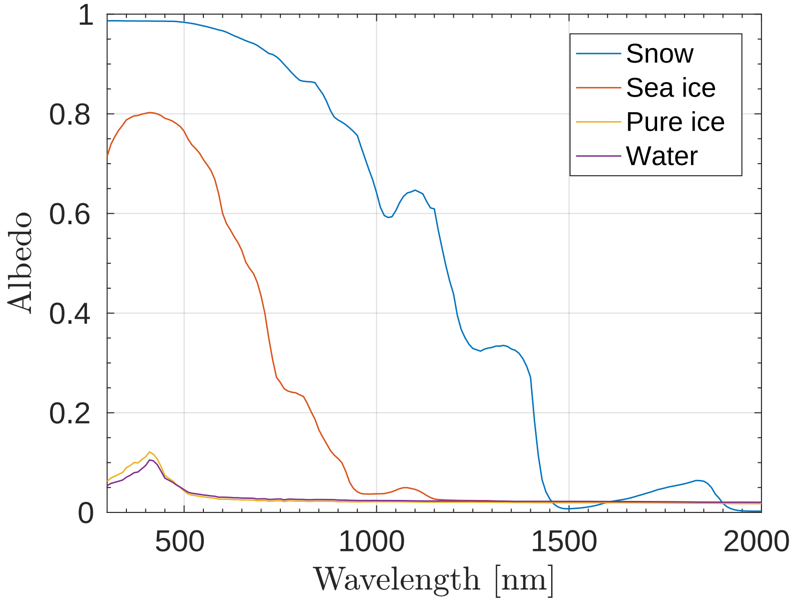

Figure 2.7: Typical albedo for snow (blue), sea ice (red), pure ice (yellow), and water (purple). The solar zenith angle is set to 40°, with no clouds. Generated with our model, input parameters of the snow and sea ice can be found in Table 2.1.

Table 2.1: Ice and snow parameters used to generate Figure 2.7. See Section 2.4 for model details.

Media		Depth [cm] (from top)	Density [kg/m^3]		Snow grain radii [μm]	
Snow	Layer 1	0-30	145		200	
	Layer 2	31-100	240		1500	
			Brine radii [μm]	Brine volume fraction	Bubble radii [μm]	Bubble volume fraction
Ice	Layer 1	0-20	100	0.05	100	0.01
	Layer 2	21-100	150	0.01	200	0.005

2.2.4 Reflectance functions

What is the difference between reflectance and albedo? They are both defined as ratios of reflected and incoming light at a surface, but they have different properties: Albedo (Equation 2.13) is a measure of the ratio of the total reflected and incoming irradiance, and can be considered a measure of the ratio of the total energy reflected at a surface.

When we use the term "reflectance" in this thesis, we are referring to reflection that is dependent on incident and reflected angle, and is to be thought of as a material property. Albedo can in this sense be regarded as the spectral reflectance over the whole hemisphere [Warren, 1982].

In the field of remote sensing, angular distribution of reflectance and the concept of the bidirectional reflectance distribution function (BRDF), ρ is essential [e.g Hudson et al., 2006, Schaepman-Strub et al., 2006, Dumont et al., 2010]. It describes how the intensity of the reflected light depends on both the angle of the incident light, and the viewing angle of the instrument. Adapted from Schaepman-Strub et al. [2006][2], we can define it as the ratio between reflected radiance $L(\theta_0, \theta, \phi)$ in observing angle (θ,ϕ), and the irradiance beam F, from zenith angle θ_0:

---

[2] The authors include the azimuth angle of incidence, ϕ_0 in their definition, but as we always define our source to be at $\phi_0 = 0$, we leave it out for simplicity.

$$\rho(\theta_0, \theta, \phi) = \frac{dL_{\uparrow}(\theta_0, \theta, \phi)}{dF_{\downarrow}(\theta_0)}. \tag{2.14}$$

As it is a measure of light reflected in a particular direction, the BRDF has units sr^{-1}. A schematic view of the involved angular parameters is shown in Figure 2.8.

While being a useful function for describing surface reflectance properties, it does however exhibit some weaknesses for evaluating satellite data. As it only takes into account the direct beam of incident irradiance, and not the diffuse component arising from scattering on atmospheric constituents (gases, aerosols, cloud particles), it is not possible to describe real life outdoor situations.

The total downward irradiance is in other words left out of Equation 2.14, while it is of high importance when assessing outdoor surface reflectivities [Schaepman-Strub et al., 2006]. This is especially true for shorter wavelengths were Rayleigh scattering is dominant. For longer wavelengths however, the BRDF becomes more accurate for describing the angular reflection of a surface, as the atmospheric scattering decreases [Hudson et al., 2006, Dumont et al., 2010]. For examining the angular distribution of reflected light (including the whole visible part of the spectrum), we can use a function defined by Suttles et al. [1988] that takes the diffuse component into account: π times the upwelling radiance $L_{\uparrow}$, divided by the upwelling irradiance $F_{\uparrow}$, or:

$$R = \frac{\pi L_{\uparrow}}{F_{\uparrow}}, \tag{2.15}$$

which is called the anisotropic reflectance factor (ARF). In angular notation the ARF of a surface is:

$$R(\theta_0, \theta, \phi) = \frac{\pi L_{\uparrow}(\theta_0, \theta, \phi)}{F_{\uparrow}(\theta_0)}, \tag{2.16}$$

where $L_{\uparrow}(\theta_0, \theta, \phi)$ is the upwelling radiance, and $F_{\uparrow}(\theta_0)$ the upwelling irradiance. The upwelling irradiance can be defined as the integral of upwelling radiance, over all viewing azimuth ϕ and polar θ angles:

$$F_{\uparrow}(\theta_0) = \int_{\phi=0}^{2\pi} d\phi \int_{\theta=0}^{\frac{\pi}{2}} d\theta L_{\uparrow}(\theta_0, \theta, \phi) \cos\theta \sin\theta. \tag{2.17}$$

The ARF then becomes:

$$R(\theta_0, \theta, \phi) = \frac{\pi L_\uparrow(\theta_0, \theta, \phi)}{\int_{\phi=0}^{2\pi} d\phi \int_{\theta=0}^{\frac{\pi}{2}} d\theta L_\uparrow(\theta_0, \theta, \phi) \cos\theta \sin\theta}. \tag{2.18}$$

The multiplication with π makes the function dimensionless, and its average value over the hemisphere, weighed with its contribution to upward flux, is unity, as showed by Hudson et al. [2006]:

$$\frac{1}{\pi} \int_0^{2\pi} \int_0^{\frac{\pi}{2}} R(\theta_0, \theta, \phi) \cos\theta \sin\theta d\theta d\phi = 1. \tag{2.19}$$

For a surface exhibiting anisotropic reflectance, R will take values both higher and lower than, and equal to one, depending on viewing angle. A surface with perfectly diffuse reflection properties will result in R being equal to one for all viewing angles. This is know as Lambertian reflection, and is discussed further in Section 2.2.4.

To see how the BRDF and ARF are connected, we can first express the solar beam from an infinitesimal solid angle of incidence, $dF_\downarrow(\theta_0)$ in terms of radiance:

$$dF_\downarrow(\theta_0) = dL_\downarrow(\theta_0) \cos\theta_0 d\omega, \tag{2.20}$$

where $d\omega$ represents the infinitesimal solid angle, and then substitute this into Equation 2.14 to get an expression for $dL_\uparrow$: :

$$dL_\uparrow = \rho dF_\downarrow = \rho dL_\downarrow \cos\theta d\omega, \tag{2.21}$$

and by integrating over the upper hemisphere, the upwards radiance becomes

$$L_\uparrow = \int dL_\uparrow = \int_{2\pi} \rho L_\downarrow \cos\theta d\omega. \tag{2.22}$$

Substituting this result into Equation 2.15, and using Equation 2.13 to express $F_\uparrow$ as $AF_\downarrow$, we get:

$$R = \frac{\pi L_\uparrow}{F_\uparrow} = \frac{\pi \int_{2\pi} L_\downarrow \cos\theta d\omega}{AF_\downarrow} \tag{2.23}$$

$$R = \frac{\pi \int_0^{2\pi} \int_0^{\frac{\pi}{2}} \rho L_{\downarrow} \cos\theta \sin\theta d\theta d\phi}{A F_{\downarrow}} \tag{2.24}$$

$$R = \frac{\pi}{A} \frac{\int_0^{2\pi} \int_0^{\frac{\pi}{2}} \rho L_{\downarrow} \cos\theta \sin\theta d\theta d\phi}{\int_0^{2\pi} \int_0^{\frac{\pi}{2}} L_{\downarrow} \cos\theta \sin\theta d\theta d\phi} \tag{2.25}$$

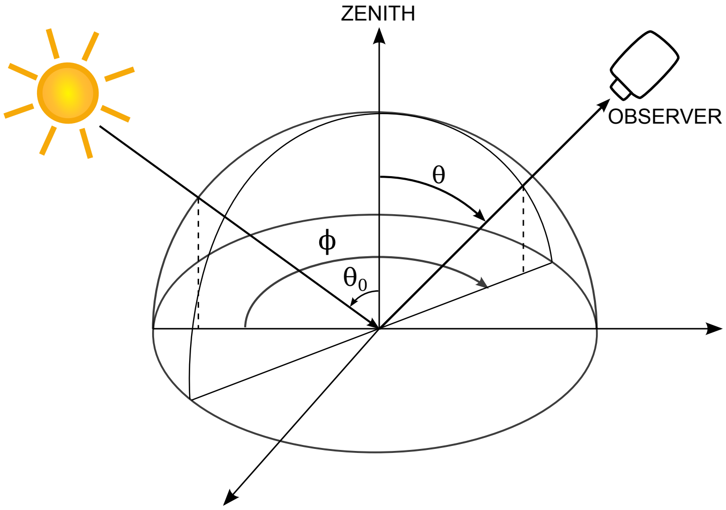

Figure 2.8: Overview of the angular parameters involved in our reflectance functions. θ_0 is the angle of the incident beam, ϕ and θ the viewing azimuth- and zenith angles.

Lambertian reflection

When the light is reflected isotropically in all directions, independent of the direction of the incident light, we have Lambertian reflection [e.g. Schaepman-Strub et al., 2006]. The scenario is the idealized situation of perfectly diffuse reflection, as seen in the right panel in Figure 2.6, where the surface reflects light equally bright in all viewing angles. The ARF (Equation 2.18) of this kind of (ideal) surface equals 1 for all viewing angles.

As most surfaces do not reflect light in an evenly distributed way, we must be careful when interpreting remote-sensing images [Jin and Simpson, 1999]. Warren [1982] states that the radiation reflected by a snow surface is not distributed uniformly into all angles, and that knowledge about this distribution is important.

When remote sensing data are processed for surfaces considered to be Lambertian, knowledge about the ARF can be used to estimate the arising error from that assumption [Dumont et al., 2010]. This is a main objective for examining how the angular distribution varies for different parameters.

As we saw in Equation 2.19, the average value over the upper hemisphere is 1, and evaluating the ARF for different surfaces is therefore a useful way to represent how the reflected radiation deviates from that of a Lambertian surface.

2.3 Characteristics of our media

Both snow, sea ice and clouds contains water constituents in some form. As we have seen in Figure 2.7, pure ice and water has a remarkably lower albedo than sea ice and snow, and therefore there must be other parameters at play, responsible for the large optical variations.

2.3.1 Snow: Grain size and solar zenith angle

One of our main objectives is to examine the reflectance of snow. We will look at its wavelength dependency, and also how the ARF of snow changes for various conditions.

The size distribution of the snow grain size varies with depth, although only the upper 10-20 cm seems to determine the albedo[Wiscombe and Warren, 1980]. Snow grain radii have been found to range from 20-100 μm for new snow, 100-300 μm for fine grained older snow, and up to 1.0-1.5 mm for old snow near the melting point [e.g. Warren et al., 1998, Wiscombe and Warren, 1980]. For arctic snow on sea ice, Warren et al. [1999] found that the mean snow density varies with month of the year from between about 100 to 330 kgm^{-3} in September (when snow accumulation begins), to between 250 and 340 kgm^{-3} in April (April and May are typically the months where maximum snow level is reached [Warren et al., 1999]), and the narrow interval of 190 to 250 kgm^{-3} in August (end of melting season).[3]

As thoroughly investigated by e.g., Wiscombe and Warren [1980], snow grain size plays an important role for the optical properties of snow: As the grain size increases, the albedo decreases for all wavelengths in the visible and near infrared parts of the spectrum, shown in the top panel in Figure 2.9. This correlates well with the observed decreasing albedo as the snow ages, and fresh snow hence tends to be more "white" than older snow, within the otherwise same conditions. The albedo of the snow consisting of the smallest grains, 50 μm, has an almost constant high value of close to 0.9 throughout the entire visible part of the spectrum, and as we increase the radii the albedo drops.
In the bottom panel of Figure 2.9 we see that the snow albedo increases for increasing albedo, in accordance with results from Wiscombe and Warren [1980] (and in disagreement with Taylor and Stowe [1984], Section 1.2). However the variations in albedo are not as pronounced as for the various grain sizes.

---

[3] All values are taken as one standard deviation from the mean value for each month.

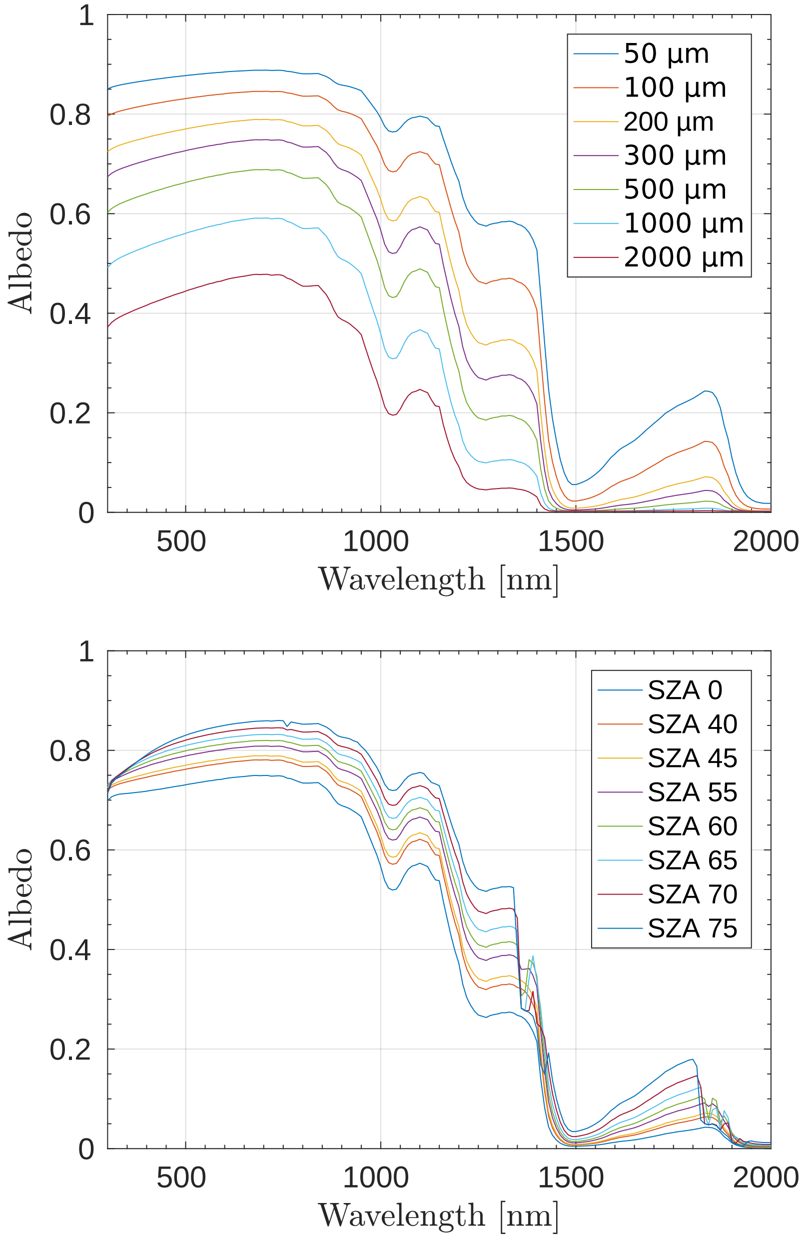

Figure 2.9: The variation of spectral albedo of snow for various snow grain radii, spanning from 50 to 2000 µm (top), and for various solar zenith angles, from 0 to 75° (bottom). Figures created with AccuRT.

An important factor in snow albedo is the age of the snow. After falling to the ground, snow metamorphism starts to take place. Both temperature, topography and wind, as well as inherent entropy properties in the snow crystals determine the speed and behaviour of the process. The result of this metamorphism is both a rounding of the crystals, as well as increasing particle size.

2.3.2 Sea ice: Brine and bubbles

Perovich [1996] finds that sea ice albedo increases with thickness for all wavelengths, before, depending on wavelength, it asymptotically approaches a threshold. For longer wavelengths (600-1000 nm) this limit is about 25 cm, while for shorter wavelengths (around 400 nm) it is around 80 cm [Perovich, 1996]. At that point the ice is optically thick, and a further increase of ice thickness will not affect its albedo.

Experimental results from Light et al. [2003] show that brine inclusion dimensions range from less than 0.01 mm to nearly 10 mm, while air bubbles are generally smaller than 0.2 mm.

As our model does not take temperature inputs, we must rely on the literature on how sea ice structure vary with temperature, to achieve input parameters that reflect real sea ice conditions for different temperatures. We know that warmer ice will have larger, less saline brine inclusions than colder ice, and conversely as the ice cools and grows the trapped brine becomes more concentrated to maintain freezing equilibrium [Light et al., 2003].

We start with looking at the albedo of an ice floe consisting of air bubbles and no brine pockets, and vice verca: an ice floe with brine pockets and no air bubbles, shown in Figure 2.10. The model inputs are shown in Table 2.2. We see that the air inclusions contribute to a threefold of the ice albedo compared to that of ice with only brine inclusions. These The albedo of the bubbly ice resembles that of the reference albedo for ice in Figure 2.7 closely. This leads us to suspect that air inclusions are of great importance for sea ice reflectance, while brine might only contribute some. Brine drainage is however a key contributor to the formation of the air inclusions [Perovich, 1996], and as the sea ice ages its albedo will increase as a result. This reflects the significance of a multi-year sea ice in the earth's radiation budget, as a larger extent of old ice will contribute to a higher albedo.

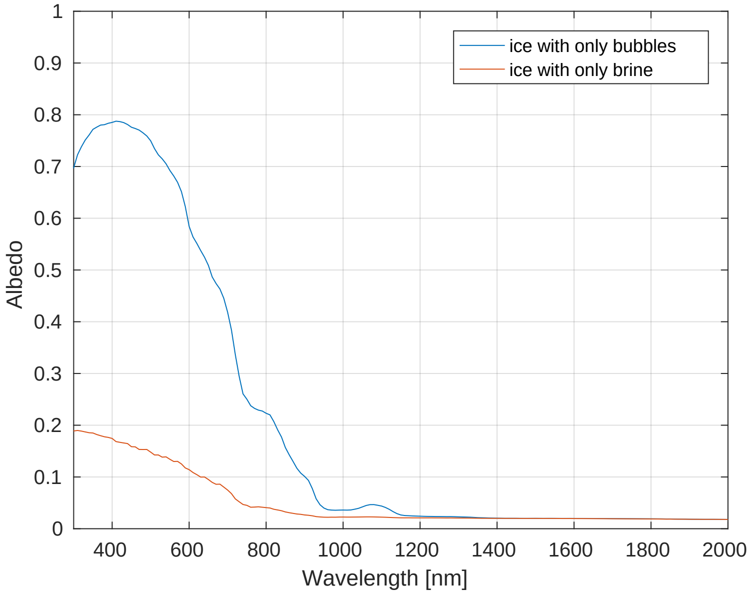

Figure 2.10: The spectral albedo of two-layered sea ice with air bubbles and no brine (blue line), and with brine inclusions and no air bubbles (red).

Table 2.2: Model inputs for producing Figure 2.10. SZA = 40°.

	Ice thickness [cm]	Brine only		Bubbles only	
		Volume fraction	Brine radius [μm]	Volume fraction	Bubble radius [μm]
Top layer	0-20	0.05	100	0.01	100
Bottom Layer	21-80	0.01	150	0.005	200

We want to examine how the variation of bubble and brine volume fractions and radii influence the spectral albedo. We will leave out the bubbles in the brine runs, and vice verca. In the top panel of Figure 2.11) we see how the spectral albedo of sea ice varies greatly with the brine volume fraction. Increasing the volume fraction decreases the albedo. In this model run we kept the brine inclusion radii constant at 100 μm. From the bottom panel of Figure 2.11) we see that decreasing the brine radii increases the albedo. Here the volume fraction of the brine inclusions are kept constant at 0.05. The ice is 1 m thick in both cases. In Figure 2.12 we see the variations of sea ice albedo, when we change the physical characteristics of the bubble radii and the bubble volume fraction. Due to model constraints regarding refraction to a medium of higher refractive index, the curves are a bit off, but the overall trend can still be assessed. The modelling hick ups are explained in Section 2.4 below, and is a consequence of Snel's law of refraction (Equation 2.11). From this Figure we see that sea ice albedo is increasing with increasing bubble volume fraction, and decreasing with increasing bubble radii.

When studying first-year sea ice, Hamre et al. [2004] found the brine volume fraction at the bottom of the ice to be above 40%, while in the ice interior this value spans from 1-15%.

When looking at sea ice through optics glasses, we learn that its complicated physical structure (and variations herein) leads to large variability in its optical properties. Sea ices' intricate structure consists of air-, brine-, solid salts- and contaminants inclusions, which all varies with temperature [Perovich, 1996].

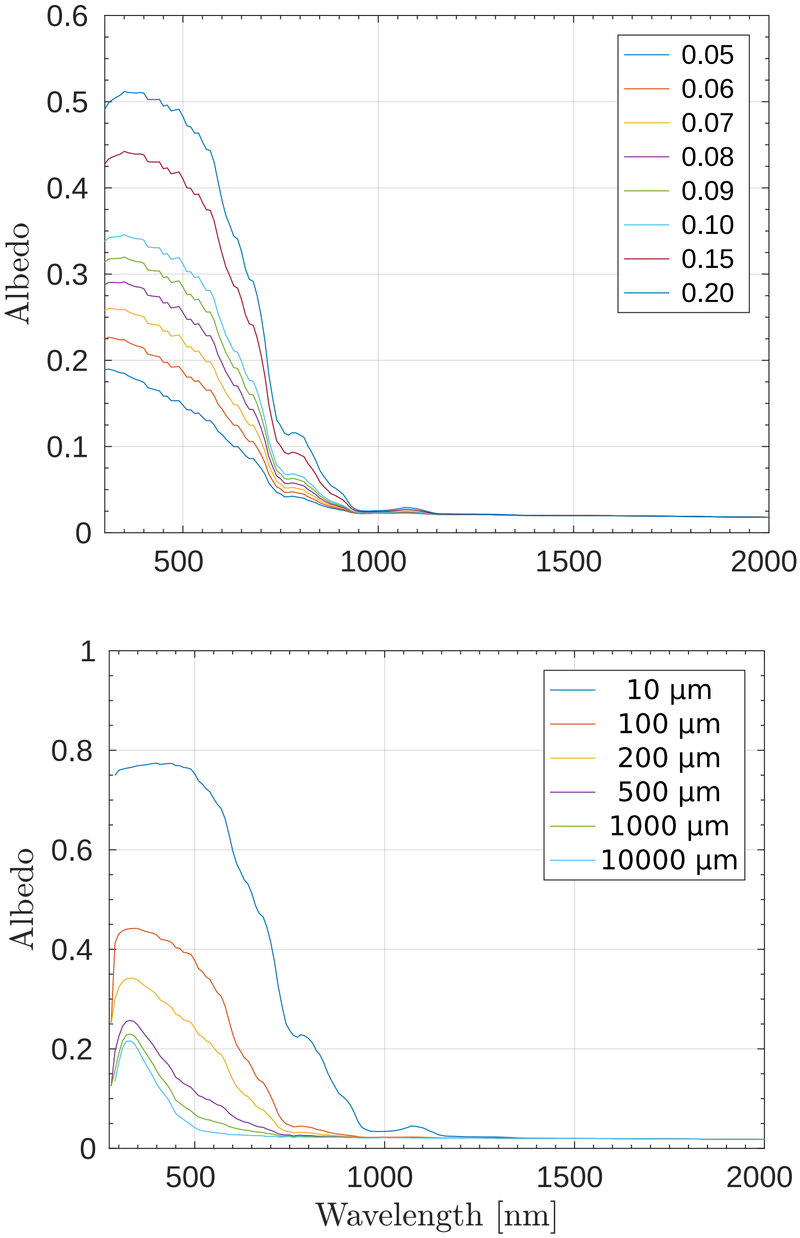

Figure 2.11: The spectral albedo of sea ice, when varying the brine distribution. In the top panel the brine pocket radii are kept constant at 100 μm while varying their volume fraction from 0.05 to 0.2, while in the bottom panel the volume fraction is kept constant at 0.05, while varying the brine pocket radii from 10 to 10 000 μm. Air inclusions are left out.

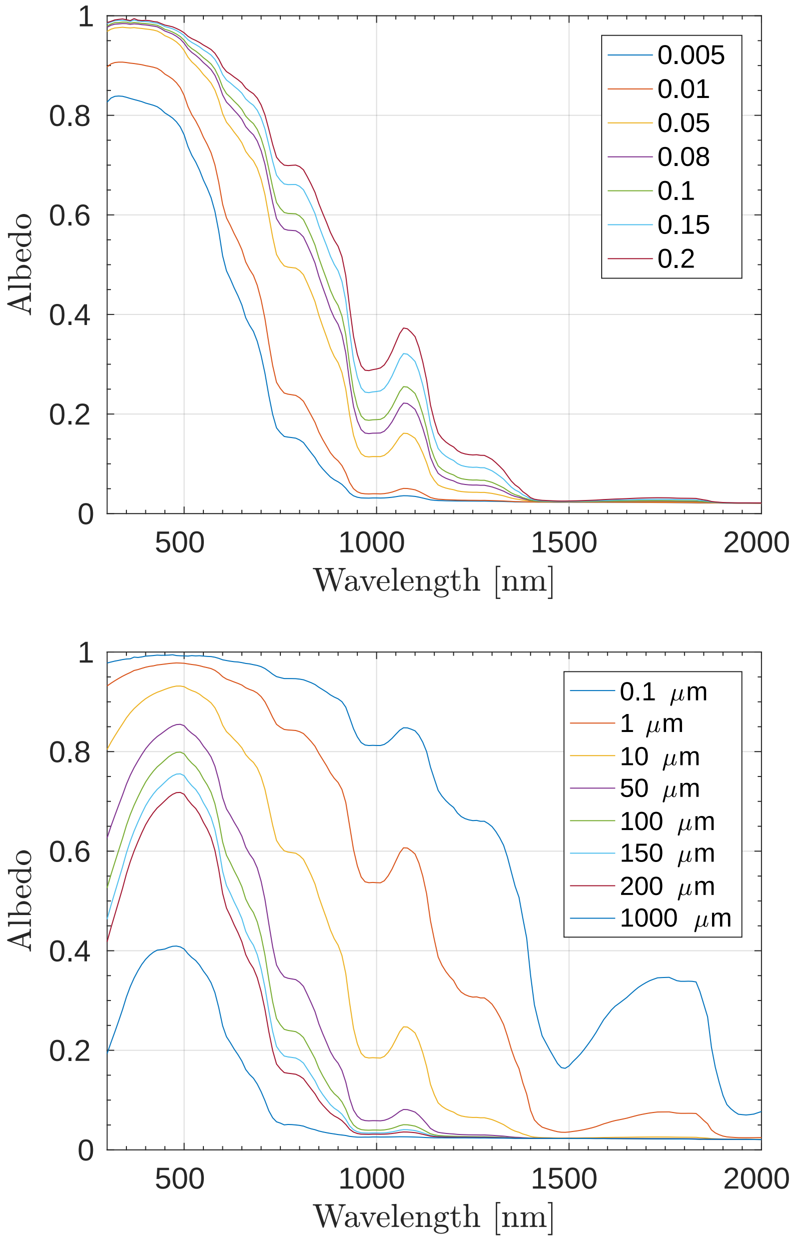

Figure 2.12: The spectral albedo of sea ice, when varying the bubble distribution. In the top panel the bubble inclusion radii are kept constant at 100 µm while varying their volume fraction from 0.005 to 0.2, while in the bottom panel the bubble volume fraction is kept constant at 0.05, while the bubble radii is varied from from 0.1 to 1000 µm. Brine pockets are left out. The values are not realistic, but it allows us to assess the overall trend.

2.3.3 Clouds

Clouds are complex structures, and they play an important role in the global climate [Lamb and Verlinde, 2011]. The total cloud fraction on global scale is estimated to 0.68 ± 0.03, when considering clouds with optical depth $\kappa > 0.1$ [Stubenrauch et al., 2013]. The fraction increases to around 0.73 when thin, subvisible cirrus clouds are included, and decrease to 0.56 when only clouds with $\kappa > 2$ are considered.

When adding parameters for cloud properties, we have to know the typical identities for the different cloud types, and/or how to estimate these. The cloud height, thickness, volume fraction and droplet size distribution must be considered.

As shown in Figure 2.4, the imaginary part of the refractive index, and hence the absorption coefficient of both pure ice and water exhibit a similar wavelength dependency. The huge albedo difference between sea ice and water (Figure 2.7) is therefore related to the physical characteristics of the sea ice. For cloud constituents this means that it is only the shape of the particle, and not whether it is ice or water that determines its scattering and absorptive properties.

Based on altitude, we divide clouds into three main categories: strato, alto, and cirro, corresponding to low (below 2 km), mid (2-7 km), and high (above 7 km) heights [Lamb and Verlinde, 2011]. They exhibit different properties, some of which are shown in Table 2.3.

Table 2.3: Typical values for physical properties of three different cloud categories. LWC stands for liquid water content, IC for ice content. N is the number of particles per unit volume. Values from Thomas and Stamnes [2002], Lamb and Verlinde [2011].

Cloud	Type	Altitude [km]	Typical droplet radii [μm]	LWC/IC [gm^{-3}]	N [cm^{-3}]
Cirro	Cold	> 7	85	0.03 – 0.064	0.025
Alto	Warm	2-7	6.25	0.4 – 4	400
Strato	Warm	< 2	10	0.65 – 1.0	250

We differ between warm clouds which are made up from liquid water droplets, and cold clouds, made up from either ice crystals, or a combination of ice and water constituents. The physical parameters of warm cloud particles follow to some extent a typical size scheme, and although their size variation is continuous, the water droplets can be divided into different categories: A haze drop is typically ∼1 μm in diameter, a cloud drop ∼10 μm, a drizzle drop 100 μm, and a raindrop ∼1 mm [Lamb and Verlinde, 2011].

As we see in Figure 2.13, clouds have little to no effect on the surface albedo of snow, for an incident zenith angle of 45°. We saw similar results for larger zenith angles, with only a slightly higher albedo for zero clouds.

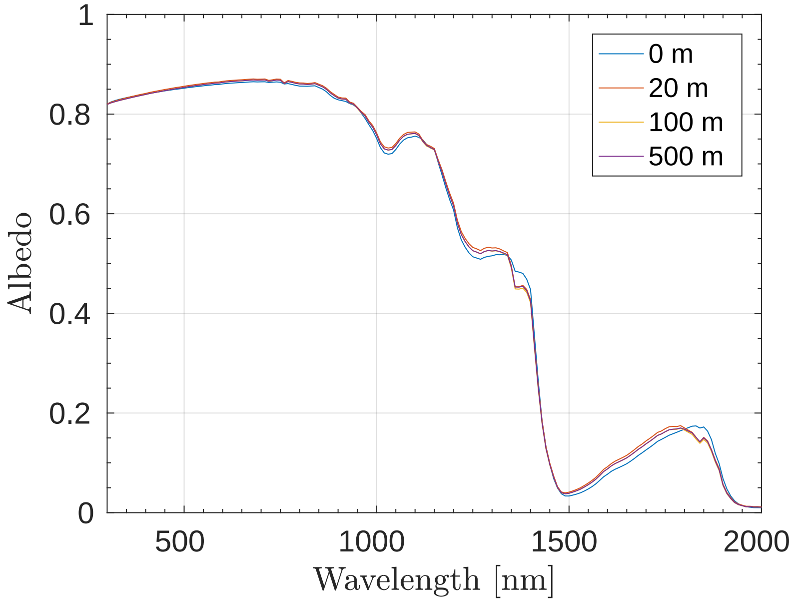

Figure 2.13: The spectral albedo of snow, for various cloud thicknesses, varying from 0 to 500 m. SZA: 45°

2.3.4 Atmosphere: Gases and aerosols

The atmosphere comprises mainly of various molecular gases, where nitrogen (N_2), oxygen (O_2), argon (A), carbon dioxide (CO_2) and water vapour (H_2O) are the most abundant [e.g. Bohren and Clothiaux, 2006, Lamb and Verlinde, 2011]. These molecular constituents contribute to Rayleigh scattering ($g \approx 0$), and does also contribute to absorption, as can be seen in Figure 2.2. Ozone (O_3) is less abundant, but should be mentioned due to large absorption in the UV. In addition, atmospheric suspended particles, aerosols, are a common constituent. Aerosols are in general particles in the range of around 10 nm to several microns (μm), arising from both natural and anthropogenic emission [Lamb and Verlinde, 2011]. These particles are also responsible for scattering and absorption, all depending on their inherent optical properties (IOPs), and will contribute to a variation in the intensity flux. To limit the extensiveness of this thesis however, aerosols are mainly left out.

2.4 Description of our model

We have used a multistream radiative transfer code, AccuRT, which consists of two adjacent multilayered strata that allow for different refractive indices. Both the number of layers within the slabs, and the number of streams (i.e., computational angles) can take a wide range of user specified values. The model solves the radiative transfer equation numerically [Hamre et al., 2017].

The shape of the physical parameters within the slabs (e.g., snow grains, brine pockets, bubbles, cloud droplets) are approximated by those of spheres [Hamre et al., 2004]. In the case of snow crystals, they quickly loose their delicate shapes and facets due to local weather conditions and metamorphism, which makes the grains both rounded and quite uniformly shaped [Wiscombe and Warren, 1980]. In other words an unproblematic assumption for the fallen snow, or in warm clouds were the liquid water droplets naturally tend to a rounded shape.

For clouds consisting of ice crystals however, determination of reliable optical properties is considered difficult [Thomas and Stamnes, 2002], as the ice crystals take on a wide variety of shapes and sizes, depending on parameters such as temperature and vapour density [Lamb and Verlinde, 2011], and that theses geometric variabilities have a great influence on the anisotropic reflectance factor [Dumont et al., 2010].

The main issue with the sphere-approximation has been that a sphere with equal volume to the crystal has too little surface area and therefore a reduced scattering effect, while a sphere with equal surface area will have too large volume, leading to too much absorption [Grenfell et al., 2005]. However, a way to succumb this, is to implement the modelled cloud with a larger amount of smaller spheres, so that the cloud contains the same total volume and area, as the real cloud [Grenfell et al., 2005].

When rendering reflectance outputs from a snow configuration, AccuRT does not include the direct beam of upwards irradiance $F_{\uparrow}$, but rather treats it is a diffusely reflective surface. This is a useful approximation, as the reflected specular solar beam would lead to an infinitesimal solid angle of very high intensity, but still lets us investigate the angular distribution of the reflected light.

In the model, the refractive index of the atmosphere is set to 1[4], while for water and ice it is extremely wavelength dependent (Figure 2.5), and the real part (determining the phase velocity in the medium) varies from about 1 to 1.6. For UV, VIS and NIR wavelengths, it is almost constant with a value of about 1.3. Tabulated data for the real and imaginary refractive index from Warren and Brandt [2008] is used for modelling. Due to the different refractive indices in atmosphere and water (Section 2.2.1), the total number of streams in the atmosphere spanning the whole sky will correspond to a cone smaller than 2π sr in the water (the hemisphere has a solid angle of 2π sr). This can be visualized by assessing Figure 2.3, where light entering a medium of higher refractive index, will be refracted into a more narrow angle relative to the surface normal. Radiance upon refraction yields that the radiance is increasing when light travels to a medium with larger refractive index: $\frac{L_i}{L_t} = \frac{d\Omega_t}{d\Omega_i} = \frac{1}{n^2} \rightarrow L_t = n^2 L_i$, where subscripts L_t and L_i denotes transmitted and incident radiance, and n the refractive index of the medium.

To ensure enough streams outside the cone, the following relation establishes the number of streams used in the lower slab:

$$N_l = k_1 \cdot N_u \cdot n_{max}^{k_2}. \tag{2.26}$$

Here N_l is the number of streams in the lower slab, k_1 and k_2 are two parameters assigned 1 and 2 respectively (a result of trial and error by the model makers), N_u the number of streams in the upper slab, and n_{max} the largest refractive index within the specified wavelength range.

Being a one-dimensional plane parallel model, the different strata in AccuRT is treated as infinite slabs, meaning every layer configuration appends to the whole infinite slab. This makes modelling of a fragmented surface

---

[4] The actual value is listed as 1.000293, at STP [Hecht and Zajac, 1974]

structure or cloud cover impossible. The plane parallel approach also gives rise to precaution when we run the model for large solar zenith angles. As the zenith angle increase, the total amount of atmosphere that the light needs to pass through also increase, as shown in Figure 2.14. For real life scenarios the curvature of the earth sets a threshold for this distance, while in the flat earth model, the atmosphere thickness will approach infinity for large enough zenith angles. To avoid conflict with the infinite atmosphere, we limit our incident zenith angles to a maximum of 75°.

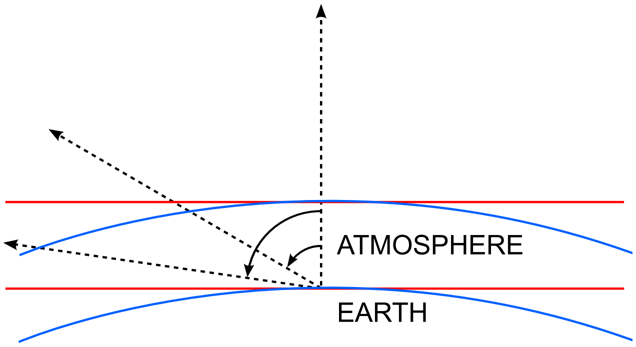

Figure 2.14: Simplified sketch of how the thickness of the atmosphere deviates increasingly for increasing zenith angles, between the curved (blue lines) and flat (red lines) approach. For large zenith angles the thickness of the plane parallel atmosphere becomes unnaturally large. The layer thickness and curvature ratio is exaggerated.

An other limitation of the plane parallel model, is that surface roughness and surrounding topography are left out, while they might influence the light conditions. Measurements of the anisotropic reflectance factor of Antarctic snow has been made by both Warren et al. [1998] and Hudson et al. [2006], where South Pole sastrugi (snow ridges created by prevailing wind erosion) are pronounced due to strong continental winds. Antarctic weather conditions are however not to be assumed representable to what can be seen in the Arctic, due to very different local characteristics (accumulation rate, temperature, winds, etc.), but effects may be comparable to what we can model with the plane parallel approach.

The upwelling irradiance of snow $F_{\uparrow}$ is defined to only have a diffuse component, and is therefore a function of only observing angles, ϕ and θ, while for sea ice, the direct component of the reflected solar beam is included, so it is a function of both ϕ, θ and θ_0. As the solar beam is defined as irradiance coming from an infinitesimal solid angle, its intensity can be thought of as that of a delta function, meaning an infinitely large value for an infinitely small extent. The upwelling radiance ($L_\uparrow$) is therefore also consisting of only the diffuse components, as the direct component would be extremely large and only existing in a infinitesimal dot.

2.4.1 Basis for model inputs

Choosing realistic values when running our model is essential, when we want to apply our results to real life conditions. We therefore turn to the work by some of the eminent researches within the fields of snow, sea-ice and atmospheric sciences, and also run our model with various inputs to test its sensitivity.

Warren [1982] points to several studies finding that snow albedo is not dependent on the snow density, but rather that the density is directly dependent on snow grain size, where density normally increases with increased grain size. Isolation of the two parameters in showed that the snow albedo remained constant for constant grain size, while varying the density.

The importance of acknowledging the snow pack as a stratified medium is emphasized by Colbeck [1991], as the different layers exhibit a range of different properties affecting the coupled atmosphere surface system accordingly. These strata variabilities include snow grain distribution and size, and snow density, and arise from both precipitation and metamorphic processes due to weather- and topographical conditions. In this thesis however, we will strive to isolate the various parameters, to observe the isolated response, and will therefore mostly limit ourselves to single slab configurations.

When we vary the solar zenith angle, we need to keep both the plane parallel atmosphere restrictions (Figure 2.14), and the realistic angles of incidence for arctic regions, mentioned in Section 2.1.2, in mind. This leaves an interval of roughly 30°, from SZA 45° to 75°. We will mostly keep within this interval, but we will also look at the response from zenith angles closer to zenith when we want to assess an overall trend.

2.5 Remote sensing

The ability to perform remote sensing observations from space revolutionized large scale data collecting in 1972 [Schowengerdt, 2006]. The method is still by far a invaluable tool for gaining knowledge about the state of the earth, and is especially valuable for measuring surface and atmosphere properties in otherwise inaccessible and isolated areas. As stated by Stubenrauch et al. [2013], satellite observations are also the only way to provide continuous and comprehensive surveys of atmosphere characteristics over the entire globe. citetrobinson1993global emphasizes the importance of accurate large-scale monitoring of the global snow cover for understanding details of climate dynamics and climate change.

Typical ranges for optical remote sensing often lie between 0.4 and 2.5 μm [Richards and Richards, 1999], in the visible and near infrared parts of the spectrum. However, most remote sensing sensors measure the reflected radiation of only a few wavelength bands [Richards and Richards, 1999, Dumont et al., 2010]. As we have noted before, remote sensing instrumentation often perform measurements within a limited field of view (FOV), i.e. within a narrow solid angle. Knowledge of the angular distribution for narrow wavelength bands is therefore of highest interest.

Chapter 3

Methods

3.1 Field work

Every spring, a glaciology team from the Norwegian Polar Institute conducts a survey of the glaciers in vicinity of Ny-Ålesund on Svalbard. In April 2016, I was able to join them for a week, collecting data with a radiometer setup. The map in Figure 3.1 indicates the locations where we performed measurements. From east to west: Austre Brøggerbreen, Midtre Loveenbreen, and two locations on Kongsvegen. In the lower right corner, Tellbreen, close to Longyearbyen is indicated. The team collected a wide variety of data for monitoring Ny-Ålesund glaciers mass balance and movement, through ice core samples, snow pit analyses, permanent weather station inspections, etc., while we concentrated on sampling radiation data.

Figure 3.1: Map of our sampling locations on Svalbard [Norwegian Polar Institute, 2016]. The glaciology survey was preformed at different locations, marked with red dots in vicinity of Ny-Ålesund (upper left). In addition we had one day of field work at Tellbreen, close to Longyearbyen (lower right).

3.1.1 Equipment

For collecting data on the Svalbard glaciers, we used a setup with three radiometers from TriOS, all measuring in the visible and near infrared parts of the spectrum [Ramses, 2010]:

- **Ramses-ACC 80E2 Cosine irradiance sensor** Light is collected by a plane diffuser, and detected by an optical fibre. The signal is weighed by the cosine response of the angle of the incident light.
- **Ramses-ASC 84EE Scalar irradiance sensor** Light is collected by a spherical diffuser, and detected by an optical fibre. It collects light from a whole hemisphere, corresponding to a solid angle of 2π.

- **Ramses-ARC 810C Radiance sensor** Light is collected from a solid angle in front of the sensor, corresponding to a 7° field of view.

The Ramses sensor are hyperspectral radiometers, meaning they collect radiation through numerous of narrow bands, with an optical module from Zeiss [2017]. Details on the sensors are shown in Table 3.1, while a sketch of the optical principle of operation is depicted in Figure 3.2.

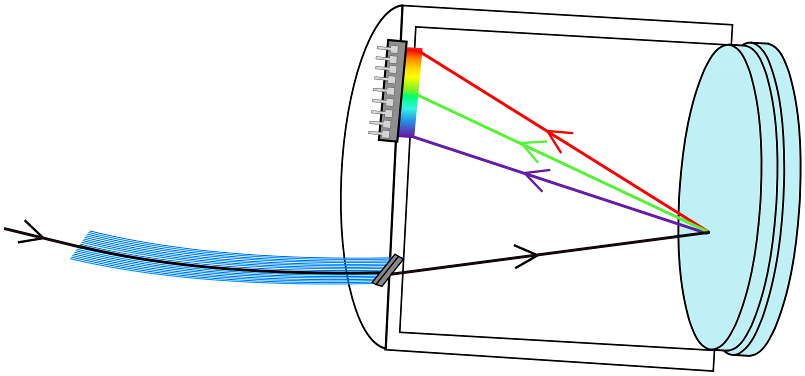

Figure 3.2: Simplified sketch of the optical principle of the Zeiss module in the Ramses radiometers, based on a figure in Ramses [2010]. The received light is transmitted through an optical fibre bundle (lower left), and enters a chamber with a concave flat-field grid (right). Here the rays are dispersed onto a 256 channel photo diodic array (upper left in chamber), which converts the information into electric signals.

Table 3.1: TriOS Ramses radiometers specification, values from Tveiterås [2013]

Name	Function	Spectral range [nm]	Spectral peak[1] resolution [nm]	Accuracy	FOV [°]	Operating range [°C]
Ramses-ACC 80E2	Cosine response irradiance sensor (flat)	319.5 - 951.8	0.3	better than 6-10%		-10 to + 50
Ramses ASC 84EE	Scalar irradiance sensor (spherical)	320-900	0.3	better than 6-10%		
Ramses-ARC 810C	Hyperspectral radiance sensor	319.1 - 951.8	0.3	better than 6%	7	-10 to + 50

---

[1] The intensity peak of a certain wavelength has a resolution of 0.3 nm, while the width of the corresponding intensity curve has a resolution of 10 nm.

3.1.2 Setup

We used a compact and mobile TriOS radiometry setup scheme, consisting of three sensors mounted on a metallic plate, attached to a tripod. The two irradiance sensors were upwards facing, collecting downwelling irradiance, while the radiance sensor pointed towards the ground in a 45° angle. We collected radiation data at 15 seconds intervals. Our setup is shown in Figure 3.3, with an overview in the top panel, and a close up in the bottom panel. Both photos were taken on Kongsvegen glacier at 78.765°N, 12.905°E, on April 13th, 2016. We emphasized choosing large, open and pristine sampling locations, to reduce disturbance from surrounding topography, and had minimal activity in the close vicinity of the setup.

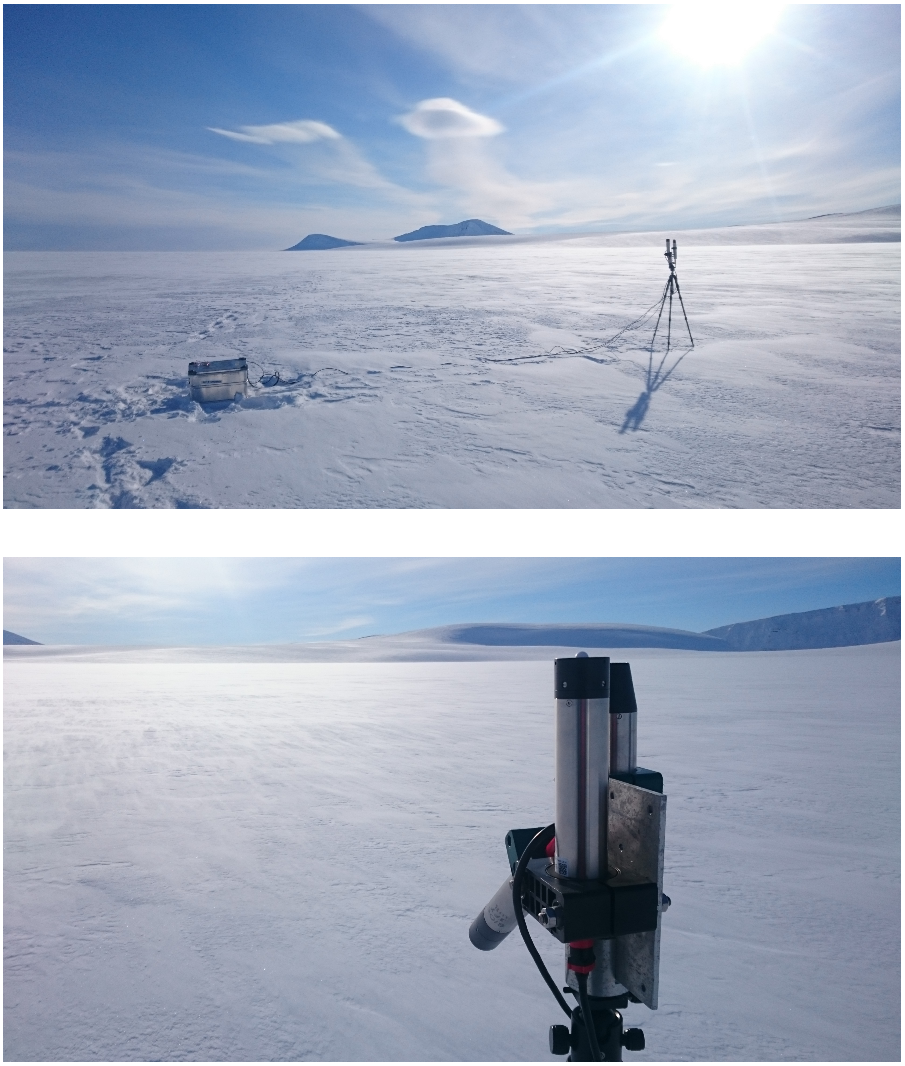

Figure 3.3: Photos from Kongsvegen, April 13th, 2016, showing an overview of the whole radiometer setup (top), and a close up (bottom). The two irradiance sensors are mounted to a metallic plate in equal height, while the radiance sensor is facing the ground in a 45 ° angle, pointing towards the solar azimuth angle. We used this scheme for all samplings on Svalbard in April 2016.

As Tellbreen (78.252°N, 16.138°E) is located in between a few ridges, some surrounding topography was inevitable (see Figure 3.4).

Figure 3.4: Photo from Tellbreen, April 16th, 2016.

3.1.3 Time and weather

An overview of the sampling specifications is shown in Table 3.2. The table includes time and locations, sampling duration, cloud cover assessment, air temperature, and solar zenith and azimuth angles. Due to technical issues, only half of the days of field work resulted in complete measurement series, these are shown in the table. See Appendix C.1 for details. As we also can see in Figures 3.3 and 3.4, we had nice weather conditions with no precipitation on both April 13th and 16th, while the first day of field work, April 9th, was dominated by low clouds and fog, and light snow accumulation.

Table 3.2: Sampling specifications, Ny-Ålesund, April 2016. Solar zenith and azimuth angles were determined with the aid of a solar positioning calculator, National Oceanic and Atmospheric Administration [2016]. Daylight saving time is accounted for.

Date	Local time UTC: +1	Location	Lat [°]	Long [°]	Clouds	ppt.	t [°C]	SZA [°]	SAA [°]	Comment
09.04.	14:05-14:55	Austre Brøggerbreen	78.872	11.913	low: 7/8	light snow	-1	68.8-69.6	194.1-207.2	Some surrounding topography
13.04.	14:19-15:10	Kongsvegen	78.765	12.905	high: 5/8	none	-14	69.9-71.6	194.9-217.5	
16.04.	14:21-14:26	Tellbreen	78.252	16.138	high: 4/8	none	-15	68.7-68.8	202.6-203.1	Some surrounding topography

3.1.4 Uncertainties

We used a leveller instrument when positioning our setup on the glacier snow. It consist of a cylindrical, translucent cage enclosing a viscous fluid, influenced by the overall gravity field. It does therefore not align with the potential local surface incline. In addition to the uncertainty arising from eye evaluated alignment, and uncertainties within the leveller itself, the relative solar zenith angle will be influenced by the deviation from a horizontal surface.

Uncertainty in recorded data might also arise from sensor calibration errors.

3.2 Modelling

We will test how well our model agrees with previously established optical properties of snow, ice and sea ice. In essence we want to establish how different physical properties within the media affects the optical properties, and which parameters play the lead role.

One key point we are examining the anisotropic reflectance factor, R (Equations 2.15 and 2.18) for snow and sea ice, mainly observing its response to varying incident zenith angles, for three selected wavelengths: 500, 800 and 1100 nm. Other wavelengths will occasionally appear, for example when we make an approach to modelled results of the ARF from Warren et al. [1998] and Hudson et al. [2006].

We will vary the parameters in our snow and ice in accordance with realistic values (Section 2.4.1).

3.2.1 Snow

As we have seen in Section 2.3, snow is a highly complex medium. Various external variables as accumulation rate and type, prevailing wind, topography and temperature affect the snow properties. It is also a distinctly stratified medium, where the different layers can exhibit extreme variations in terms of density, snow grain size. We will assess data collected in the field and essentially how the in situ reflectance is affected by changing weather conditions. We will

3.2.2 Sea ice

We look at how varying physical aspects in the sea-ice affects it reflectivity. We want to investigate how brine and bubble content in the ice floe will affect the albedo and reflectivity of the surface. How sensitive is the model to the different layers? If the second layer is not affecting our results to much, we will simplify our modelling by removing the layer. We therefore run our model with 1 m thick ice, with the run with a single layer having the same physical properties as the top layer in our two-layer run. The brine volume fraction is set to 0.05 in both ice types. As albedo tend to increase with decreasing inclusion size [Light et al., 2003, Perovich, 1996], the configuration with the highest number of small inclusions has a higher albedo. Since we want to see the isolated effect of changing one parameter, we choose to stick with a simplified configuration of 1 layered sea ice.

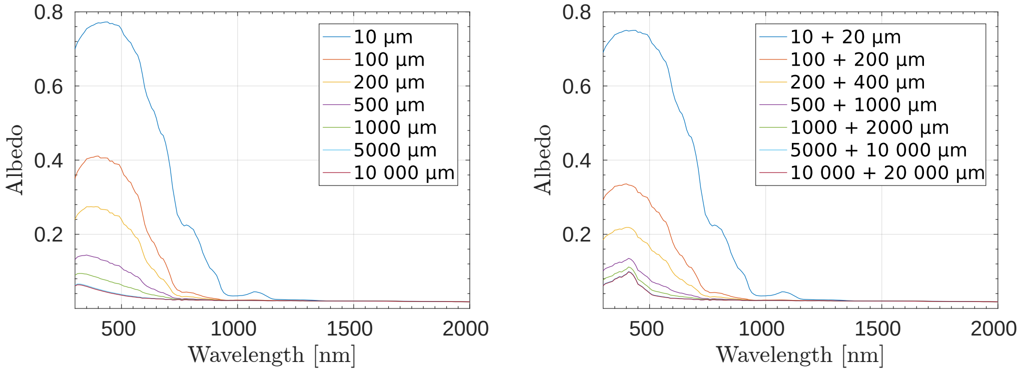

Figure 3.5: Comparison of the albedo response for varying brine radii in 1 m thick ice, with one layer (left), and two layers (right). The bubble radii in the left panel are the same as in the top 20 cm in the right panel, while the bottom 80 cm in the right panel has twice the bubble size of that in the top layer. The brine volume fraction is 0.05 in both panels.

3.2.3 Clouds

We know that clouds affect the radiation budget of the earth, due to both scattering and absorption. They may consist of water constituents in both gaseous, liquid and solid state, as well as aerosols and natural and artificially originating pollutants.

3.2.4 Interpreting the polar plots

In Chapter 4 the anisotropic reflectance factor R is plotted for different surfaces and parameters in polar contour plots, with code adapted from Garrad [2016]. The plots depicts how the reflected radiance deviates from the average value (unity), in different observing polar and azimuth angles (θ, ϕ), where the center of the plots represents a observation polar angle of 0°, looking downwards (nadir). The concentric rings indicates an increasing viewing polar angle, drawn every 22.5° from center. A polar angle of 90° represents horizontal observations. See Figure 3.6 for a schematic overview.

As mentioned in Section 2.2.4, we have varied the solar zenith angle, while always keeping the solar azimuth angle at 0°, i.e., north in the plots. This means that light reflected in the direction of the sun will be on the 0-180° line in the upper half of the plots. An azimuth angle of 180° represents reflectance in the principal plane, in opposite direction of the sun. We have normalized the distribution according to Equation 2.18, as we are interested in the pattern of the angular distribution, and how the surface deviates from a Lambertian surface in various viewing angles. A value of 1 therefore corresponds to perfect diffuse reflection, a higher relative reflectance value means a positive deviation, while a lower value indicates a negative deviation. These characteristics are translated to respectively yellow and blue in our plots, with a yellow-orange-green-blue gradient. The scale is fitted to each plot, as the distribution varies. In the example plot in Figure 3.6, the maximum deviation is negative, and can be observed at horizontal grazing angles ($\theta = 90°$) for all azimuth angles ϕ, with a value of about 0.65 times the average value. The maximum deviation is observed at nadir, at about 1.1. times the average value. The reflection is close to Lambertian for observing polar angles between 40 and 50°.

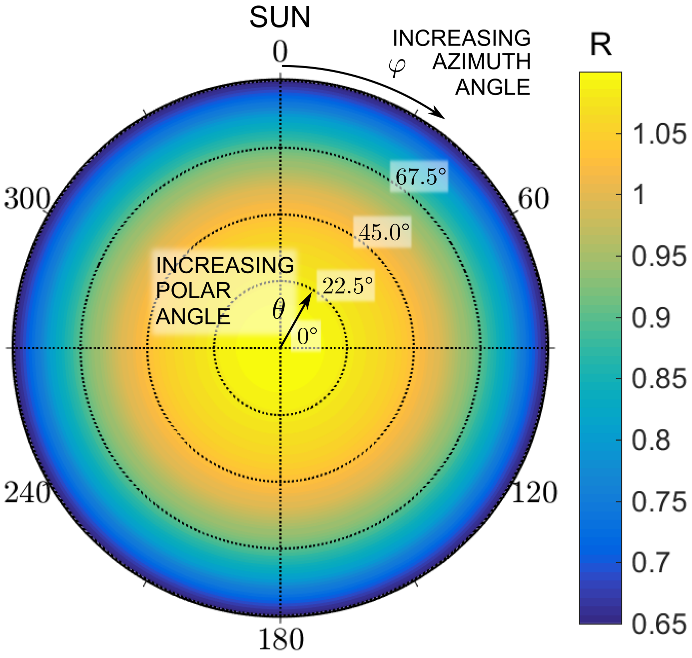

Figure 3.6: How to interpret the polar plots in Chapter 4: Observing polar angle θ increaces from the center (0°, nadir direction) towards the horizon (90°). Azimuth angles ϕ increase clockwise from the direction of the sun (0°), around the perimeter.

Chapter 4

Results and discussion

4.1 The Anisotropic reflectance factor

The optical properties of snow and ice varies with their inherent properties. As seen in Sections 2.3 variations in snow grain size, and sea ice bubble and brine inclusion has a significant effect on the albedo. For this analysis we have chosen three wavelengths in the visible and near infrared parts of the spectrum (Figure 2.2): 500, 800 and 1100 nm. As can be seen in Figure 2.7, the value of fine grained snow albedo is close to 1 at both 500 and 800 nm, while it has a local maximum value of about 0.65 at 1100 nm, before it drops further into the infrared. Sea ice albedo has a maximum value of 0.8 at 400 nm, and 0.75 at 500 nm. At 800 nm the value is about 0.25, and drops almost linearly towards 0 at around 950 nm, before exhibiting a small peak of value 0.05 at 1100 nm.

4.1.1 ARF of snow

How the anisotropic reflectance factor R responds to variations in zenith angle, snow grain size, and snow thickness are presented in this section. We start by assessing what happens to the angular reflectance distribution of snow, when the incident irradiance beam changes from $\theta_0 = 0°$ to $\theta_0 = 45°$, shown in Figure 4.1. In the left panels the wavelength of the light is 500 nm, while in the right it is 800 nm. We see that for incidence from zenith (top panels), the anisotropic reflectance factor R has a central maximum intensity centered symmetrically around nadir, at about 1.1 times the average value for both wavelengths. The intensity falls off from $\theta = 0$ towards the horizon, where the largest deviation from the average value is seen. For 500 nm the minimum value is about 0.65 times the average value, while for 800 nm it is about 0.4. As we have more diffuse light from atmospheric Rayleigh scattering coming from all directions at shorter wavelengths, the maximum deviation from unity is smaller for 500 nm than for 800 nm.

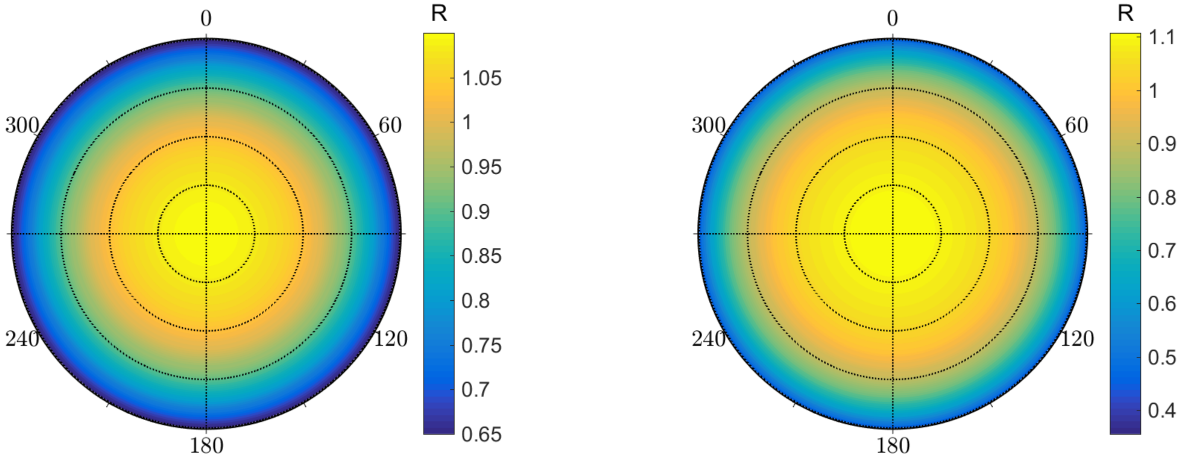

(a) λ: 500 nm, SZA: 0°

(b) λ: 800 nm, SZA: 0°

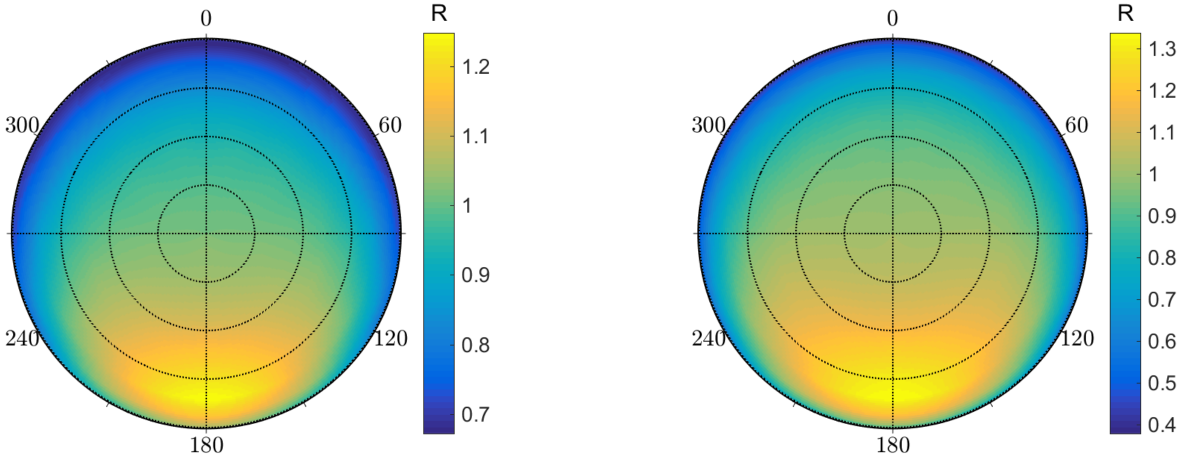

(c) λ: 500 nm, SZA: 45°

(d) λ: 800 nm, SZA: 45°

Figure 4.1: The anisotropic reflectance factor for snow, when the sun is in zenith (top panels), and at 45° (bottom panels).

The value of $R(\theta, \phi)$ is about 1 ± 0.05 in polar observation angles θ

between 40° and 60°, for all azimuth angles, in both top panels; meaning the deviation from isotropic reflection is about 5% in this range.

In the bottom panels of Figure 4.1 we see $R(\theta, \phi)$ for 45° incidence (the smallest realistic solar zenith angle for arctic regions, see Section 2.1.2). Here we see the intensity peak in the angular distribution is shifted in the forward direction for both wavelengths, located at about $(\theta, \phi) = (75°,180°)$. The intensity peak is in other words not a result of specular reflection (as seen in Figure 2.6), but rather an effect from the internal scattering within the snow pack, where the particles are very large compared to the wavelength of the light. This means a positive asymmetry factor, with prevalent forward scattering. Light penetrating into the snow are therefore more likely to be scattered further into the snow in its forward direction, when they first have travelled beyond the interface. Photons leaving the snow after only one scattering event will therefore have a higher probability to be scattered in the horizontal direction, since this is the most probable scattering direction above the snow/atmosphere interface.

The snow pack consists of a 1 m thick, homogenous, fine grained layer of older snow (radii 200 μm), with density 300 kgm^{-3}.

Varying the solar zenith angle

Snow albedo increases with solar zenith angle, as show in Figure 2.9, and it also has an effect on the ARF, as seen in Figure 4.1. In Figure 4.2 we investigate how the reflectance distribution is affected by increasing the incident zenith angle further (top to bottom), at three different wavelengths: 500, 800 and 1100 nm (left to right).

We see that the forward intensity peak is increasing with increasing zenith angles, for all three wavelengths, in accordance with the trend we saw in Figure 4.1.

The forward intensity peak is however only prominent for large observing polar angles θ, and as incident zenith angles are increasing, the forward intensity peak moves closer to the horizon, opposite the sun in the principal plane.

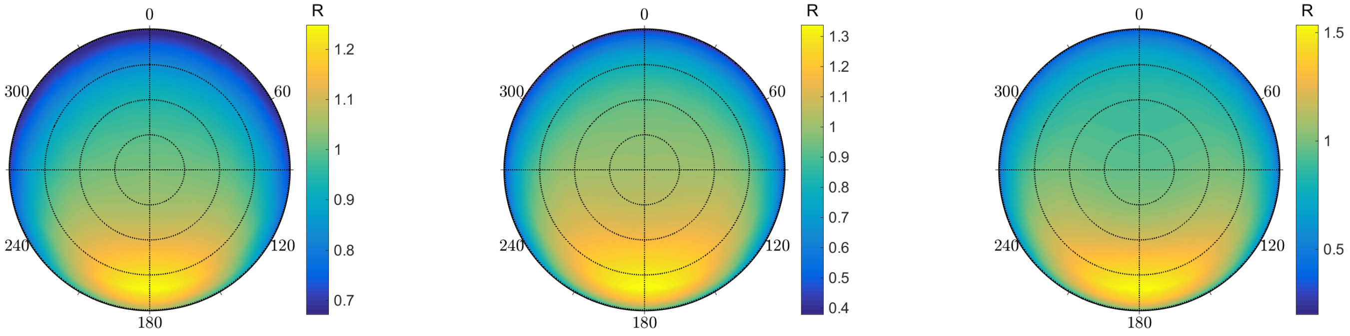

(a) λ: 500 nm, SZA: 45°   (b) λ: 800 nm, SZA: 45°   (c) λ: 1100 nm, SZA: 45°

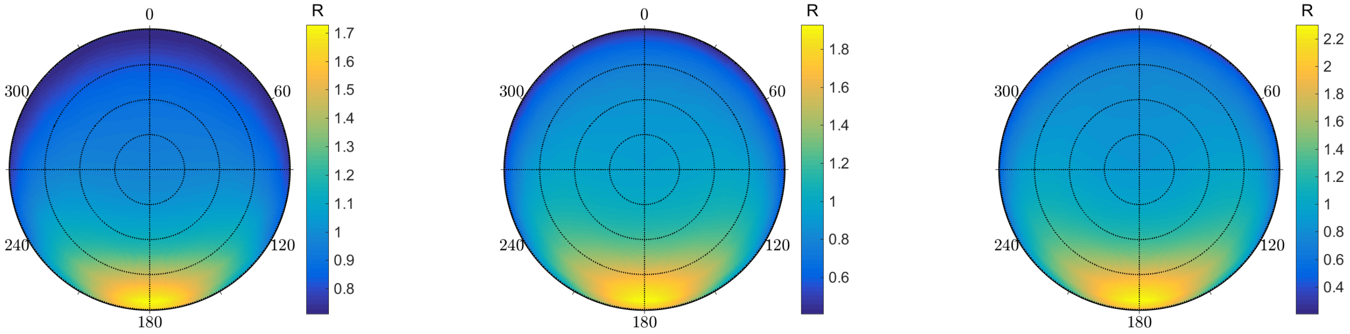

(d) λ: 500 nm, SZA: 55°   (e) λ: 800 nm, SZA: 55°   (f) λ: 1100 nm, SZA: 55°

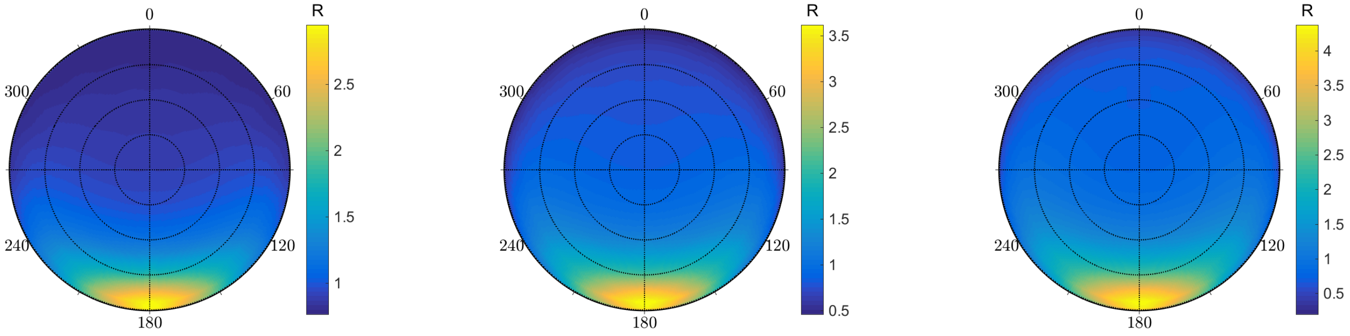

(g) λ: 500 nm, SZA: 65°   (h) λ: 800 nm, SZA: 65°   (i) λ: 1100 nm, SZA: 65°

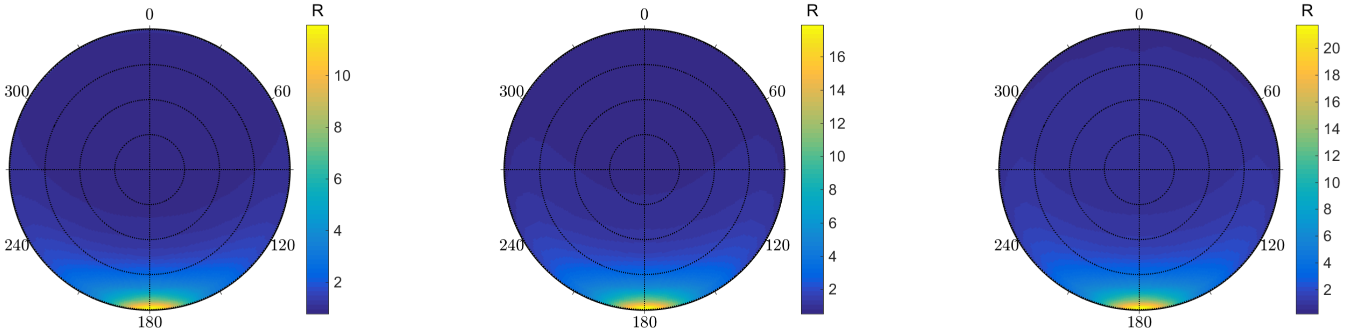

(j) λ: 500 nm, SZA: 75°   (k) λ: 800 nm, SZA: 75°   (l) λ: 1100 nm, SZA: 75°

Figure 4.2: The anisotropic reflectance factor of snow for increasing zenith angles, $\lambda = 500$ nm in the left panels, 800 nm and 1100 nm i right panels. Top panels have solar zenith angle = 45°, panels in second row 55°, third row 65°, and bottom 75°. The snow pack consists of a one meter thick homogenous layer, with density 300 kgm^{-3} and snow grain radii 200μm.

Varying snow grain size

As we have seen in Figure 2.9, the snow grain size has an large effect on the albedo. From this figure the variation seems to be linear, as the curves follow the same trend throughout the visible and NIR parts of the spectrum (with a little enhancement for the smaller grain sizes from around 1500 to 1950 nm). In Figure 4.3 we see the anisotropic reflectance function for 500, 800 and 1100 nm (left to right), for increasing snow grain radii, from top to bottom: 50, 125, 200 and 1000 µm. The zenith angle is 55°.

We see the same effect from Rayleigh scattering as previously: the range between maximum and minimum deviation is largest for long wavelengths, and smallest for shorter wavelengths. For 1100 nm the scale goes from around 0.3 towards the horizon, to around 2 in the forward maximum peak. For 500 nm the minimum value is 0.7 times the average, and the maximum 1.7.

The overall trend for light of 500 nm is that R is unchanged for all grain sizes, while for 800 nm there is a small increase in the forward intensity peak for significantly large particles. For 1100 nm the forward intensity peak is increased slightly (from 2 to 2.2 times the average value) for particles of about 200 µm, and even more (to 3 times the average value) for the largest grains.

For larger zenith angles the effect was even less pronounced, and the figures are therefore not included.

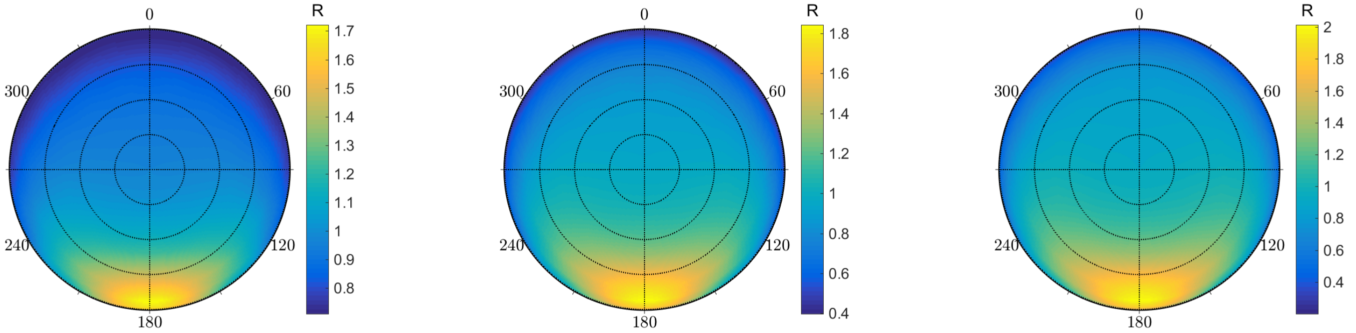

(a) λ: 500 nm, radii: 50 µm

(b) λ: 800 nm, radii: 50 µm

(c) λ: 1100 nm, radii: 50 µm

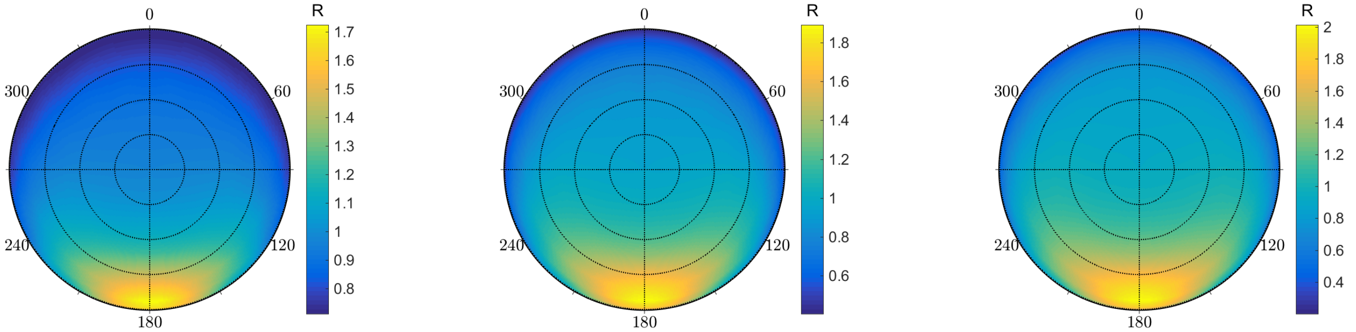

(d) λ: 500 nm, radii: 125 µm

(e) λ: 800 nm, radii: 125 µm

(f) λ: 1100 nm, radii: 125 µm

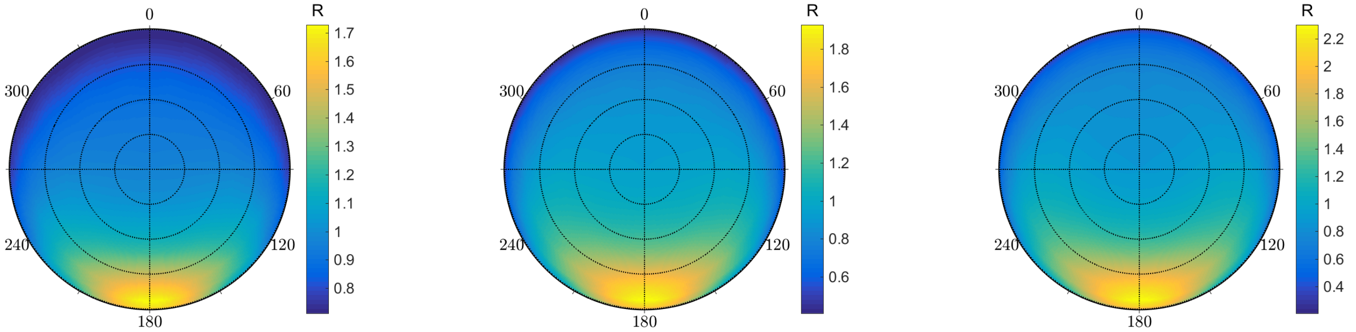

(g) λ: 500 nm, radii: 200 µm

(h) λ: 800 nm, radii: 200 µm

(i) λ: 1100 nm, radii: 200 µm

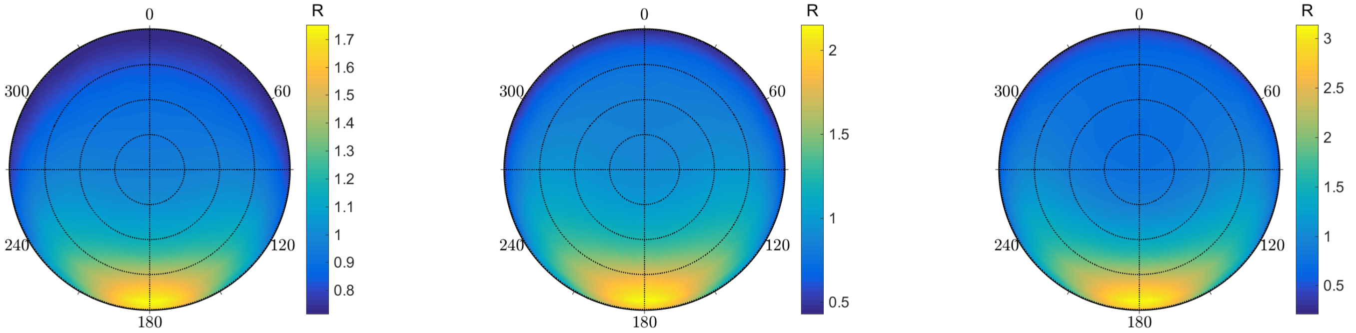

(j) λ: 500 nm, radii: 1000 µm

(k) λ: 800 nm, radii: 1000 µm

(l) λ: 1100 nm, radii: 1000 µm

Figure 4.3: Anisotropic reflectance of snow, for increasing snow grain radii, values are noted under each panel. The wavelength of the light is 500 nm, $\theta_0 = 55°$, and snow density kept constant at 300 kgm^{-3}.

ARF for decreasing snow depth

The effects of decreasing snow depth on the angular distribution of the reflected light, with solar zenith angle 40°, is shown in Figure 4.4. The wavelength of the light is 500 nm in the left panels, 800 nm in the middle, and 1100 nm in the right panels. In the top three panels the snow depth is 0.001 m (1 mm), in the second row it is 200 μm – grain radii for fine grained snow, in the third row from the top it is 50 μm – similar to new, fine grained snow, and in the bottom three panels, the snow depth is 0; or in other words: bare ice. We see that the ARF of a snow covered surface is changing remarkably as the snow depth approaches zero. In the top panels the layer is still thick enough to exhibit reflectance distribution similar to that of a thick snow layer (seen in previous figures), but as the snow cover gets thinner, the reflectance distribution undergoes a transformation from the distinct forward intensity peak seen for 1 mm thick snow (top panels, and previous figures), to a multimodal, bell shaped form, before reaching bare ice. The bell shape is most prevalent for light at 800 nm, with a snow cover of 200 μm.

For all wavelengths we see the familiar forward peak in the distribution in the top panels, which is then accompanied by a single, pronounced intensity dot at about $\theta = 45°$, for snow depths of both 200 and 50 μm. It seems that for very thin snow, we have two intensity peaks in the angular distribution of the reflected light, one arising from snow reflectance, and one from sea ice. In the bottom panels, where we have only sea ice, the forward peak we had for snow at about $\theta = 70°$, is now replaced by an intensity peak spanning over a much larger solid angle, and with a maximum value very close to unity for all wavelengths. The ARF of sea ice is thoroughly described in the next section.

The trend seems to be most prominent for solar zenith angles smaller than around 40°, at 55° the effect is only barely visible, while for 70°, it is unobservable. Some examples of this is shown in Appendix B.1.

The reflectance is fairly isotropic in the forward direction ($\phi \in [160, 180°]$) at θ of about 80° for all wavelengths. The snow is in general more reflective at $\lambda = 500$ than 800, in accordance with the reference albedo in Figure 2.7, where the albedo is close to 1 at 500 nm, and around 0.87 at 800 nm.

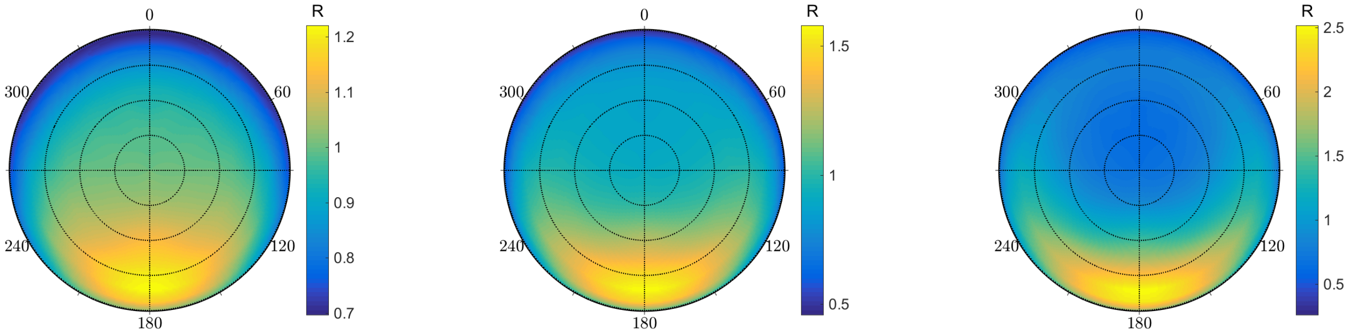

(a) λ: 500 nm, depth: 1 mm = 1000 µm

(b) λ: 800 nm, depth: 1 mm = 1000 µm

(c) λ: 1100 nm, depth: 1 mm = 1000 µm

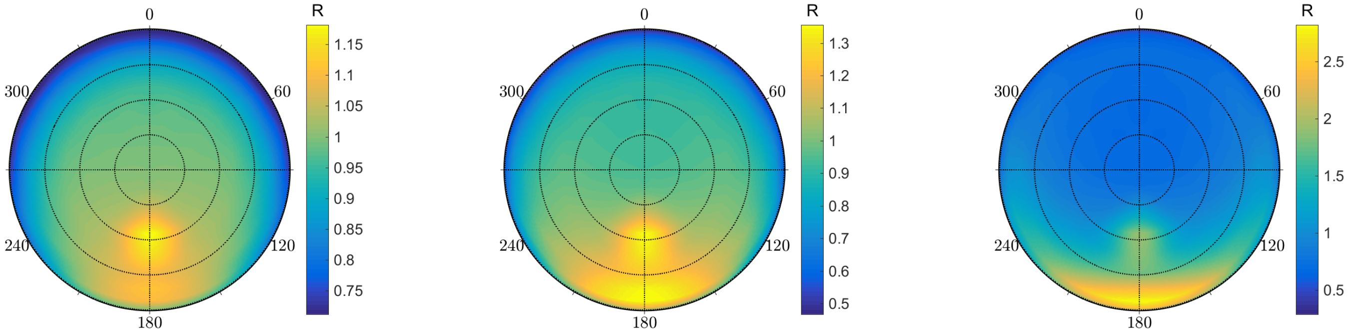

(d) λ: 500 nm, depth: 200 µm

(e) λ: 800 nm, depth: 200 µm

(f) λ: 1100 nm, depth: 200 µm

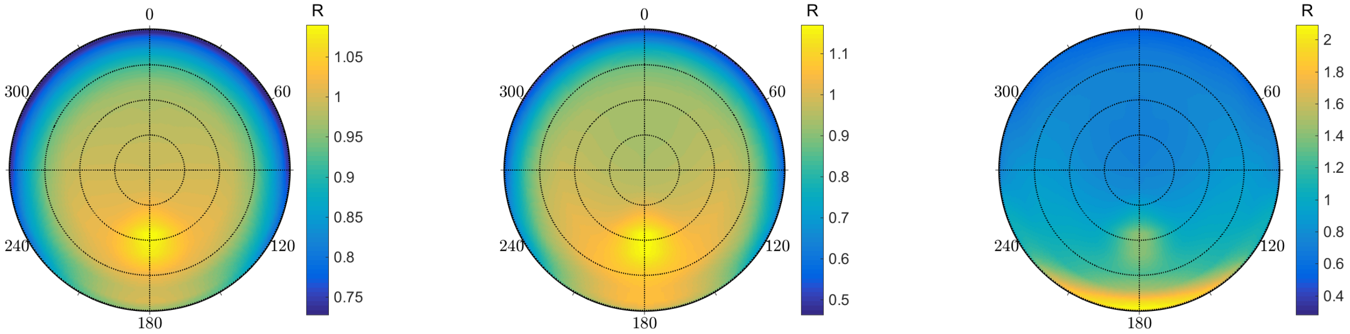

(g) λ: 500 nm, depth: 50 µm

(h) λ: 800 nm, depth: 50 µm

(i) λ: 1100 nm, depth: 50 µm

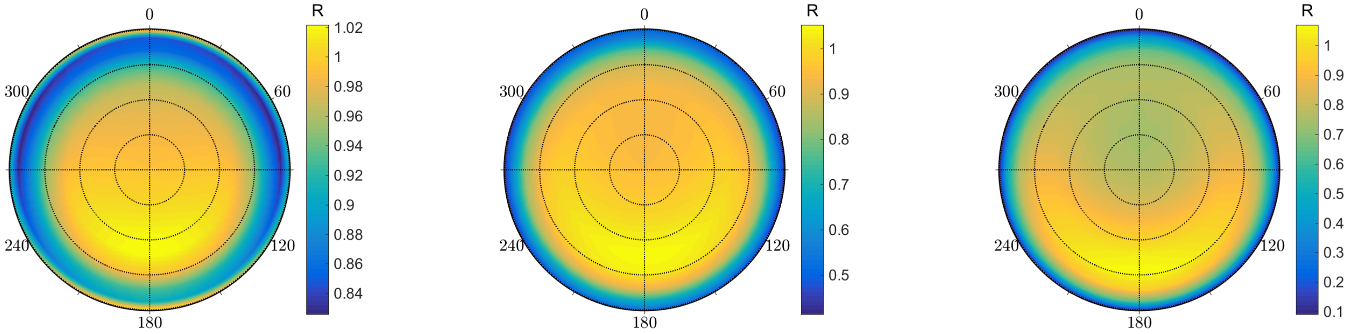

(j) λ: 500 nm, depth: 0 µm

(k) λ: 800 nm, depth: 0 µm

(l) λ: 1100 nm, depth: 0 µm

Figure 4.4: R of snow for decreasing snow depth, SZA: 40°, $\lambda = 500$ nm in the left panels, 800 in the middle, and 1100 nm i right panels. The snow pack consists of a one meter thick homogenous layer, with density 300 kgm^{-3} and snow grain radii 200µm.

4.1.2 ARF of sea ice

In Figure 4.5 we see how the angular reflectance distribution for sea ice, is affected when the incident irradiance beam is changed from $\theta_0 = 0°$ in the top panels, to 45° in the bottom. The wavelength of the light is 500 nm in the left panels, and 800 nm in the right panels. We notice the same nadir intensity peak as in Figure 4.1, decreasing symmetrically towards the horizon. The maximum deviation however is closer to unity for both wavelengths, and that the range is smaller, compared to that of snow. For SZA = 45° (bottom panels), we now observe a forward intensity peak at a polar angle of about 60° for both wavelengths, however, it is much more prevalent at 800 nm. This variability was not apparent for the same angular configuration for the ARF of snow. An explanation for this is the specular surface reflection from the Rayleigh scattered light at 500 nm, identified as an intensity ring around the horizon in the bottom left plot. At 800 nm there is less skylight and thus less reflection of the sky at the horizon.

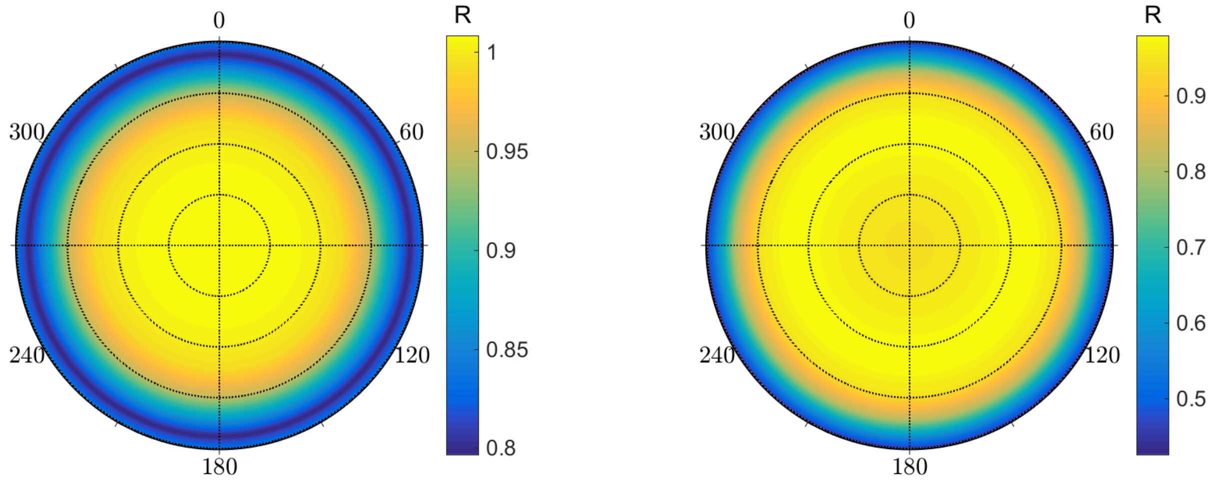

(a) λ: 500 nm, SZA: 0°

(b) λ: 800 nm, SZA: 0°

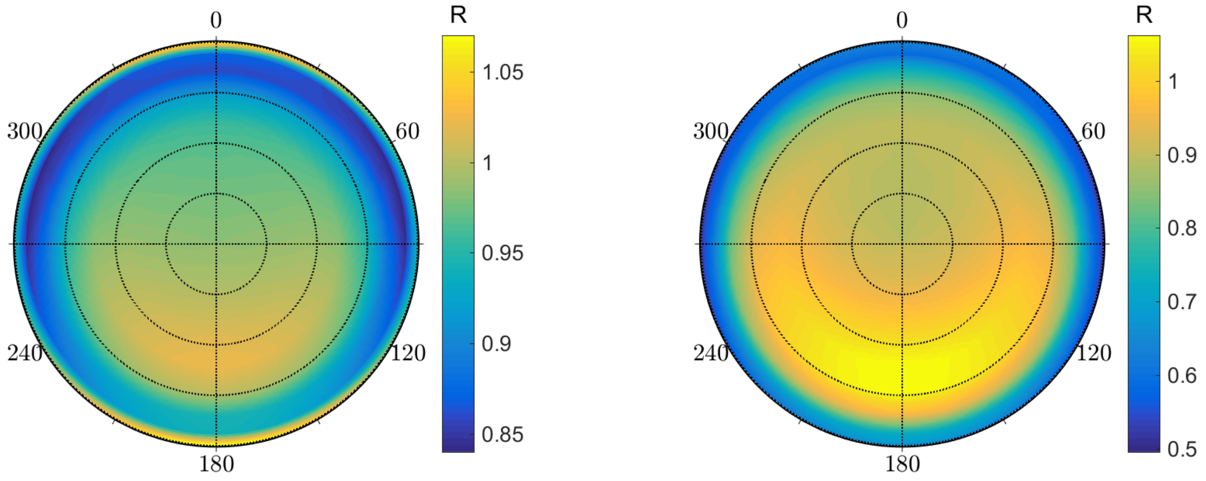

(c) λ: 500 nm, SZA: 45°

(d) λ: 800 nm, SZA: 45°

Figure 4.5: The anisotropic reflectance of a sea ice, with SZA 0° in the upper panels, and 45° in the lower. $\lambda = 500$ nm for left panels, and 800 nm for right panels. Sea ice parameters are shown in Table 4.1.

Varying zenith angle

When we examine the anistotropic reflectance factor of sea ice (Figure 4.6), with the same zenith angles and wavelength inputs as in Figure 4.2, we notice a variation in distribution as the zenith angle increases. For light at 500 nm wavelengths, the distinct forward peak that we saw for snow, is not prevalent for sea ice, and instead we see a peak value of the reflected light towards the horizon for, the value is increasing for increasing zenith angles, meaning more light is entering the sea ice from lower incident angles, resulting in the observed reflection intensities in horizontal observing angles. Moving towards the near infrared in Figure 2.7 we see that sea ice albedo is close to zero for wavelengths above around 950 nm, except for a small peak with a maximum of around 0.05 at 1100 nm.

In the middle and right panels of Figure 4.6 we see that the available light is mostly arising from forward atmospheric scattering, meaning we observe the same type of forward intensity peak that we had for snow, an effect that is also prominent for 1100 nm.

We note that the reflectance value for all observational angles at 1100 nm is below 1. This can be ascribed to the large upwards irradiance arising from the reflected incident irradiance beam, as the direct component is not represented in the upwelling radiance.

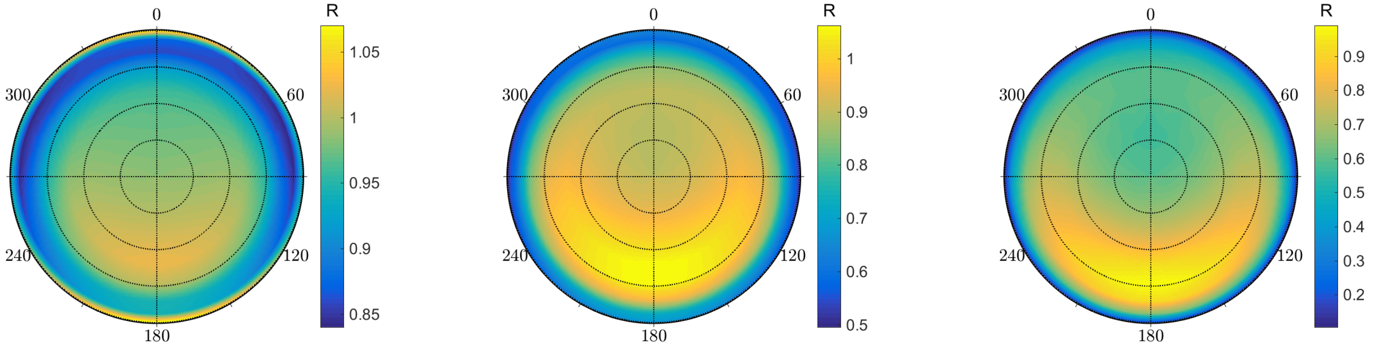

(a) λ: 500 nm, SZA: 45° (b) λ: 800 nm, SZA: 45° (c) λ: 1100 nm, SZA: 45°

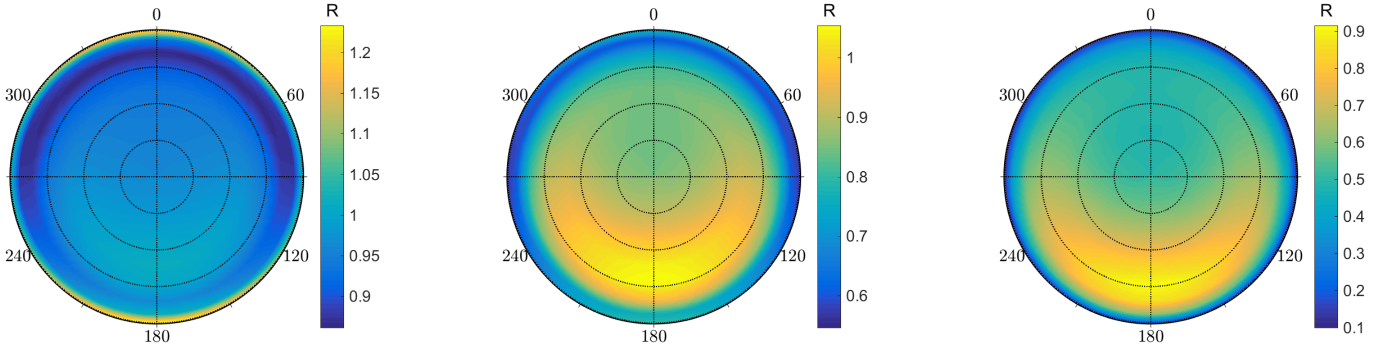

(d) λ: 500 nm, SZA: 55° (e) λ: 800 nm, SZA: 55° (f) λ: 1100 nm, SZA: 55°

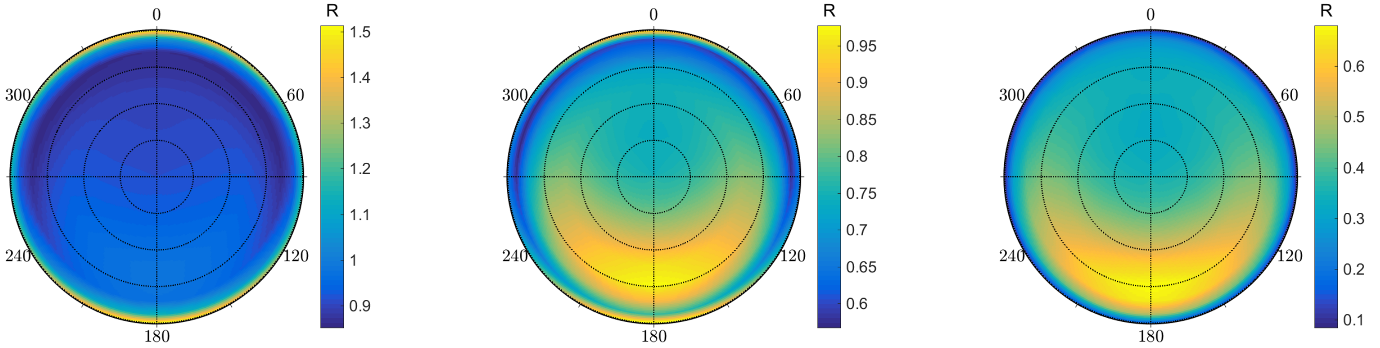

(g) λ: 500 nm, SZA: 65° (h) λ: 800 nm, SZA: 65° (i) λ: 1100 nm, SZA: 65°

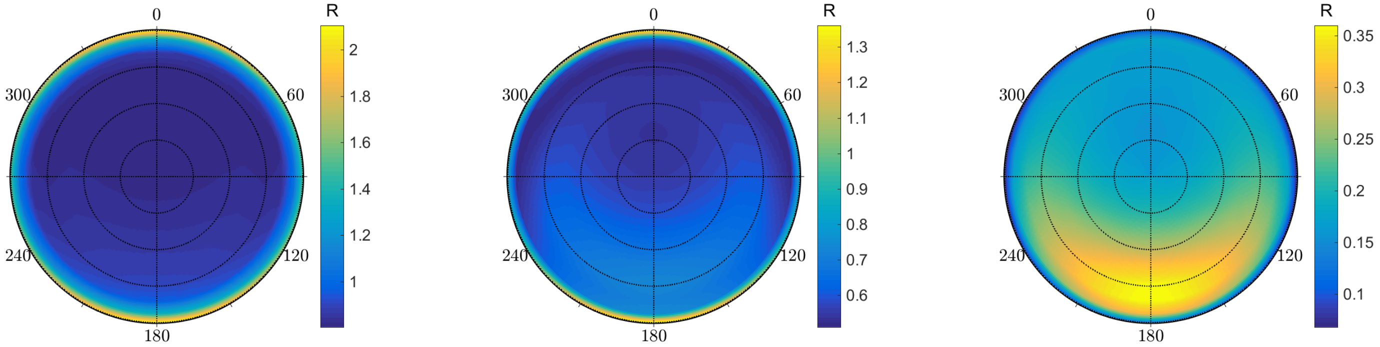

(j) λ: 500 nm, SZA: 75° (k) λ: 800 nm, SZA: 75° (l) λ: 1100 nm, SZA: 75°

Figure 4.6: The anisotropic reflectance of a sea ice, with solar zenith angle 45° in the upper panels, 55° in the second row, 65° in third row panels, and 75° in the lower panels. $\lambda = 500$ nm in the left panels, 800 nm in the middle panels, and 1100 nm in the right panels. Sea ice parameters are shown in Table 4.1.

Table 4.1: Model parameters for the one layered sea ice used in Figures 4.5 and 4.6.

Depth [cm] (from top)	Brine radii [μm]	Brine volume fraction	Bubble radius [μm]	Bubble volume fraction
0-100	500	0.05	50	0.01

4.2 Cloud effect

With their white-ish appearance, we know that clouds contribute to the spreading of light. As they contain droplet and/or crystals in the size range of microns, we also know that Mie scattering dominates, as opposed to the scattering on atmospheric gas particles, which is dominated by Rayleigh scattering. As Mie scattering is less wavelength dependent, we observe a more uniform scattering throughout the visible spectrum.

When considering what the satellites ”see”, we have to take their orbital altitude into account. As we have seen (Figure 2.2), there is some not negligible atmospheric attenuation happening. By converting this difference into a factor of reduction, we will get a correct value. The angular reflectance distribution does however not change, as radiance is a measure of flux independent of distance to the source (See Section 2.1.1).

As for clouds, it is a bit of a different story. We saw in Figures 4.7 and 4.9 that they account for some blocking, and only transmitting a thickness-dependent fraction of the incoming irradiance. The rest of the light is, by the laws of conservation, either absorbed or reflected. It becomes obvious that a thick cloud will block the reflected signal from the earth-atmosphere boundary. We will therefore look at the spectral albedo of clouds, to see what thicknesses allow for sufficiently transmittance of ground level reflectance.

First we examine how the presence of clouds affects the total incoming irradiance on ground level, shown in Figure 4.7. Cloud thickness is varied from 0 m (clear sky) to 5000 m (very thick cloud), with a mean droplet radii of 10 μm, and a volume fraction of 10^{-6}. The solar zenith angle is 45°. In the left panel we see the total incident irradiance for the different cloud profiles, and not surprisingly we observe decreasing irradiance for increasing cloud thickness. In the right panel the irradiance curves are normalized to that for zero clouds, and it becomes clear that significant attenuation occors throughout the spectrum, and especially for NIR wavelengths. A cloud of only 100 m vertical extension blocks almost half of the incoming irradiance at around 1250 nm, while a 500 m thick cloud blocks out 90% of the irradiance in the same interval. No irradiance is passed through for clouds thicker than 500 m beyond about 1350 nm.

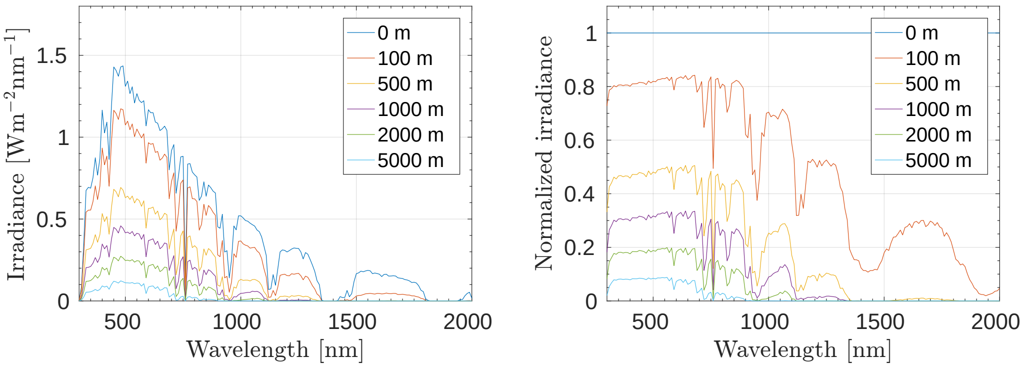

Figure 4.7: The impact of clouds on the incident spectral irradiance on ground level for various cloud thicknesesses. The left panel shows the total modelled irradiance, while the right panel shows the same irradiances normalized to that of no clouds. The ground is covered by 1.2 m thick snow, see Table 4.3, above 1.3 m thick sea ice. Solar zenith angle is 45°

The distinct dents in the normalized irradiance spectra in the right panel of Figure 4.7 corresponds to the atmospheric absorption bands in the irradiance spectra in the left panel of Figure 4.7 (and also in Figure 2.2). The enhanced scattering in the cloud environment increases the chance of photons getting absorbed by atmospheric constituents, in a rate related to the extra numbers of mean free paths caused by interaction with the (larger) cloud particles. The effect can however also arise from the near zero reference irradiance in these wavelength intervals, and does not necessarily imply a strong variability in the transmitted irradiance, especially in the IR parts of the spectrum.

When the cloud thickness is reduced something interesting happens: The incident irradiance for the thinnest clouds almost exceeds the irradiance of that of clear sky, at certain VIS- and NIR wavelength intervals, as shown in Figure 4.8. The exceeded intensity can be explained by a combination of only a little attenuation of the direct solar beam for the thin cloud, and an enhanced diffuse component arising from the additional mean free paths from scattering on a few cloud particles. The latter allows for more Rayleigh scattering, and a stronger downward radiative flux. As we move through the NIR and into the IR parts of the spectrum, we see the same attenuation trends as in Figure 4.7.

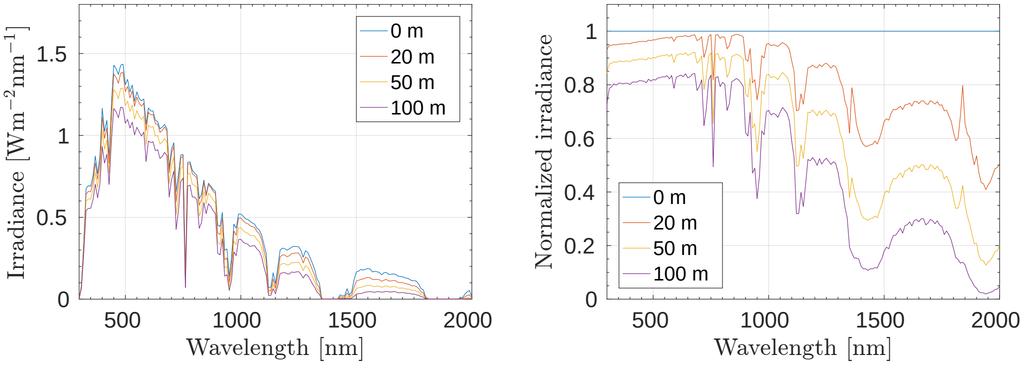

Figure 4.8: The impact of thinner clouds on downwelling irradiance. The left panel shows the total modelled irradiance for various cloud thicknesses, while the right panel shows the same irradiances normalized to that of no clouds. The ground is covered by 1.2 m thick snow, see Table 4.3, above 1.3 m thick sea ice. The solar zenith angle is 45°

In Figure 4.9 we see the extended spectrum for transmitted irradiance in a wider part of the spectrum, for a cloud of 100 m thickness, vs the irradiance with no clouds. We notice that the irradiance spectrum for the cloud scenario follows that of the clear sky, with an almost constant reduction of about 15% for shorter wavelengths. In the NIR part of the spectrum the blocking increases, and transmittance is reduced as we move further into the NIR and IR part of the spectrum. This indicates an established fact [e.g., Bohren and Clothiaux, 2006, Lamb and Verlinde, 2011] that even thin clouds contribute to the blocking of thermal radiation.

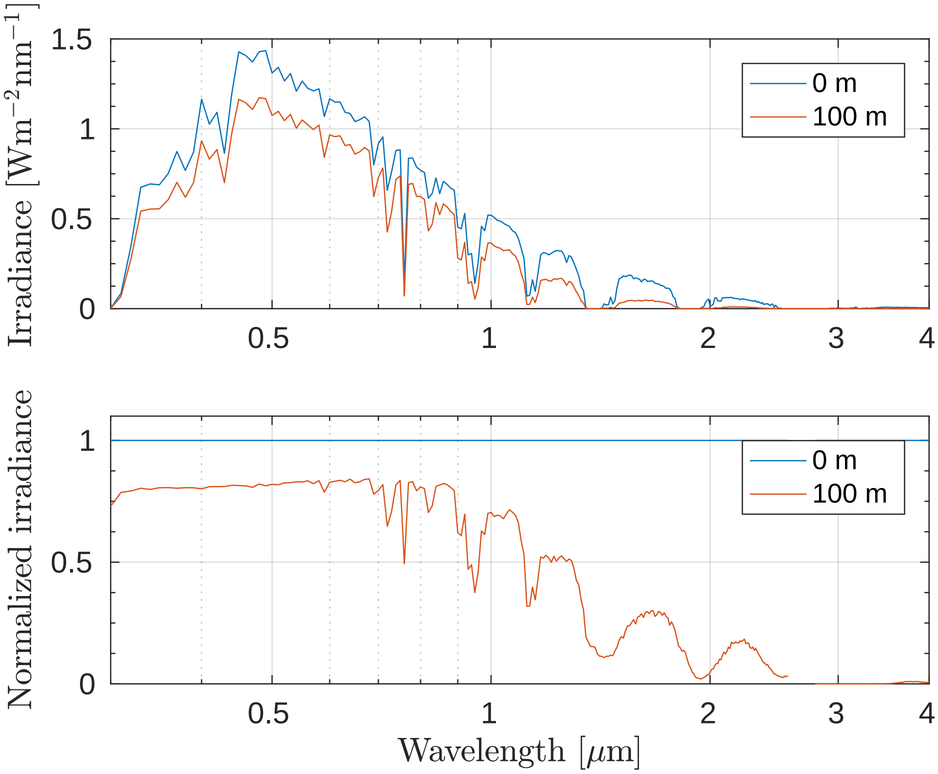

Figure 4.9: The transmitted irradiance on ground level. The blue line is the irradiance with no cloud, the red for a 100 m thick cloud. Top panel shows the total irradiance, while the lower panel shows the irradiance relative to the clear sky values.

4.2.1 Surface properties affecting the downward flux

As shown in Figures 4.7 - 4.9, the cloud attenuates significant amounts of the incoming solar radiation. It is also interesting to note that the surface albedo has an effect on the downward irradiance at ground level: In Figure 4.10 we see that a highly reflective surface results in a higher downward flux than that of a less reflective surface. This is an effect arising from the repeated backscattering between the ground and the sky, where more light is backcattered from a more reflective surface.

With the presence of clouds, here 500 m thick, the effect is even more significant. We see that downward irradiance $F_{\downarrow}$ over snow is about 3 times as high as for over open water. This artifact makes estimations of the surface albedo possible, while only measuring the downwelling irradiance.

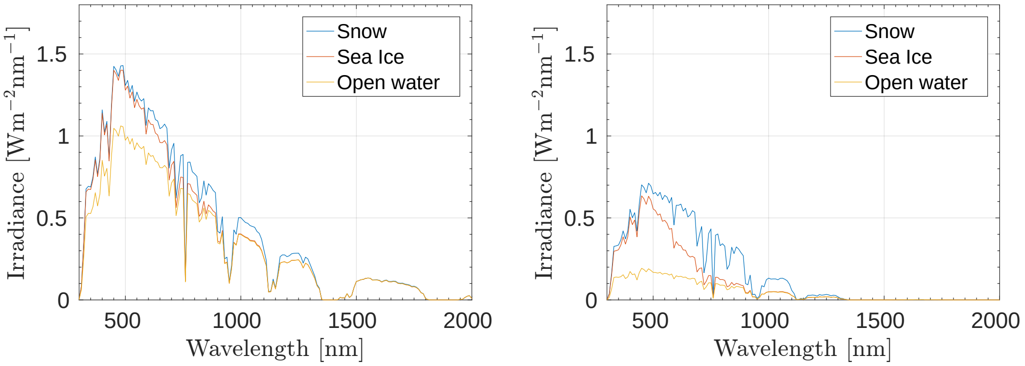

(a) 20 m thick cloud

(b) 500 m thick cloud

Figure 4.10: Surface albdo effect on downward irradiance, Solar zenith angle is 45°

4.2.2 Angular distribution and clouds

The results from Figures 4.7 and 4.8 tells us that the presence of even just thin clouds affects the atmospheric radiation situation dramatically. The effect of clouds on the angular distribution on snow is shown in Figure 4.11, for three different wavelengths (500, 800 and 1100 nm, left to right), $\theta_0 = 45°$. The top panels shows the anisotropic reflectance factor R for clear skies (as seen in the top panels in Figure 4.2). In the second row we see the effect of a 50 m thick cloud, where the forward intensity peak of R is shifted to the horizon for all wavelengths. This indicates an increase in the diffuse downwards irradiance component, while the reflectance distribution is still affected by the direct irradiance beam. The positive deviation from the average value is also changed: we see a slightly higher maximum value for both 500 and 800 nm, about 1.25 times the average value for 500 nm, and almost 1.4 for 800 nm. For clear sky the maximum intensity fr 500 nm is about 1.2, while for 800 nm it is around 1.3. The maximum value for 1100 nm is approximately the same for clear sky as with a 50 m thick cloud. In the third row panels of Figure 4.11, in the presence of a 100 m thick cloud, the distribution is smoothed out even more for all wavelengths, and the forward peak, whilst still being prominent, has seen a large intesity reduction. For 500 nm the maximum value is only 1.07 times the average value, for 800 nm it is about 1.15, and for 1100 nm it is about 1.2. For even thicker clouds, the trend of diffusing is even more pronounced. With a 300 m thick cloud, the angular distribution of light is almost totally diffused, and we notice a distinct "shallow bowl" shape, as described by Schaepman-Strub et al. [2006]. It is recognized by a slightly negative deviation symmetrically about nadir, with a slightly positive deviation towards the horizon. The overall distribution is however close to Lambertian, especially for 500 nm where the maximum deviation is about 0.5% from the average value. For 800 nm the maximum deviation is about 5%, while for 1100 nm it is as much as 10%. The snow configuration is the same as used previously: density 300 kgm^{-3} and radii 200 μm.

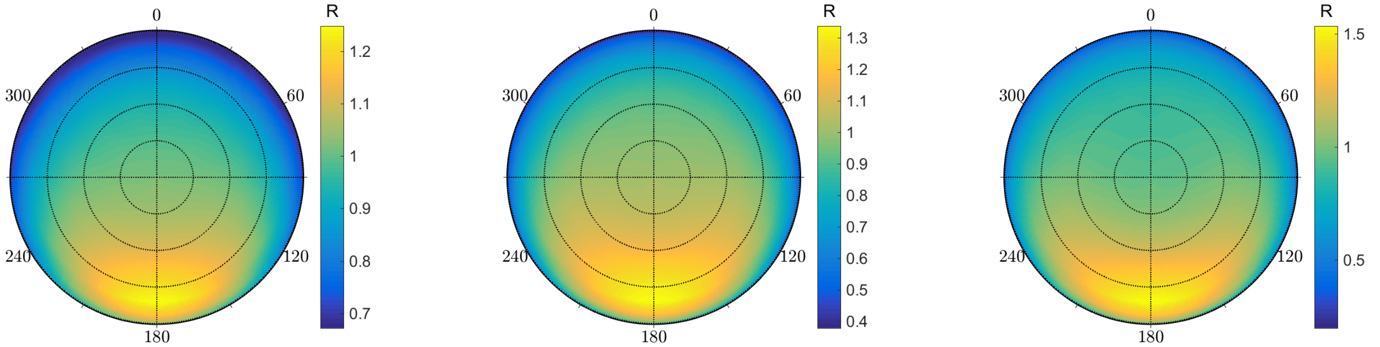

(a) λ: 500nm, Cloud thickness: 0 m

(b) λ: 800nm, Cloud thickness: 0 m

(c) λ: 1100nm, Cloud thickness: 0 m

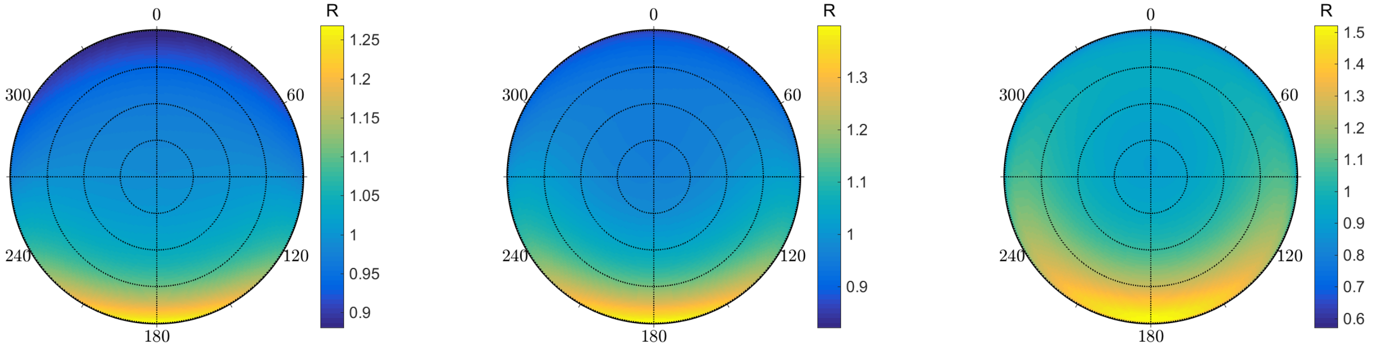

(d) λ: 500nm, Cloud thickness: 50 m

(e) λ: 800nm, Cloud thickness: 50 m

(f) λ: 1100nm, Cloud thickness: 50 m

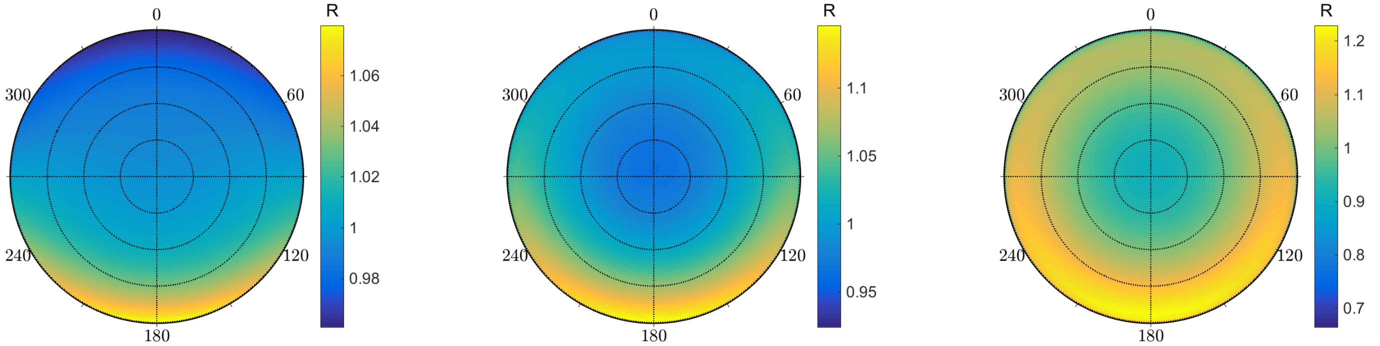

(g) λ: 500nm, Cloud thickness: 100 m

(h) λ: 800nm, Cloud thickness: 100 m

(i) λ: 1100nm, Cloud thickness: 100 m

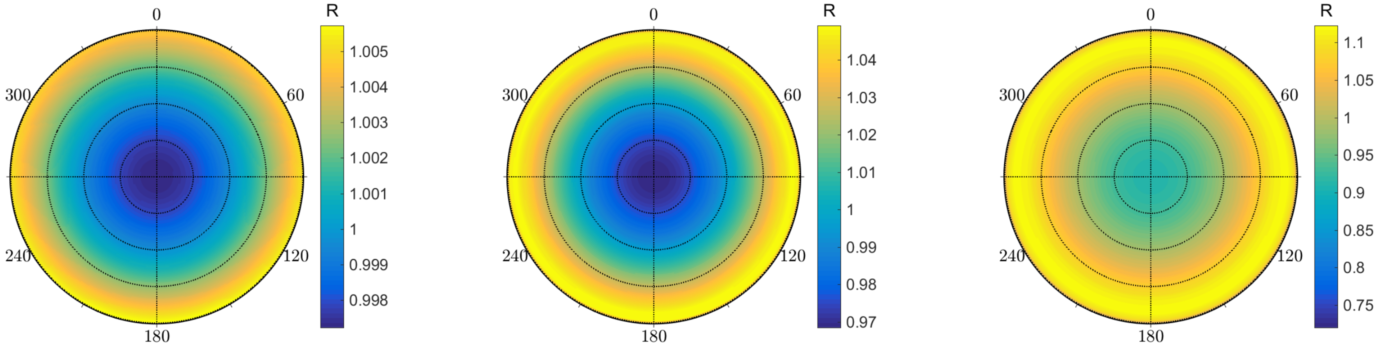

(j) λ: 500nm, Cloud thickness: 300 m

(k) λ: 800nm, Cloud thickness: 300 m

(l) λ: 1100nm, Cloud thickness: 300 m

Figure 4.11: ARF of snow for four different cloud thicknesses, with SZA 45°. The top panels are without clouds, then the thickness is incresed to 50 m in the second row panels, and 100 m in third row panels, and 300 m in the bottom panels. Wavelengths are 500 nm (left panels), 800 nm (middle column panels), and 1000 nm (right panels).

In Figure 4.12 we see clouds effect on snow ARF for solar zenith angle of 70°. Here the diffusing effect is even more pronounced than in Figure fig. 4.11. If we compare the second row panels in this figure, with those in the second row on the previous page, we see that the angular distributions are almost identical, even though the zenith angles are 30° apart, for a 50 m thick cloud. For 100 m, the panels are almost indistinguishable, which is rather impressive considering the downward flux is only reduced with about 20% (see Figure 4.7). For 300 m we can not tell them apart.

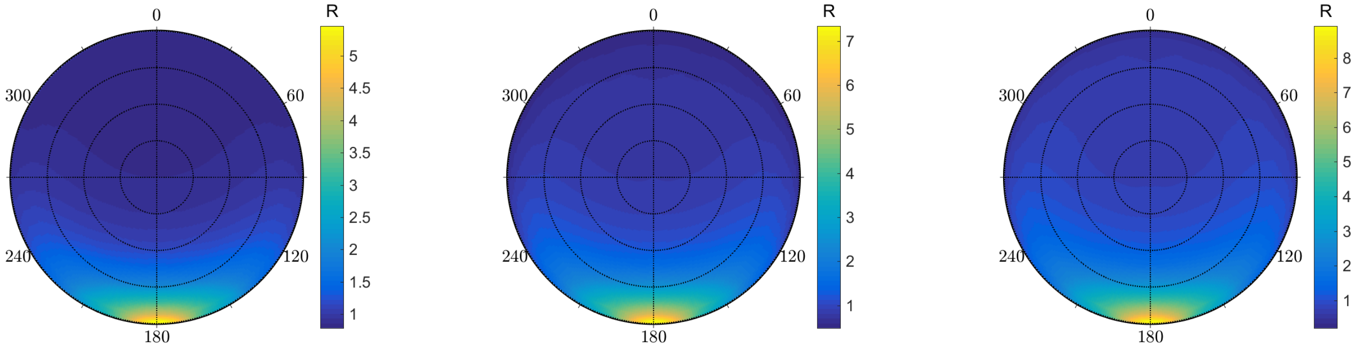

(a) λ: 500nm, Cloud thickness: 0 m (b) λ: 800nm, Cloud thickness: 0 m (c) λ: 1100nm, Cloud thickness: 0 m

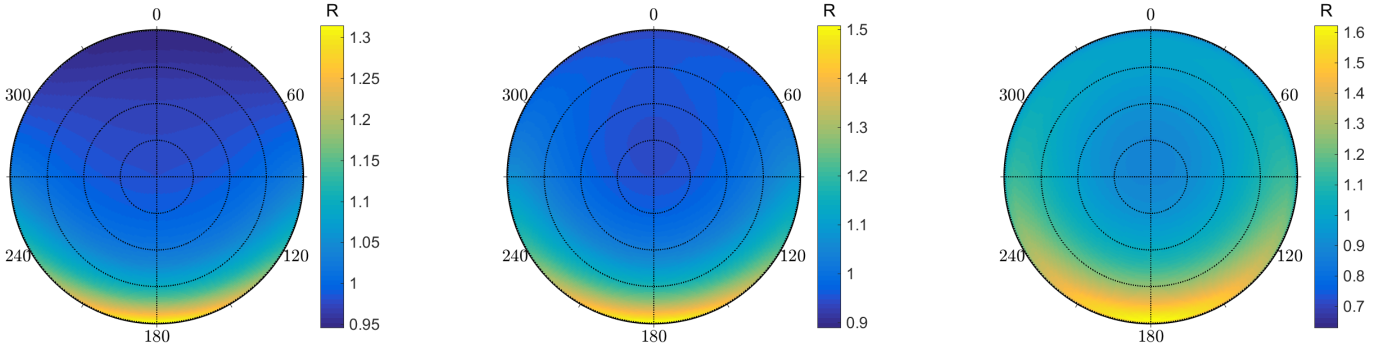

(d) λ: 500nm, Cloud thickness: 50 m (e) λ: 800nm, Cloud thickness: 50 m (f) λ: 1100nm, Cloud thickness: 50 m

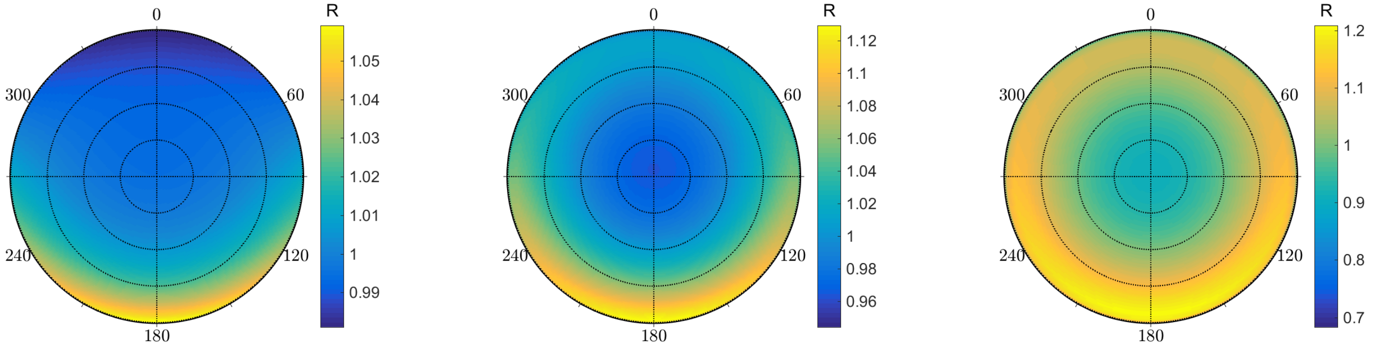

(g) λ: 500nm, Cloud thickness: 100 m (h) λ: 800nm, Cloud thickness: 100 m (i) λ: 1100nm, Cloud thickness: 100 m

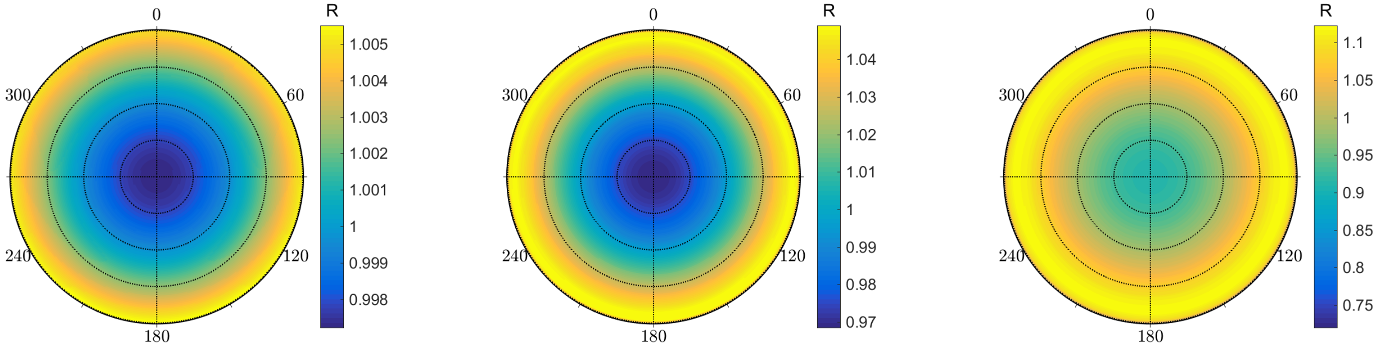

(j) λ: 500nm, Cloud thickness: 300 m (k) λ: 800nm, Cloud thickness: 300 m (l) λ: 1100nm, Cloud thickness: 300 m

Figure 4.12: ARF of snow for three cloud thicknesses, SZA 70°: 0 m (clear sky) in the top panels, 50 m in the middle row panels, and 100 m in the bottom panels. Wavelengths are 500 nm (left panels), 800 nm (middle column panels), and 1100 nm (right panels). The snow pack consists of a 1 m thick slab with grain radii 200 μm, with density 300 kgm^{-3}.

The presence of a thick cloud layer will inhibit the satellite monitoring ability, and adding a even thicker cloud would mean even less irradiance transmitted through the cloud on its way down, and even less transmitted back up to space. We will however look at the reflectance distribution of this kind of scenario as well, to check if an adequately thick cloud will give rise to completely Lambertian snow reflection. For all wavelengths we see no difference between the angular distribution when the cloud thickness is more than 300 m. This can be noted by comparing the bottom plots in Figures 4.11, 4.12 and 4.13.

For diffusing effect is strongest for shorter wavelengths, with a variation of only $+0.5$ and -0.2%. For 800 nm the deviation range is $+4$ and -3%, while for longer wavelength, the least diffusing effect is seen, with a variational range of about $\pm 10\%$.

4.3 Comparing with previous results

In Hudson et al. [2006], they investigate the BRDF and ARF of Antarctic snow through in-situ measurements, and with a plane-parallel radiative transfer model. They saw some variations in the snow ARF measurements for similar zenith angles at different days, with no noticeable change in the sastrugi. They propose variations in snow grain size as an explanation for the variations in R. Figure 14 in their paper shows the observed and modelled ARF for snow at 900 nm, with zenith angle $\theta_0 = 64.8°$, for snow grains of 100 μm radii. We have tried to recreate this scenario in Figure 4.14a, together with model runs with both smaller and larger snow grain radii.

The measured values of R from Hudson et al. [2006] (Section 4.3) showed some variability from different days at similar zenith angles, and they propose grain size variations as an explanation. As we have seen in Figure 4.3, our modelling of the ARF does only partly support this hypothesis, as the ARF seems to be independent of small variations in snow grain size.

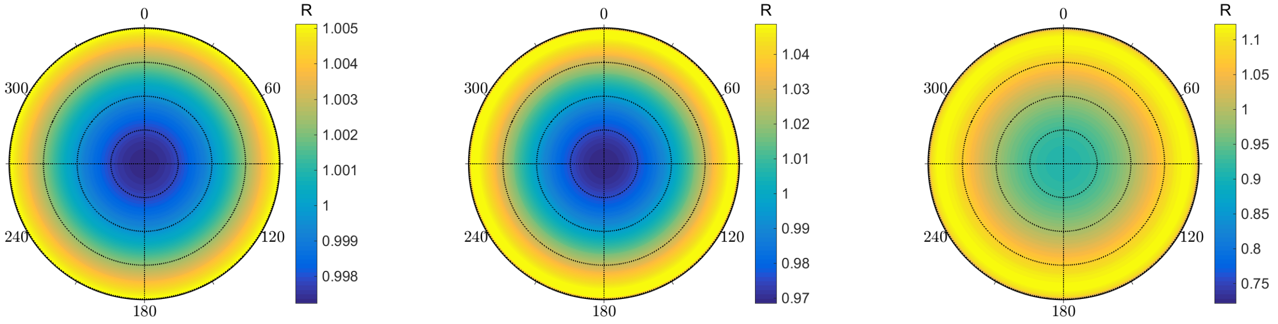

(a) λ: 500nm, Cloud thickness: 500 m

(b) λ: 800nm, Cloud thickness: 500 m

(c) λ: 1100nm, Cloud thickness: 500 m

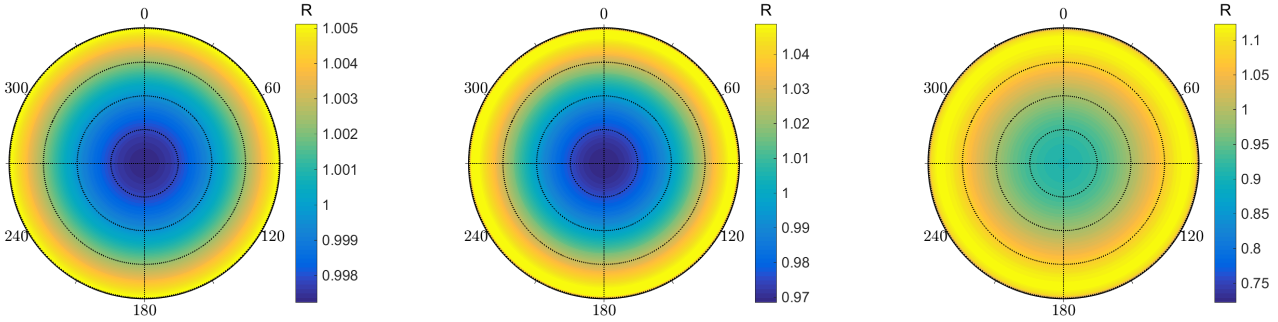

(d) λ: 500nm, Cloud thickness: 5 km

(e) λ: 800nm, Cloud thickness: 5 km

(f) λ: 1100nm, Cloud thickness: 5 km

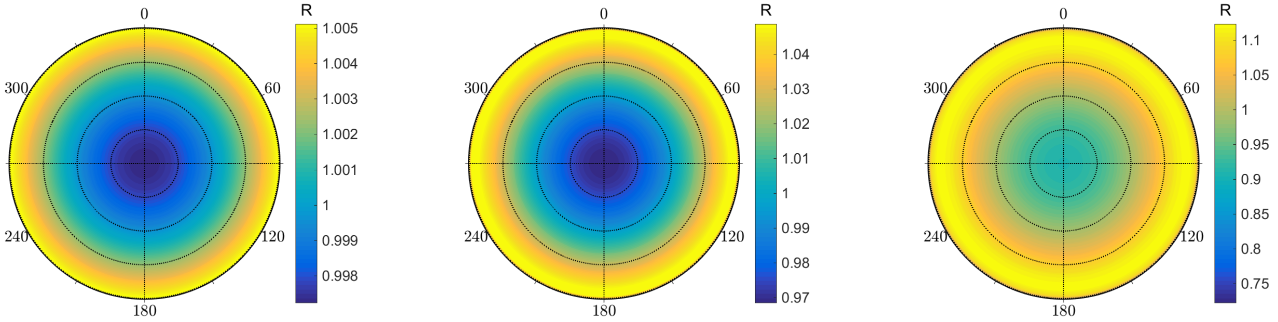

(g) λ: 500nm, Cloud thickness: 10 km

(h) λ: 800nm, Cloud thickness: 10 km

(i) λ: 1100nm, Cloud thickness: 10 km

Figure 4.13: ARF of snow for very thick clouds. The top panels shows the angular reflectance didistribution of snow with a cloud thickness of 500 m, the middle 1 km, while in the bottom panels shows the extreme scenario of a cloud of 10 km thickness. Wavelengths are 500 nm in the left panels, 800 in the middle, 1100 in the right. The snow pack consists of a 1 m thick slab with grain radii 200 μm, with density 300 kgm^{-3}.

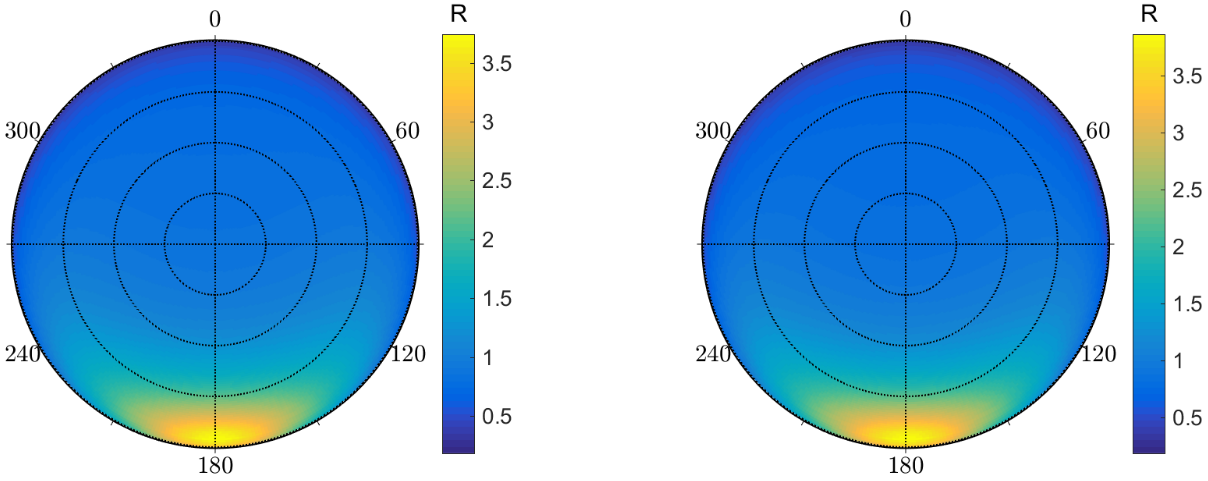

(a) 100 μm, as in Hudson et al. [2006]

(b) 50 μm

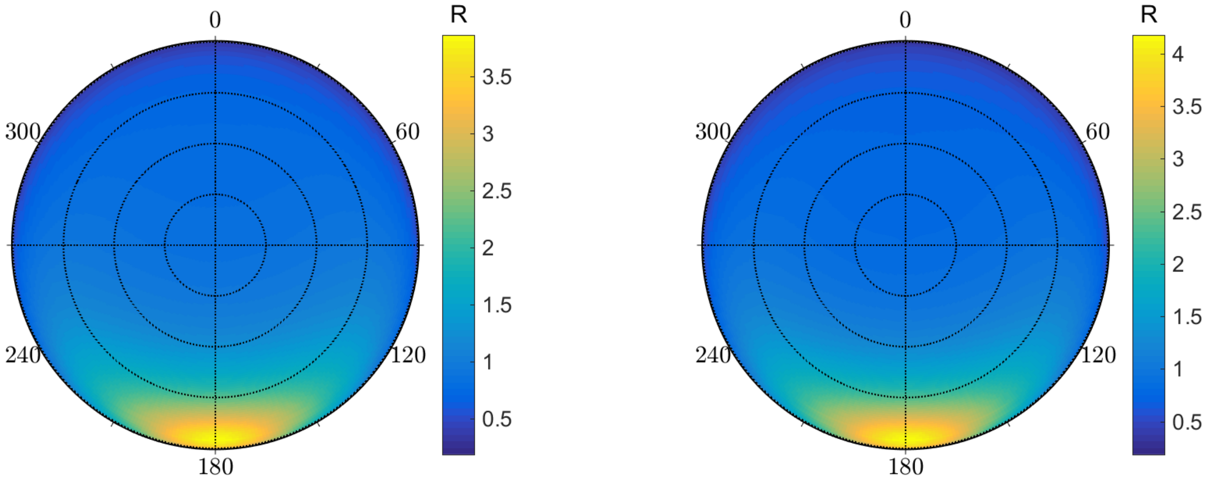

(c) 150 μm

(d) 300 μm

Figure 4.14: An approach to recreate Figure 14 in Hudson et al. [2006], which depicts the ARF of Antarctic snow, with θ_0= 64.8° at 900 nm. Snow parameters are shown in Table 4.2

Table 4.2: An approximation of the snow parameters to compare results with Figure 14 in Hudson et al. [2006]. θ_0= 64.8°, λ = 900 nm.

	Depth [m]	Snow grain radius [μm]	Density [kg/m^3]
Figure 4.14a	1.5	100	300
Figure 4.14b	1.5	50	300
Figure 4.14c	1.5	150	300
Figure 4.14d	1.5	300	300

4.4 Field work

4.4.1 Measured reflectance

With the setup described in Section 3.1.1, we collected radiance and irradiance data at three Svalbard glaciers: Austre Brøggerbreen, Kongsvegen and Tellbreen, sometimes referred to as day 1, day 2 and day 3 from here.

In Figure 4.15 we see the measured reflectance spectrum for wavelengths in the visible and near infrared parts of the spectrum (350-900 nm). The radiance sensor was facing the ground in a 45° angle, and pointed in the approximate solar azimuth angle. Each line in the plots represents a time series, collected at 15 seconds intervals. The time series in Panels a) and b) (about 50 minutes) were significantly longer than for that in Panel c), which was only 5 minutes. This is partly why the total amount of curves are enclosed within a smaller band of reflectance intervals in the Tellbreen-plot. The highest reflectance values were obtained at Tellbreen (Panel c), where we also can observe an almost constant reflectance of 0.9 from 600 to 900 nm. For day 1 and 2 there was a decreasing trend in this wavelength range, more pronounced on day 1 than 2. An explanation for this can be the surrounding topography, which were mountainsides covered in snow. This might have enhanced the diffuse component, from backscattering from the surrounding snow covered ridges. This phenomenon can also be supported by the results showed in Figure 4.10, where more reflective surfaces contribute to a higher total downwelling irradiance. The variance in reflectance spectra can however also be ascribed to sensor calibration errors, as this variability is within the accuracy range of the radiometers (Table 3.1).

While our setup did not allow for measuring upwards irradiance, we have plotted the reflected radiance $L_{\uparrow}$ (at 45°) divided by the incoming irradiance $F_{\downarrow}$, multiplied by π to make it dimensionless. It is a modification of the ARF (Equation 2.18), where we use the the downwelling irradiance as opposed to the upwelling. A consequence of this is that we don't know the value of R really is, but we can try to make sense of the behaviour of the reflected light for various wavelengths, and with a various cloud cover.

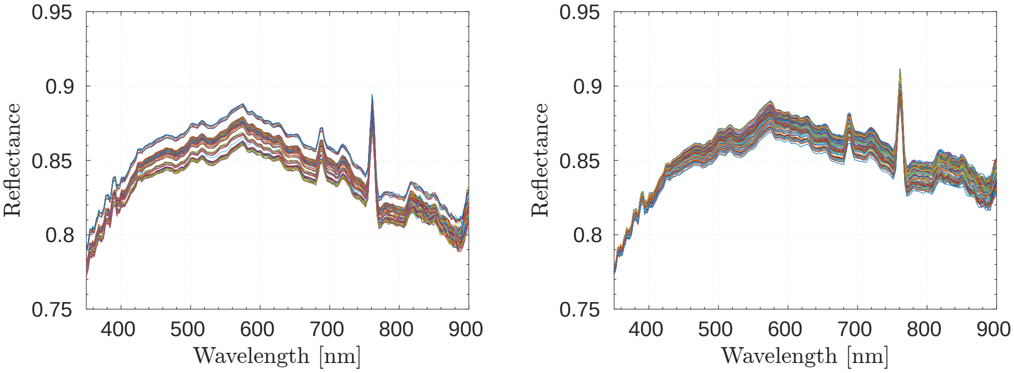

(a) Day 1. Low, dense clouds.

(b) Day 2. High, thin clouds.

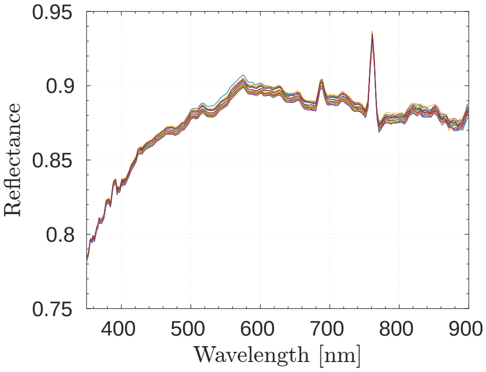

(c) Day 3. High thin clouds, and pronounced surrounding topography

Figure 4.15: The measured spectral reflectance at a) Austre Brøggerbreen, April 9th 2016, b) Kongsvegen, April 13th 2016, and c) Tellbreen, April 16th 2016. Cloud conditions are listed under each panel.

As mentioned the albedo of snow is almost constant for the short wave radiation between 350 and 600 nm, while in these plots the reflectance increase from around 0.8 at 350 nm, to 0.87-0.9 at 600 nm. This indicates that there might be some angular dependency for the snow reflectance at shorter wavelengths, as we would expect an corresponding value for all wavelengths for a diffusely reflecting surface. For zenith angles between 65 and 75° (Figure 4.2), there is a strong forwards peak towards the horizon, leaving assessing of small variation in R for smaller θ difficult. This is discussed further in Section 4.4.2 below.

At all three sampling times, the solar zenith angle was around 70° during measurements.

Other conditions also affect the local variations in the reflectance. During all days of field work we experienced a continuous change in cloud cover, with high, thin clouds in the last two series, and a denser, lower cloud cover in the first. (Revisit Section 3.1.3 for description of the weather conditions). In Figure 4.16 we have isolated the first, last and middle time series, to investigate if the changing zenith angle is affecting the value. The spectra from both day 1 and 2 shows that the middle time series had the highest value throughout the spectrum, and the last had the lowest. The variation is at the most around 4% for both days. For day 3, we see very little variation in the various time series, due to the short collection time, but we notice that the middle time series had the lowest reflectance value, and the last the lowest.

This is not transmissible to the trend of increased snow albedo for increased zenith angles, as the sun moved closer to the horizon for all measurement series. The change in solar zenith angle can therefore not be said to be the main contributor for the reflectance variations, as we then might expect the first time series to have the lowest reflectance, an d the last the highest.

In Figure 4.17 we see the variation in reflectance for the three days of field work, with three isolated wavelengths throughout the measurement series. As noted in Figure 4.15, the reflectance is lowest for short wavelengths for all three days. In day 1 and 2, light at mid-wavelengths (500 nm) had the highest reflectivity, while for 900 nm it has decreased. For day 3 the reflectance at 500 and 900 nm is almost equally high, at about 0.88 throughout. We see about the same reflectance value for 350 nm light for all three days, suggesting that light in this wavelength range is less sensitive to variations in topography and

At around 14:40 on day 1, we see a short interval of increased reflectance, lasting about two minutes. As seen in Section 2.3.3, clouds have no effect on the albedo for these wavelengths, but from Section 4.2, we have seen that the angular reflectance distribution gets more isotropic in the presence of clouds. A local increasement in cloud thickness might therefore explain this small "jump". For day 2 we see some variations in the 500 nm reflectivity curve, which is not present in the 300 and 900 nm curves, mainly at around 14:25 and 14:40. This can be explained by

From both day 1 and 2 it appears that light of longer wavelengths are more sensitive to small changes in cloud cover than shorter wavelengths, where

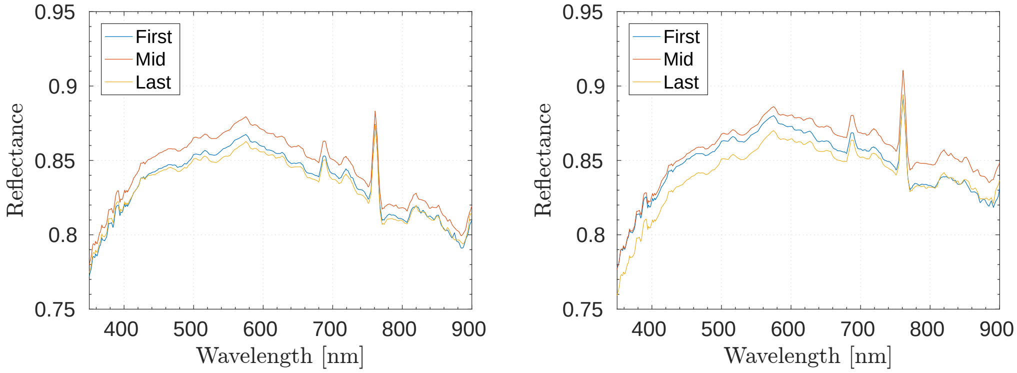

(a) Day 1. Low, dense clouds.
SZA: start: 68.8, end: 71.6

(b) Day 2. High, thin clouds.
SZA: start: 69.8, end: 71.6

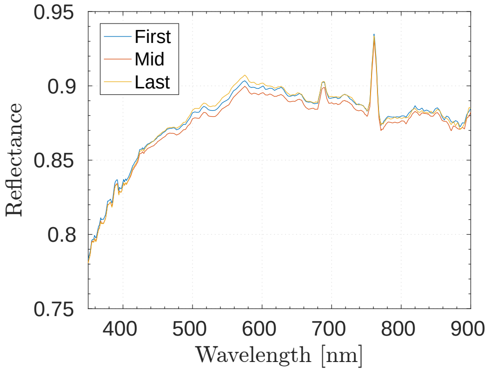

(c) Day 3. High thin clouds, and pronounced surrounding topography
SZA: start: 68.7, end: 68.8

Figure 4.16: The measured spectral reflectance for three selected time series: first (blue), middle (red), and last (yellow), at a) Austre Brøggerbreen, April 9th 2016, b) Kongsvegen, April 13th 2016, and c) Tellbreen, April 16th 2016. Cloud cover information and solar zenith angle is listed under each panel, more details can be found in Table 3.2.

the 900 nm curves exhibit a rather pronounced jaggedness, which fits well with the modelled result of R for various cloud thicknesses, seen in Figures 4.11 and 4.12. The trend is also visible for day 3, but due to the short measurement series it is less pronounced in the plot. Even though the cloud cover was remarkably different in day 1 and day 2, the reflectance curves of light with wavelengths 350 and 500 nm are very similar for the two days, while it is higher for that of 900 nm on day 2.

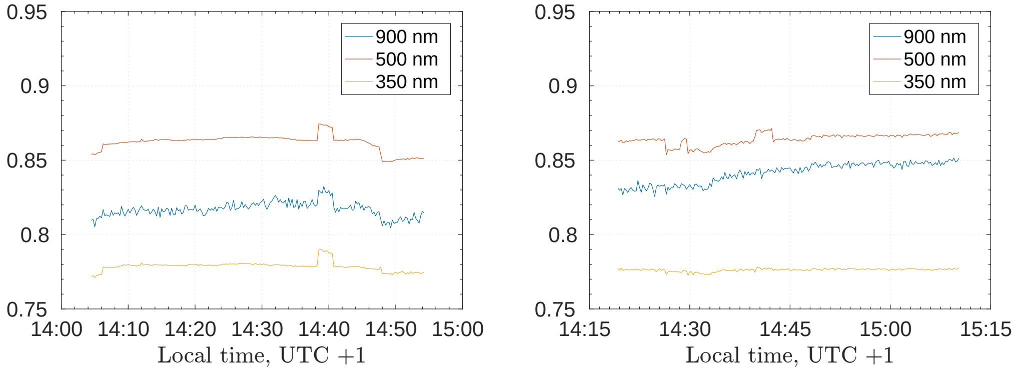

(a) Day 1. Low, dense clouds.

(b) Day 2. High, thin clouds.

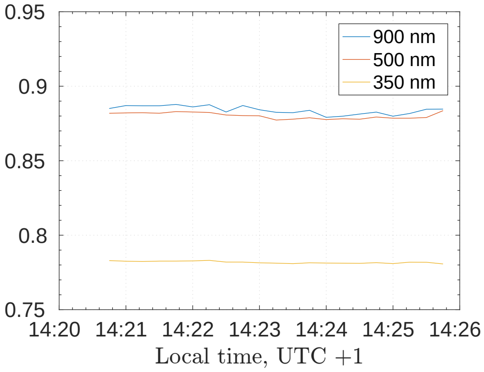

(c) Day 3. High thin clouds, and
pronounced surrounding topography

Figure 4.17: The measured spectral reflectance for three selected wavelengths: 900 nm (blue), 500 nm (red), and 350 nm (yellow), at a) Austre Brøggerbreen, April 9th 2016, b) Kongsvegen, April 13th 2016, and c) Tellbreen, April 16th 2016. Cloud cover information is listed under each panel, more details can be found in Table 3.2.

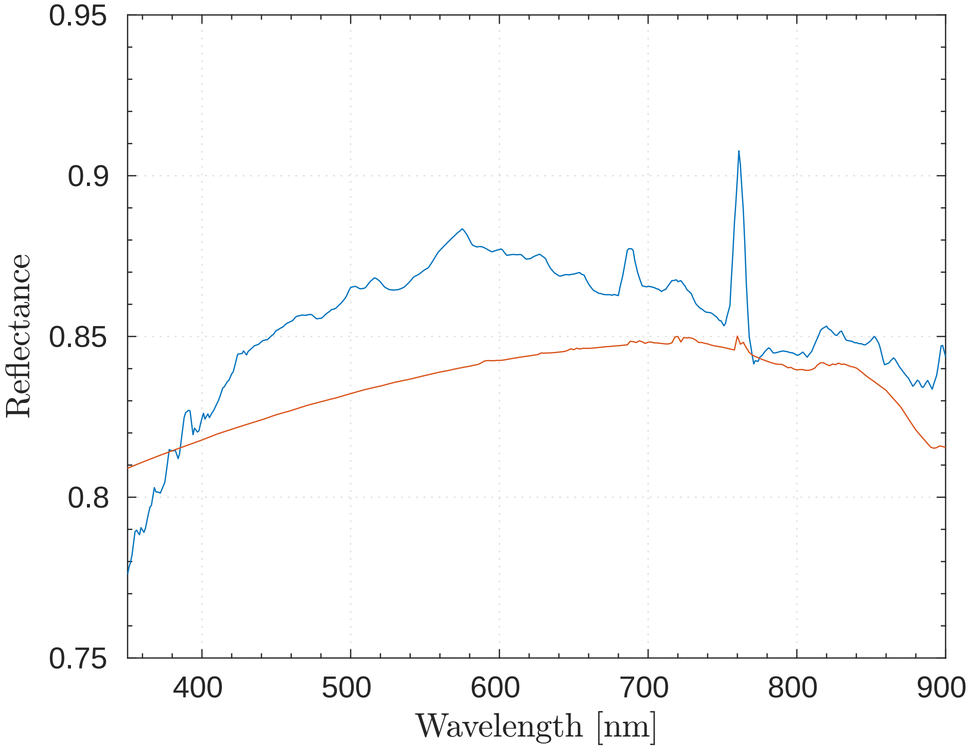

Figure 4.18: Spectral reflectance from Kongsvegen April 13th. The blue represents one time series of reflectance data, while the red line represents modelled reflectance, with a two layered snow cover of 1.2 m thickness, and an observing polar angle of 45°, in correspondence with the radiometer setup in the field.

Table 4.3: An approximation to the parameters for the snow pack at Kongsvegen April 14th 2016.

	Depth [cm] (from top)	Density [kg/m^3]	Snow grain radius [µm]
Layer 1	0-20	145	75
Layer 2	21-100	240	1000

Addressing the sharp peaks that occurs in the measured reflectance plots in Figures 4.15 and 4.16: One very large peak is located at around $\sim$ 760 nm, while two less prominent ones at 680 and 720 nm. These wavelengths correspond to those of the dents in the solar spectrum in Figure 2.2, which can be explained by the strong molecular absorption exhibited by O_2 in this wavelength region [Hill and Jones, 2000]. While the two sensors detect this dent individually, their spectral uncertainty range have most likely lead to a detection of slightly different corresponding wavelengths, resulting in a constructive interference effect when we take the ratios between the fluxes. A perfect overlap of the absorption bands would yield a ratio that would cancel out the appearance of these peaks.

4.4.2 ARF for field measurements

When we have approximated the snow pack parameters for our collected data (Table 4.3), use our knowledge of the weather conditions to make an estimation of the angular reflectance at Kongsvegen on April 14th, shown in Figure 4.19. The solar zenith angle was $\sim 71.26°$, and we noted that roughly 5/8 of the sky was covered by thin, high clouds.

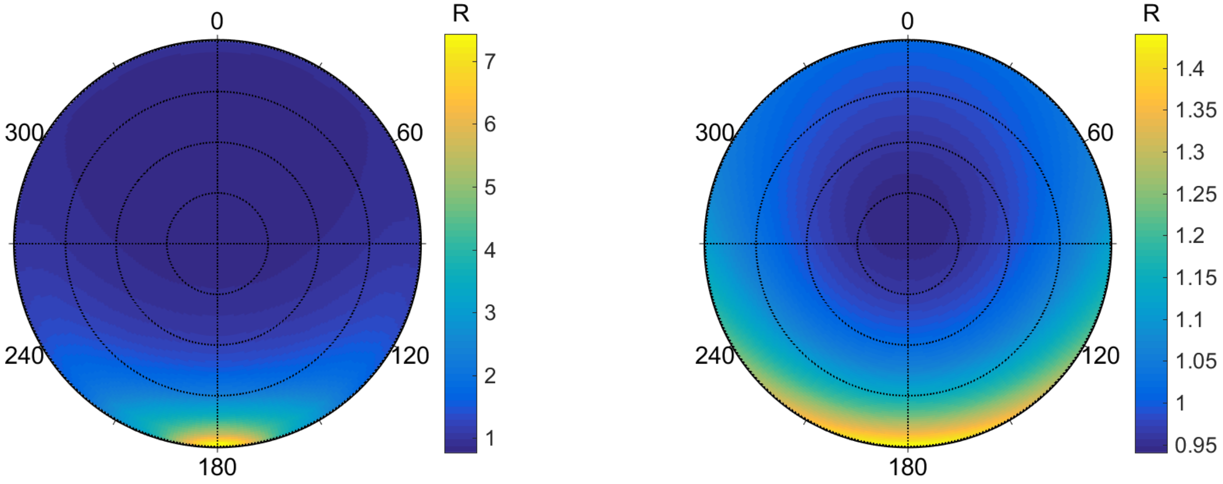

Figure 4.19: The anisotropic reflectance of a snow pack with model inputs corresponding to the parameters on Kongsvegen April 14th at 14:19 local time (Table 4.3), solar zenith angle is set to 71.26°, $\lambda = 500$ nm. Left panel is without clouds, right panel with a thin cloud cover of 50 m.

4.4.3 Estimating angle of incident light

When we have data from both a cosine and a scalar irradiance collector, we can take the ratio between them to estimate the average angle for the incoming light. Both sensor measure the total incoming irradiance, but their different shapes yields different signal processing: As we have seen in Chapter 3, the cosine response sensor weighs the incoming irradiance by the cosine of the angle of the incident light.

$$\frac{F_{\cos}}{F_{scalar}} = \frac{\int L\, u\, d\omega}{\int L d\omega} = \bar{u}, \tag{4.1}$$

where $F_{\cos}$ is the irradiance measured by the cosine response sensor, F_{scalar} by the scalar sensor (revisit Table 3.1 for specifications), and u is $\cos\theta$, the cosine response from the incoming irradiance.

When the sky is clear, there will be a large component of direct sunlight, as well as some diffuse components from atmospheric Rayleigh scattering. As we have seen, less light will reach the ground in the presence of clouds, and what reaches the ground has been diffusely scattered by the cloud constituents. By isolating the cosine response and solving Equation 4.1 for the average angle, $\bar{\theta}$ we get:

$$\bar{\theta} = \arccos \bar{u}, \tag{4.2}$$

an expression for the estimated average angle of the incident light. For diffuse light in the upward hemisphere, the mean angle of incidence is equal to the sum of the maximum and the minimum zenith angle, divided by two: $\frac{0° + 90°}{2} = 45°$. This means that angles closer to 45° indicates a larger diffusing component (when the actual solar zenith angle is known, and different from this angle).

The estimations for three different time series are shown in Figure 4.20. The cloud cover was remarkably different for the three sampling days, with low, thick clouds in Figure 4.20a, high, thin clouds in Figure 4.20b, and a few high clouds in Figure 4.20c. More details about the sampling conditions is available in Table 3.2. We note that in Figure 4.20a there are some large fluctuations in the average angle of the incoming light, indicating large variations in the cloud cover. This fits well with our cloud observations this day. The average angle of the incident light is also deviating by about 10° from the solar zenith angle on day 1. For days 2 and 3 there is only one degree deviation from the solar zenith angle, in correlation with the presence of only thin, high clouds these days. Some uncertainties are however also arising from the levelling of the radiometer setup.

We also note that the average zenith angle of incident light reaches a minimum at around 14:40, which corresponds to the effect we saw in Figure 4.17a, where there is an increase in in the angular reflectance.

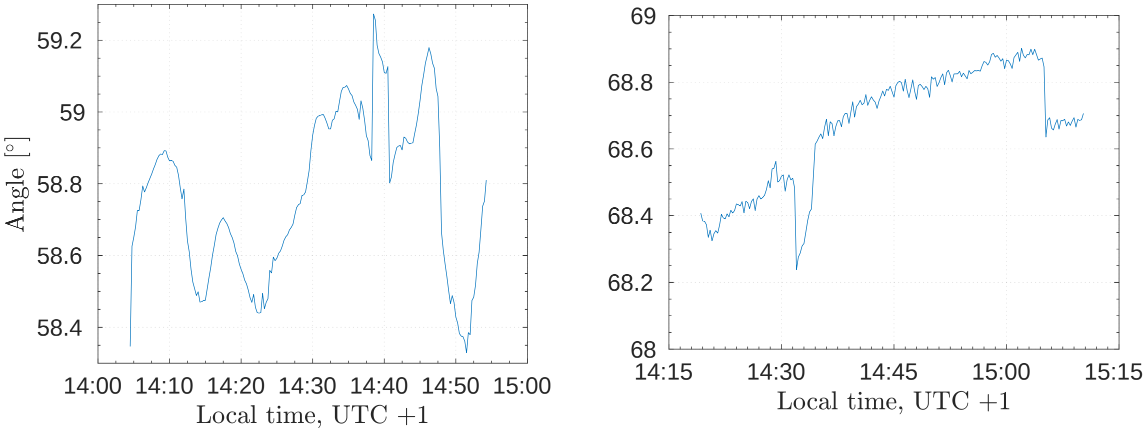

(a) Day 1. SZA: start: 68.8, end: 69.6

(b) Day 2. SZA: start: 69.8, end: 71.6

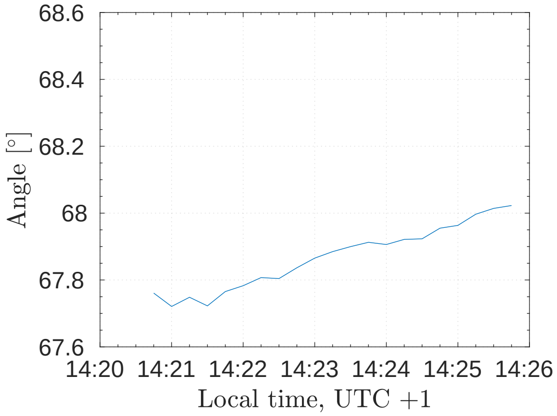

(c) Day 3. SZA: start: 68.7, end: 68.8

Figure 4.20: The estimated average angle of the incident light, for three sampling locations on Svalbard in April 2016: a) Austre Brøggerbreen, April 9th, b) Kongsvegen, April 13th, and c) Tellbreen, April 16th. The angles are estimated by applying Equations 4.1 and 4.2. Solar zenith angles for the individual time series are noted under each panel.

Chapter 5

Conclusions and outlook

Studying the nature of light is a complex and difficult task. When we want to include real life parameters, more possible complications arise. Many aspects needs consideration, and unsuspected effects might appear. Using a multi-stream model for solving the radiative transfer equation is a very effective and fruitful way to explore optical properties of various media

Collecting and assessing radiation data, as well as modelling various scenarios for a number of different parameter setups are all time consuming tasks. We need to weigh the importance of each parameter of interest, and take the time to evaluate their significance both as input and output weights.

ARF

Our results regarding the anisotropic reflectance factor of snow, is in accordance with previous results from Hudson et al. [2006], who found that the BRDF of snow is nearly constant for shorter wavelengths.

The ARF of snow is dependent on incident solar zenith angles for all three wavelengths (500, 800 and 1100 nm). The largest deviation from Lambertian reflection is seen for extreme observational angles (towards the horizon), for all three wavelengths. The effect is more prominent for longer wavelengths, where diffuse scattering from atmospheric constituents is reduced.

Light of shorter wavelengths (here 500 nm) exhibit less deviation from isotropic scattering on snow, than longer, while there still is a large deviation towards horizontal observational angles. For large solar zenith angles we observe a sharp intensity peak in the forward direction for a tiny angular interval at grazing angles.

It seems that for observing angles between $0 \leq \theta \leq 40$ at longer wavelengths, will give the most "correct" value for the reflectance value of snow, with R being close to unity in this interval.

When we observe the figures depicting the directional radiance dependency, the intensity peak in the horizontal direction (observing polar angles approaching 90°) can be explained by the principles of Mie-scattering for the first scattering event in the atmosphere/snow interface.

For very thin snow atop sea ice, we observe two intensity peaks: one arising from the snow backscattering, and one arising from sea ice backscattering.

We can conclude that for low solar zenith angles, the reflected light in observing angles from snow covered surfaces has a ARF close to 1, meaning that the weighing of

The ARF of snow seems to be independent of snow grain size for wavelengths in the visible part of the spectrum, for both large and small zenith angles. For NIR wavelengths, there is an increased forward peak intensity, limited to a slightly smaller observing solid angle, for larger snow grains. The average value of the ARF is however approximately unchanged for solid angles of π sr centered around nadir for various snow grain sizes.

Sea ice ARF exhibits large wavelength dependency, where for shorter wavelengths Rayleigh scattered light from the atmosphere results in reflectance intensity in horizontal directions. Deviation is negative in the upwards direction for larger zenith angles at all wavelengths.

Cloud effect

The reflectance of both snow and sea ice is diffused further with the presence of clouds. Our modelling suggests that even a thin cloud cover enhances the diffuse scattering from snow surfaces, a cloud of thickness of more than 200 m will result in a close to perfectly diffuse reflectance pattern.

The reflectance distribution of light of 500 nm wavelength is highly affected by the presence of clouds. The overall trend is that the range about uniform reflection is reduced with increased cloud over thickness, contributing to a more diffuse light scenario.

The angular distribution of light of longer wavelengths seems however to be more sensitive to small variations in cloud cover. The sensitivity seems to increase with increasing zenith angles.

As the clouds thickness increases, the variation in the angular reflectance patterns decrease for all zenith angles, until we reach a threshold at about 200 m. Adding to the cloud thickness beyond this threshold gives a unchanged angular reflectance distribution, independent of the solar zenith angle.

5.0.4 Comparing with previous results

The measured values of R from Hudson et al. [2006] (Section 4.3) showed some variability from different days at similar zenith angles, and they propose grain size variations as an explanation. As we have seen in Figure 4.3, and also in Figure 4.14, our modelling of the ARF only partly support this hypothesis, as the change in snow grain radii would have to be at least 0.5 to 1.5 times larger for an effect to be prominent. Other possible explanations for their observed variability in the ARF are in-situ and instrument uncertainties.

Field work

It seems that surrounding snow-covered topography might have an enhancing effect on measured total downwards irradiance, but this can also be ascribed to sensor uncertainties.

Being located in close vicinity to Longyearbyen, Tellbreen is easily accessible for locals, and is frequently traversed by snow mobiles, and is also a popular site for e.g. leisure activities and scientific research. In contrast we have the more remote Ny-Ålseund glaciers, mostly accessed only by scientists throughout the year. We could however not detect significant variations in our data sets.

The presence of clouds will effectively diffuse the light, and a thicker cloud layer will shift the cosine response towards the average of the polar angle (45°).

5.1 Further work

A further investigation on the ARF of snow which depth is approaching zero is of great interest, as this can tell us more about the reflective properties of sea ice, when only a thin, frizzy layer of small ice particles is covering the ice. We think this knowledge might be useful as an approximation to sea ice surface roughness.

Some central parameters that is known to have an impact on snow and ice albedo has been left out of this work, including black carbon constituents, algae growth, and aerosol variations.

Black carbon in snow is of rising interest, as it has become evident it is a contributor to climate change [e.g. Hansen and Nazarenko, 2004, Bond et al., 2013]. Both Hadley and Kirchstetter [2012] and Warren [2013] find that the presence of black carbon in snow decreases its albedo, and that the effect is amplified by increased snow grain size, which is connected to the established decreasing albedo for ageing snow. Difficulties in distinguishing between the presence of soot in the atmosphere and in the snow cover in satellite measurements [Warren, 2013] indicates that the impact black carbon constituents might have on snow and ice reflectivity is of high interest.

Suggestions for further work include: limiting the range of observational angle to a more narrow cone. This will in the cases of extreme value maxima close to the horizon give a more nuanced overview of the angular distribution, outside the extreme regions. This is especially relevant for incident irradiance zenith angles larger than about 60° on snow covered surfaces.

Being a very useful tool for looking at various scenarios of various, simplified parametrizations, our model is still a one dimensional multistream application for solving the radiative transfer equation. With a three dimensional radiative transfer model, we would have the chance to investigate the response to a greater extent, and also vary the input parameters in a more dynamic way, with extensive variations in both surface and atmosphere properties, like a fractionated cloud cover, or surface irregularities.

A model which allows for direct inputs of volume to surface (V/S) ratios of various parameters seems to be a step in the right direction, when advancing radiative transfer models, making them both more user friendly, and possibly more liable. For this, knowledge of the V/S of crystals in particular are crucial, as pointed out by Grenfell et al. [2005].

Bibliography

Craig F Bohren and Eugene E Clothiaux. *Fundamentals of atmospheric radiation: an introduction with 400 problems*. John Wiley & Sons, 2006.

Tami C Bond, Sarah J Doherty, DW Fahey, PM Forster, T Berntsen, BJ DeAngelo, MG Flanner, S Ghan, Bernd Kärcher, Dorothy Koch, et al. Bounding the role of black carbon in the climate system: A scientific assessment. *Journal of Geophysical Research: Atmospheres*, 118(11):5380–5552, 2013.

SC Colbeck. The layered character of snow covers. *Reviews of Geophysics*, 29 (1):81–96, 1991.

Marie Dumont, Olivier Brissaud, Ghislain Picard, Bernard Schmitt, J-C Gallet, and Yves Arnaud. High-accuracy measurements of snow bidirectional reflectance distribution function at visible and nir wavelengths–comparison with modelling results. *Atmospheric Chemistry and Physics*, 10(5):2507–2520, 2010.

inc. Encyclopædia Britannica. anisotropy, 2006. URL `https://global.britannica.com/science/anisotropy`.

Ken Garrad. 3d polar plot. `https://se.mathworks.com/matlabcentral/fileexchange/13200-3d-polar-plot`, 2016.

Thomas C Grenfell, Steven P Neshyba, and Stephen G Warren. Representation of a nonspherical ice particle by a collection of independent spheres for scattering and absorption of radiation: 3. hollow columns and plates. *Journal of Geophysical Research: Atmospheres*, 110(D17), 2005.

Odelle L Hadley and Thomas W Kirchstetter. Black-carbon reduction of snow albedo. *Nature Climate Change*, 2(6):437–440, 2012.

Børge Hamre, Jan-Gunnar Winther, Sebastian Gerland, Jakob J Stamnes, and Knut Stamnes. Modeled and measured optical transmittance of snow-covered first-year sea ice in kongsfjorden, svalbard. *Journal of Geophysical Research: Oceans*, 109(C10), 2004.

Børge Hamre, Snorre Stamnes, Knut Stamnes, and Jakob Stamnes. Accurt: A versatile tool for radiative transfer simulations in the coupled atmosphere-ocean system. In *AIP Conference Proceedings*, volume 1810, page 120002. AIP Publishing, 2017.

James Hansen and Larissa Nazarenko. Soot climate forcing via snow and ice albedos. *Proceedings of the National Academy of Sciences of the United States of America*, 101(2):423–428, 2004.

Eugene Hecht and Alfred Zajac. *Optics*. Addison-Wesley, 1974.

Christian Hill and Roderick L Jones. Absorption of solar radiation by water vapor in clear and cloudy skies: Implications for anomalous absorption. *Journal of Geophysical Research: Atmospheres*, 105(D7):9421–9428, 2000.

Stephen R Hudson, Stephen G Warren, Richard E Brandt, Thomas C Grenfell, and Delphine Six. Spectral bidirectional reflectance of antarctic snow: Measurements and parameterization. *Journal of Geophysical Research: Atmospheres*, 111(D18), 2006.

Zhonghai Jin and James J Simpson. Bidirectional anisotropic reflectance of snow and sea ice in avhrr channel 1 and 2 spectral regions. i. theoretical analysis. *IEEE transactions on geoscience and remote sensing*, 37(1):543–554, 1999.

Marc L Kutner. *Astronomy: A physical perspective*. Cambridge University Press, 2003.

Dennis Lamb and Johannes Verlinde. *Physics and chemistry of clouds*. Cambridge University Press, 2011.

B Light, GA Maykut, and TC Grenfell. Effects of temperature on the microstructure of first-year arctic sea ice. *Journal of Geophysical Research: Oceans*, 108(C2), 2003.

Gary A Maykut. Large-scale heat exchange and ice production in the central arctic. *Journal of Geophysical Research: Oceans*, 87(C10):7971–7984, 1982.

U.S. Department of Commerce National Oceanic and Atmospheric Administration. NOAA. `https://www.esrl.noaa.gov/gmd/grad/solcalc/`, 2016. [Online: accessed April, 2016].

Norwegian Polar Institute. TopoSvalbard. `http://toposvalbard.npolar.no`, 2016. [Online: accessed August 24, 2016].

Donald K Perovich. The optical properties of sea ice. Technical report, COLD REGIONS RESEARCH AND ENGINEERING LAB HANOVER NH, 1996.

Ramses. *RAMSES hyperspectral radiometer manual Rel. 1.1.* TriOS Mess- und Datentechnik GmbH, Werftweg 15, D- 26135 Oldenburg, Germany, 2010. Rüdiger Heuermann (president).

John A Richards and JA Richards. *Remote sensing digital image analysis*, volume 3. Springer, 1999.

Gabriela Schaepman-Strub, ME Schaepman, TH Painter, S Dangel, and JV Martonchik. Reflectance quantities in optical remote sensing—definitions and case studies. *Remote sensing of environment*, 103(1):27–42, 2006.

Robert A Schowengerdt. *Remote sensing: models and methods for image processing.* Academic press, 2006.

CJ Stubenrauch, WB Rossow, Stefan Kinne, S Ackerman, G Cesana, H Chepfer, L Di Girolamo, B Getzewich, A Guignard, A Heidinger, et al. Assessment of global cloud datasets from satellites: Project and database initiated by the gewex radiation panel. *Bulletin of the American Meteorological Society*, 94 (7):1031–1049, 2013.

J Tim Suttles, Richard N Green, Patrick Minnis, GL Smith, WF Staylor, Bruce A Wielicki, IJ Walker, DF Young, VR Taylor, and LL Stowe. Angular radiation models for earth-atmosphere system. volume 1: Shortwave radiation. 1988.

V Taylor and Larry L Stowe. Reflectance characteristics of uniform earth and cloud surfaces derived from nimbus-7 erb. *Journal of Geophysical Research: Atmospheres*, 89(D4):4987–4996, 1984.

Gary E Thomas and Knut Stamnes. *Radiative transfer in the atmosphere and ocean*. Cambridge University Press, 2002.

Jørund Haldorson Tveiterås. Characterization of hyper spectral irradiance and radiance sensors. Master's thesis, The University of Bergen, 2013.

Stephen G Warren. Optical properties of snow. *Reviews of Geophysics*, 20(1): 67–89, 1982.

Stephen G Warren. Can black carbon in snow be detected by remote sensing? *Journal of Geophysical Research: Atmospheres*, 118(2):779–786, 2013.

Stephen G Warren and Richard E Brandt. Optical constants of ice from the ultraviolet to the microwave: A revised compilation. *Journal of Geophysical Research: Atmospheres*, 113(D14), 2008.

Stephen G Warren, Richard E Brandt, and Patricia O'Rawe Hinton. Effect of surface roughness on bidirectional reflectance of antarctic snow. *Journal of Geophysical Research: Planets*, 103(E11):25789–25807, 1998.

Stephen G Warren, Ignatius G Rigor, Norbert Untersteiner, Vladimir F Radionov, Nikolay N Bryazgin, Yevgeniy I Aleksandrov, and Roger Colony. Snow depth on arctic sea ice. *Journal of Climate*, 12(6):1814–1829, 1999.

Warren J Wiscombe and Stephen G Warren. A model for the spectral albedo of snow. i: Pure snow. *Journal of the Atmospheric Sciences*, 37(12):2712–2733, 1980.

Zeiss. *MMS – Monolithic Miniature-Spectrometer*, 2017.

Appendices

Appendix A

A.1 Abbreviations

Table A.1: Abbreviations

Abbreviation	Description
ARF	Anisotropic reflectance factor
BRDF	Bidirectional reflectance distribution function
EM	Electromagnetic
FOV	Field of view
IOP's	Inherent optical properties
NIR	Near Infrared
ppt.	Precipitation
SAA	Solar azimuth angle
SZA	Solar zenith angle
TOA	Top of atmosphere
UV	Ultraviolet

A.2 Nomenclature

Scalar and Cosine Irradiance While the scalar irradiance is collected ”as-is”, by a spherically shaped sensor, the cosine response sensor is flat. It also measures all light hitting it, but due to its geometry it weighs the light signal with the cosine of the incident beam.

Single scattering albedo $\bar{\omega}$ takes values between 0 and 1, and represents the probability of an incident photon being scattered or transmitted [Bohren and Clothiaux, 2006].

Solid angle In radiometry the principle of solid angles stands central. As opposed to 2D angles which are measured in radians (or degrees), 3D angles are measured in steradians [sr]. A full unit circle equals 2π radians, a unit sphere 4π steradians.

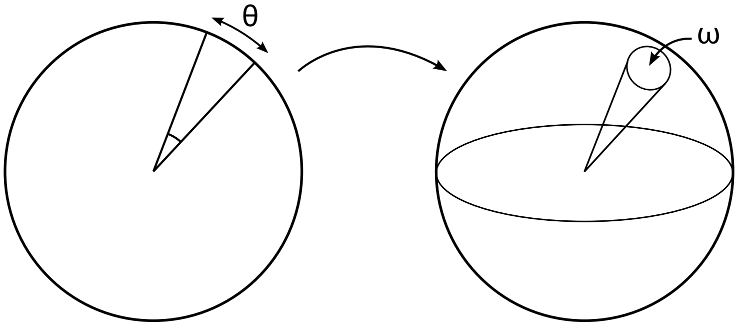

Figure A.1: The principle of angles in 2D and 3D. In 2D (left), an angle can be defined as a length section of the unit circle, with its magnitude being its arc length. In 3D (right) a solid angle is defined as an areal section of the unit sphere, with its magnitude being its area.

Appendix B

B.1 Excessive figures

ARF figures

As seen in Figure 4.4, the angular distribution changed shaped distinctively for decreasing snow depth. In Figure B.1 we see the response to very thin snow for larger zenith angles. At $\theta_0 = 55°$ (left panels) the effect is not as prominent, and at $\theta_0 = 70°$, the response is indistinguishable.

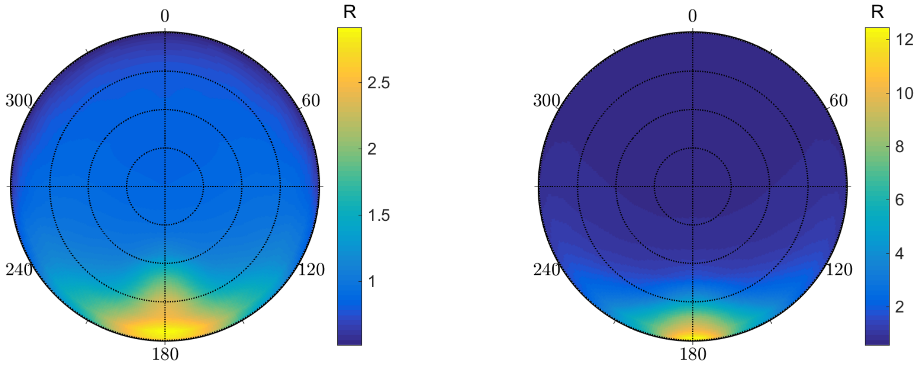

(a) SZA: 55°, depth: 200 µm

(b) SZA: 70°, depth: 200 µm

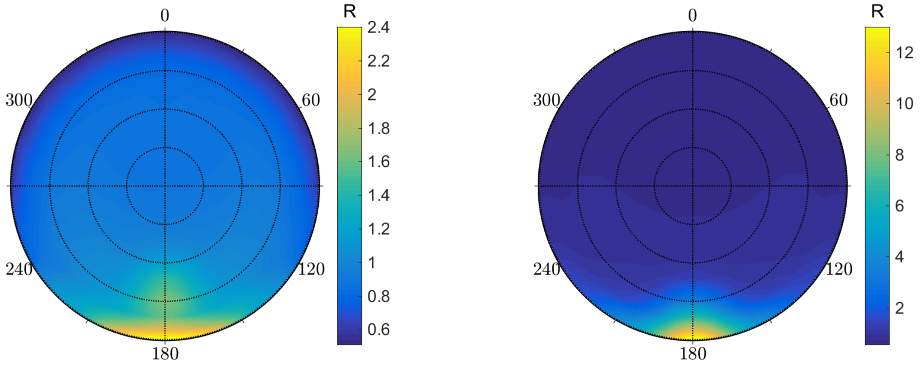

(c) SZA: 55°, depth: 50 µm

(d) SZA: 70°, depth: 50 µm

Figure B.1: R of snow for decreasing snow depth, $\lambda = 800$ nm. SZA: 55° in left panels, 70° in the right. Snow depth is 200 µm in the top panels, 50 in the bottom. The snow pack consists of a one meter thick homogenous layer, with density 300 kgm^{-3} and snow grain radii 200µm.

Appendix C

C.1 Some reflections on field work in the Arctic

The process of creating the work in this thesis, both what is included and not, has been a journey like no other. From basking around in a huge scooter suit on an enormous glacier in a remote, completely breathtakingly beautiful scenery, to handling and interpreting data, creating dozens of decent looking and sense-making elements, reading and analyzing a large amount of scientific papers, and running the model created by some of the great minds in this institute.

Restrictions on bringing equipment and extra weight are high, when travelling to Ny-Ålesund. We were unable to bring enough equipment to collect albedo data.

We originally had six days of field work. Critical issues such as complete system failure, and one or more sensors falling out are to blame. The sensors are designed to operate within -10 to +50 °C, while we some days had temperatures drop to as low as -20. As we have no data from these days, we have left them out of Table 3.2. We also learned that the computer was sensitivity to the cold weather, as it reacted with warning, error messages and complete shut down several times. We eventually created a heating system, consisting of hot water transferred from thermoses to plastic bottles (see the figure below), bubble wrap and an aluminium box. After rigging up the setup and pouring water into the bottles, we quickly retrieved the PC from a warm scooter suit, connected it to the PS101 power supply, started the sampling software, and installed it in the box. This way we were able to retrieve data. Although it worked quite well, we still highly recommend bringing computers designed for harsh outdoor environments for fieldwork in the Arctic.

Figure C.1: Our not so hi-tech, but very functioning heating system.